The HERMES Experiment

I. Analyzing Powers in Pion Electroproduction

II. The Aerogel Radiator of the HERMES RICH

Thesis by

Paul Whitton Carter

In Partial Fulfillment of the Requirements

for the Degree of

Doctor of Philosophy

California Institute of Technology

Pasadena, California

1999

(Submitted May 12, 1999)

Acknowledgments

I owe a great deal of thanks to many people who have aided me during my stay at Kellogg Radiation Lab. My advisor, Dr. Brad Filippone, provided invaluable guidance for my research and opportunities to grow as a scientist. I also thank Dr. Robert McKeown and the other professors and postdocs at Kellogg who have given me advice and encouragement. Several others deserve thanks for devoting many hours of technical support to my research. Pat Huber kept the computers running smoothly and rescued me when I accidentally deleted my data. Al Massey and Jim Pendlay helped me design circuits, build lab equipment, and find my way around the electronics shop. Jack Richards and Mike Vondrus expertly built devices that were critical to my success. I owe apologies as well as thanks to those who volunteered to help with ungratifying tasks associated with my research, especially Bob Carr and Joe Renes for traveling to DESY and installing hundreds of aerogel tiles.

I am indebted to countless members of the HERMES Collaboration I have been involved with. It has been a great pleasure to work with the RICH and azimuthal analysis subgroups. I am particularly grateful to Harout Avakian, who played a leading role in the azimuthal analysis and who I have enjoyed working closely with. The time I spent at DESY would not have been as enjoyable if not for my fellow HERMES students. Balijeet Bains was a great roommate in Hamburg, and I enjoyed the companionship of the football/hacky sack gang.

My family and friends have provided me with a network of unfaltering support. Thanks to Hooman Davoudiasl and others who suffered with me through problem sets during my early years at Caltech, and to Andrea Dvoredsky for useful physics discussions at Baskin–Robbins and Big Bear. Mike Kidder, Tina Tran, and the rest of the martial arts students and teachers I have trained with have been a second family to me. My good friend John Andersen was always just a phone call away and offered much needed sympathy for the trials I faced as a graduate student. My mother, father,

and sister Beth have been a constant source of comfort and reassurance. Finally, I am grateful to my girlfriend Mimi for her love, emotional support, and for taking such good care of me.

Abstract

Analyzing powers in pion electroproduction were measured in semi–inclusive deep inelastic scattering of longitudinally polarized positrons from a longitudinally polarized hydrogen target using the HERMES spectrometer in the DESY storage ring during the 1996 and 1997 data taking periods. The target spin and $\sin\phi$ dependent portion of the π^+ production cross section was measured to be nonzero with high significance. The π^- result was consistent with zero within experimental errors. These results are compared and contrasted with existing experimental results and interpreted in the context of recent theoretical ideas.

Accurate particle identification over a large momentum range is crucial in measurements of semi–inclusive processes. To enhance its particle identification capabilities, the HERMES Experiment upgraded its spectrometer in 1998 with a ring imaging Čerenkov detector (RICH) using aerogel and C_4F_{10} radiators. The use of aerogel in a RICH is a novel technique that requires a detailed understanding of its optical properties. A comprehensive series of measurements was carried out to characterize the generation and propagation of Čerenkov light in aerogel. The results were used to evaluate the expected performance of the aerogel radiator in the HERMES RICH.

Contents

List of Figures

List of Tables

Part I

Introduction

Chapter 1 Spin Dependent Deep Inelastic Scattering

1.1 Background

The deep inelastic scattering (DIS) of leptons from nucleons has been a key experimental tool revealing the quark parton composition of hadrons. Much of the experimental confirmation of the validity of the quantum chromodynamic theoretical framework for describing hadronic structure and interactions came through unpolarized DIS. The observation of Bjorken scaling in unpolarized DIS pointed to the existence of point-like quark constituents of nucleons. Small deviations from Bjorken scaling are accurately predicted within QCD in terms of gluon emission by the scattered quarks. The momentum distributions of valence and sea quarks within nucleons have been precisely determined, and provide further evidence for the important role of gluonic degrees of freedom.

In more recent years, the availability of polarized beams and targets have permitted the investigation of the spin dependence of DIS. The spin of the nucleon can be decomposed into quark helicity (Σ), quark orbital (L_q), gluon spin (ΔG), and gluon orbital (L_g) parts: [1, 2]

$$\frac{1}{2} = \frac{1}{2}\Sigma + \Delta G + L_q + L_g$$

Spin dependent DIS measurements (in conjunction with other measurements) revealed that only a small fraction of the nucleon spin was carried by the quarks. The most recent experiments have used semi–inclusive deep inelastic scattering to separate the contributions of different quark flavors to Σ, and on the not-too-distant horizon is the possibility to measure ΔG and orbital angular momentum contributions.

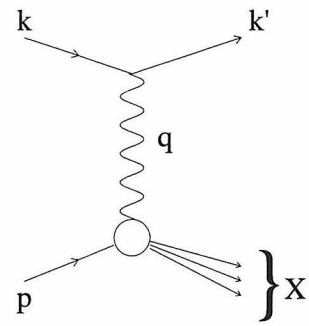

Figure 1.1: Leading order Feynman diagram describing inclusive DIS .

1.2 Inclusive Spin–Dependent DIS

The Feynman diagram describing inclusive DIS in leading order is shown in Figure 1.1. A positron with momentum k is incident on a proton of momentum p and mass M, and the scattered positron with momentum k' is detected. A virtual photon with momentum $q = k - k'$ and negative invariant mass squared $Q^2 = -q^2$ is exchanged. The undetected hadronic final state has invariant mass squared $W^2 = (p+q)^2$. Other useful invariants include $x = Q^2/(2p \cdot q)$, $y = (p \cdot q)/(p \cdot k)$, and $\nu = (p \cdot q)/M$.

The cross section is given by [3]

$$\frac{d\sigma^{s_e s}}{dxdy} = \frac{2\pi\alpha^2 My}{Q^4} L_{\mu\nu} W^{\mu\nu},$$

where α is the fine structure constant and s_e and s label the spins of the positron and proton, respectively. The lepton tensor L contains a symmetric, spin–independent part and an antisymmetric, spin–dependent part: [4]

$$L_{\mu\nu} = k'_\mu k_\nu + k'_\nu k_\mu - g_{\mu\nu} k' \cdot k + im\epsilon_{\mu\nu\alpha\beta} s_e^\alpha q^\beta,$$

where m is the positron mass. The hadronic current is similarly split into symmetric

and antisymmetric parts, $W = W_S + W_A$, with [4]

$$\begin{aligned} W_S^{\mu\nu} &= \left(g^{\mu\nu} + \frac{q^\mu q^\nu}{q^2}\right) W_1 + \frac{1}{M^2}\left(p^\mu - \frac{p\cdot q}{q^2}q^\mu\right)\left(p^\nu - \frac{p\cdot q}{q^2}q^\nu\right) W_2 \\ W_A^{\mu\nu} &= M\epsilon^{\mu\nu\alpha\beta}q_\alpha s_\beta G_1 + \frac{1}{M}\epsilon^{\mu\nu\alpha\beta}q_\alpha\left[(p\cdot q)s_\beta - (s\cdot q)p_\beta\right] G_2. \end{aligned}$$

The structure of the hadronic tensor is constrained to have this form in order to satisfy Lorentz invariance, hermiticity, and gauge invariance. [5].

W_1 and W_2 are the familiar spin–independent structure functions describing unpolarized scattering. The spin–dependent structure functions G_1 and G_2 can be accessed experimentally by comparing cross sections for scattering with opposite target polarizations. In the case of a longitudinally polarized target, for instance, the difference between cross sections with positron and proton spins antiparallel and parallel is given by [4]

$$\frac{d(\sigma^{\uparrow\downarrow} - \sigma^{\uparrow\uparrow})}{d\Omega dE'} = \frac{4\alpha^2}{Q^2}\frac{E'}{E}\left[MG_1(E + E'\cos\theta) - Q^2G_2)\right],$$

where E and E' are the incident and scattered positron energies in the lab frame and θ is the positron scattering angle. The cross section may also be written in terms of dimensionless structure functions g_1 and g_2:

$$\frac{d(\sigma^{\uparrow\downarrow} - \sigma^{\uparrow\uparrow})}{dxdy} = \frac{16\pi\alpha^2}{Q^2}\left[\left(1 - \frac{y}{2} - \frac{y^2}{4}\gamma^2\right)g_1 - \frac{y}{2}\gamma^2 g_2\right],$$

where $g_1 \equiv M^2\nu G_1$, $g_2 \equiv M\nu^2 G_2$, and $\gamma \equiv Q/\nu$.

1.3 Quark Parton Model

The spin–independent structure function $f_1 \equiv MW_1$ and the spin–dependent structure function g_1 have a simple interpretation in the context of the quark parton model. [6, 7, 8] The quark parton model treats the nucleon as a collection of point-like quark constituents. The DIS process is considered in the limit of infinite momentum

of the proton in which time dilation effects suppress the interactions of the quarks. In the Bjorken limit of large Q^2 and large ν with constant $x = Q^2/2M\nu$, the virtual photon wavelength is small enough to resolve the point-like quarks so that the scattering can be viewed as elastic scattering of the virtual photon off free quarks, and x is interpreted as the fraction of the nucleon's momentum carried by the struck quark.

f_1 and g_1 can be written in terms of polarized quark distributions $q_f^{\uparrow}$ and $q_f^{\downarrow}$. $q_f^{\uparrow(\downarrow)}(x)$ is the probability density of quarks of flavor f with momentum fraction x and helicity equal to (opposite) that of the parent proton. f_1 and g_1 are given by [4, 8]

$$\begin{aligned} f_1 &= \frac{1}{2}\sum_f e_f^2 q_f \\ g_1 &= \frac{1}{2}\sum_f e_f^2 \Delta q_f \\ q_f &= q_f^{\uparrow} + q_f^{\downarrow} \\ \Delta q_f &= q_f^{\uparrow} - q_f^{\downarrow} \end{aligned}$$

where e_f is the charge of quark flavor f in units of the positron charge.

1.4 Semi–Inclusive Spin–Dependent DIS

The Feynman diagram for semi–inclusive deep inelastic scattering (SIDIS) is shown in Figure 1.2. In SIDIS, a hadron with momentum p_h is detected in coincidence with the scattered positron while other products of the interaction go undetected. The invariant $z = p \cdot p_h / p \cdot q$ is used in addition to the kinematic variables discussed in the previous chapter. In the laboratory frame (target at rest), z is the energy fraction E_h/ν of the virtual photon carried by the hadron. Also in common use is Feynman's $x_F = p_{hz}/p_{hz}^{\max} \approx 2p_{hz}^{\rm cm}/W$, where the z axis is taken to lie along the virtual photon direction, p_h^{cm} is the hadron momentum in the virtual photon and proton center-of-momentum frame. Finally, $p_{h\perp}$ (or simply $p_\perp$) will be used to denote the transverse momentum of the hadron with respect to the virtual photon.

Hadron production is described within the quark parton model as the absorption

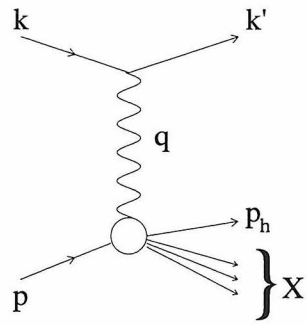

Figure 1.2: Leading order Feynman diagram describing SIDIS.

of the virtual photon by a quark and the subsequent fragmentation of the struck quark into the final state hadron. In the case of unpolarized SIDIS, this process is described by a quark distribution function $q_f = q_f^{\uparrow} + q_f^{\downarrow}$ and a fragmentation function $D_f^h(z)$ for a quark of flavor f to produce a hadron h with energy fraction z.

The SIDIS cross section to produce a hadron h with energy fraction z is given by [8, 9]

$$\sigma^h(x,z) \propto \sum_f e_f^2 q_f(x) D_f^h(z).$$

In spin–dependent SIDIS, the spin asymmetry of the production of hadron h is [9]

$$A_1^h(x,z) \;=\; \frac{\sum_f e_f^2 \Delta q_f(x) D_f^h(z)}{\sum_f e_f^2 q_f(x) D_f^h}$$

Measurements of A_1^h for positively and negatively charged hadrons on a combination of proton and neutron targets allows an extraction of the quark polarizations $\Delta q_f(x)/q_f(x)$.

Part II

Analyzing Powers in Pion Electroproduction

Chapter 2 Theoretical and Experimental Framework

2.1 Transverse Spin Degrees of Freedom in DIS

Assuming helicity conservation, parity invariance, and time reversal invariance, there are three independent helicity amplitudes at twist-2 (see Appendix C for a discussion of twist). In addition to the quark distributions q_f and Δq_f discussed earlier, a third distribution δq_f is required to complete the twist-2 description of nucleon structure. This is called a transversity distribution [10, 11] as it measures the distribution of quark transverse spin in a transversely polarized proton. The roles of the three kinds of distributions can be seen in a spin density matrix representation of the leading twist quark distribution:

$$\mathcal{F}(x) = \frac{1}{2}q(x)I \otimes I + \frac{1}{2}\Delta q(x)\sigma_3 \otimes \sigma_3 + \frac{1}{2}\delta q(x)(\sigma_+ \otimes \sigma_- + \sigma_- \otimes \sigma_+) \qquad (2.1)$$

where I is the identity matrix and the σ_i are Pauli matrices. The matrices lie in the quark $\otimes$ nucleon helicity spaces. This result is written in such a way that q and Δq are diagonal, but δq is off–diagonal. Using a different basis, δq can be diagonalized so that it may be written as a difference of probabilities to find a quark polarized along and against the polarization of a transversely polarized proton.

The leading twist transverse spin–dependent structure function is denoted h_1:

$$h_1 = \frac{1}{2}\sum_f e_f^2 \delta q_f$$

An alternate notation will be used in the following, replacing $q_f(x)$ with $f_1^f(x)$, $\Delta q_f(x)$ with $g_1^f(x)$, and $\delta q_f(x)$ with $h_1^f(x)$ to more closely identify quark densities with the

associated distribution functions.

h_1 is analogous to g_1, describing the transverse polarization of quarks in a transversely polarized nucleon. In the nonrelativistic quark model, $h_1 = g_1$ since spin and space operations commute. [11] However, deviations from the nonrelativistic quark relations $g_A/g_V = 5/3$ and $\Delta q = 1$ are found experimentally, demonstrating the importance of relativistic effects in the nucleon. The difference between the helicity and transversity distributions is an additional measure of relativistic effects in the nucleon. [11, 12] Small differences between h_1 and g_1 appear in the MIT bag model. [13]

The measurement of the transversity distribution through DIS is made difficult by its chiral odd nature. As shown by Equation 2.1, the transversity distribution is related to an amplitude that flips the helicities of the quark and nucleon. Since helicity and chirality are identical for the "good" (leading twist) light cone components of the Dirac field, the amplitude flips the chirality as well as the helicity of the quark. Chirality must be conserved in perturbative QCD and in electroweak currents, so the chiral odd transversity distribution can only be measured in combination with another chiral odd structure. In Drell–Yan scattering, a chirally odd antiquark distribution can come into play. In SIDIS, it appears through a chiral odd fragmentation process.

2.2 Chiral Odd Fragmentation

2.2.1 Collins Effect

Collins [12] first proposed the measurement of h_1 using SIDIS by measuring the azimuthal distribution of hadrons. The azimuthal angle ϕ is measured between the hadron production plane and the positron scattering plane, as shown in Figure 2.1. The proposed measurement was to use a transversely polarized target, but a longitudinally polarized target can also be used as long as the component of the polarization perpendicular to the virtual photon direction is sufficiently large. The hard scattering process transfers the transverse polarization to the outgoing quark, and through

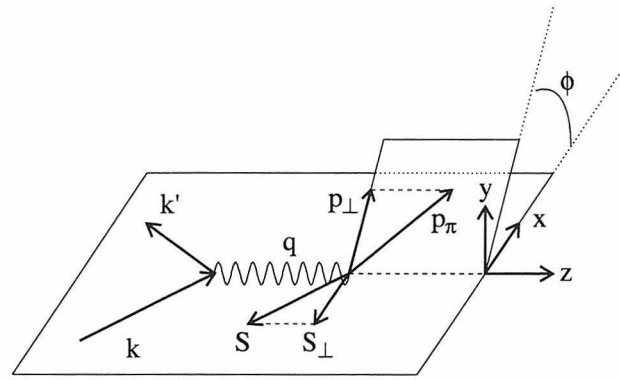

Figure 2.1: Definition of the azimuthal angle ϕ. The target is shown polarized longitudinally with respect to the incoming lepton.

a chiral odd fragmentation process, an asymmetry in the azimuthal distribution of the outgoing hadron is allowed. Collins predicted that the asymmetry should depend on the following quantity, the cosine of the Collins angle ϕ_C:

$$\cos\phi_C = \frac{\mathbf{p_h} \times \mathbf{q} \cdot \mathbf{S}_\perp}{|\mathbf{p_h} \times \mathbf{q}|\,|\mathbf{S}_\perp|}, \tag{2.2}$$

where $\mathbf{S}_\perp$ is the component of the target spin transverse to the virtual photon. For a longitudinally polarized target, $\mathbf{S}_\perp$ is constrained to lie in the electron scattering plane (see Figure 2.1) so that $\cos\phi_C = \sin\phi$.

The chiral odd fragmentation function is denoted $H_1^\perp$. It is odd under "naive" time reversal in which the transformation $(\mathbf{p_h}, \mathbf{q}, \mathbf{S}_\perp) \rightarrow -(\mathbf{p_h}, \mathbf{q}, \mathbf{S}_\perp)$ in Equation 2.2 reverses the sign of the triple product. This apparent violation of time reversal would forbid such a fragmentation process if not for nontrivial phases generated by nonperturbative final state interactions between the produced hadron and the remnants of the fragmenting quark [11, 12, 14]. The fragmentation process does not violate parity.

2.2.2 Semi-classical Model of Fragmentation

A simple way to understand how a chiral odd fragmentation function can arise is to use a semi-classical model [15]. The model is illustrated in Figure 2.2. A transversely polarized valence quark q_0 is ejected from the parent nucleon by a virtual photon or

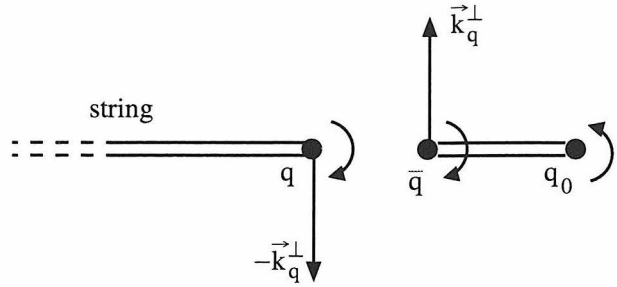

Figure 2.2: Semi-classical model of chiral odd fragmentation. Curved arrows denote the quark spins.

gluon. A color string extends itself between the struck quark and the original collision region containing the nucleon remnant. The string is broken with the formation of a $q\overline{q}$ pair. The $q\overline{q}$ system is in a ${}^3P_0$ state in order to retain vacuum quantum numbers. The nonzero orbital angular momentum of the pair provides these q and $\overline{q}$ with equal and opposite transverse momenta with respect to the string. In order for the $q\overline{q}$ system to have total angular momentum zero, the spins of the q and $\overline{q}$ must be parallel and oriented opposite the pair's orbital angular momentum. The quarks that make up the spinless final state pion have antialigned spins, so the $q\overline{q}$ pair production is governed by a projection operator

$$\frac{1}{4} - \mathbf{s}(q_0) \cdot \mathbf{s}(\overline{q})$$

where $\mathbf{s}$ is the quark spin operator. This operator induces a correlation between the spin of the valence quark and the transverse momentum of the $\overline{q}$ which then becomes the transverse momentum of the outgoing pion. For an upwardly polarized valence quark, the outgoing pion favors going leftward.

2.3 Experimental Results

2.3.1 Fermilab E704

The Fermilab E704 experiment [16] measured the analyzing power of pion production by the scattering of a transversely polarized antiproton beam on a proton target,

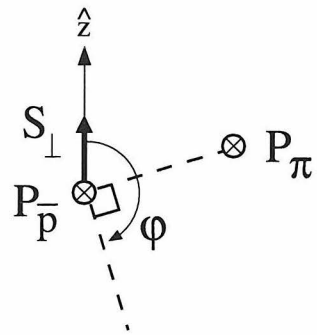

Figure 2.3: Kinematics associated with analyzing powers measured in the Fermilab E704 experiment. Incoming beam momentum $\mathbf{p}_{\overline{p}}$ and outgoing pion momentum $\mathbf{p}_{\pi}$ are pointed into the page. The beam polarization $\mathbf{S}_{\perp}$ is aligned parallel or antiparallel to the polarization axis $\hat{z}$.

$\overline{p}^{\uparrow}p \to \pi X$. A Collins angle can be defined in an analogous way as in SIDIS, with the jet axis defined by the beam momentum $\mathbf{p}_{\overline{p}}$ rather than the virtual photon momentum:

$$\cos\phi_C = \frac{\mathbf{p}_{\pi} \times \mathbf{p}_{\overline{p}} \cdot \mathbf{S}_{\perp}}{|\mathbf{p}_{\pi} \times \mathbf{p}_{\overline{p}}|\,|\mathbf{S}_{\perp}|}$$

Figure 2.3 illustrates the kinematics. The azimuthal angles ϕ of the outgoing pions were measured with respect to the beam polarization axis $\hat{z}$:

$$\cos\phi = -\frac{\mathbf{p}_{\pi} \times \mathbf{p}_{\overline{p}} \cdot \hat{z}}{|\mathbf{p}_{\pi} \times \mathbf{p}_{\overline{p}}|}$$

The analyzing power A_N, defined as

$$A_N = \frac{1}{P_B \langle\cos\phi\rangle} \frac{N^{\uparrow} - N^{\downarrow}}{N^{\uparrow} + N^{\downarrow}},$$

was measured in the range $0.2 \leq x_F \leq 0.9$ and $0.2 \leq p_{\perp} \leq 1.5$ GeV. P_B is the beam polarization and $N^{\uparrow(\downarrow)}$ is the number of pions (normalized by the beam flux) produced with the beam spin oriented parallel(antiparallel) to the beam polarization axis. A positive analyzing power means that for beam polarization directed upward (parallel to $\hat{z}$), the cross section is greater for particle production toward beam left.

The analyzing power was found to increase in magnitude with increasing x_F and $p_{\perp}$. The analyzing powers of the charged pions have similar magnitudes but opposite

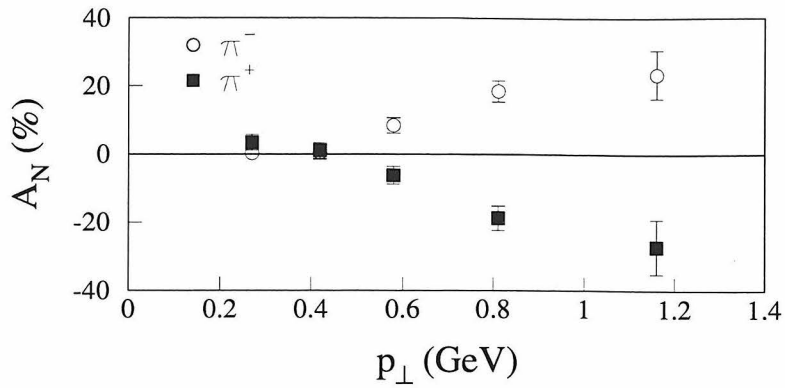

Figure 2.4: Analyzing power A_N of pion production by antiprotons as a function of $p_\perp$ measured by the Fermilab E704 experiment.

signs, with positive analyzing power for π^- production and negative for π^+. Sample results are shown in Figures 2.4 and 2.5.

The general features of the data can be explained using the semi-classical fragmentation model. In an upwardly polarized antiproton, the $\overline{u}$ quarks that tend to produce π^- are upwardly polarized so that the π^- favors going left while the $\overline{d}$ quarks that tend to produce π^+ are downwardly polarized so that the π^+ favors going right.

Data were also collected with a transversely polarized proton beam. [17, 18] The results are shown in Figure 2.6 for neutral as well as charged pions. The signs of the analyzing powers are reversed with respect to the case of the antiproton beam, as predicted by the semi-classical fragmentation model.

The experimental evidence for large single spin asymmetries is surprising in that single spin asymmetries in large $p_\perp$ inclusive hadronic reactions are forbidden in leading twist perturbative QCD. [19] This follows from the observation that single spin asymmetries are zero at the partonic level due to helicity conservation and parity and time reversal invariance. A parton level single spin asymmetry can only appear at the level of $m_q/\sqrt{s}$, where m_q is a quark mass. [20] It follows that collinear partonic configurations in hadrons prohibit single spin asymmetries. The interaction is in the

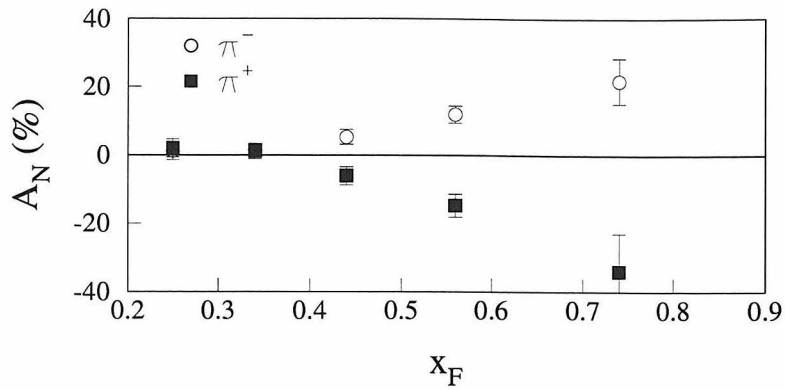

Figure 2.5: Analyzing power A_N of pion production by antiprotons as a function of x_F measured by the Fermilab E704 experiment.

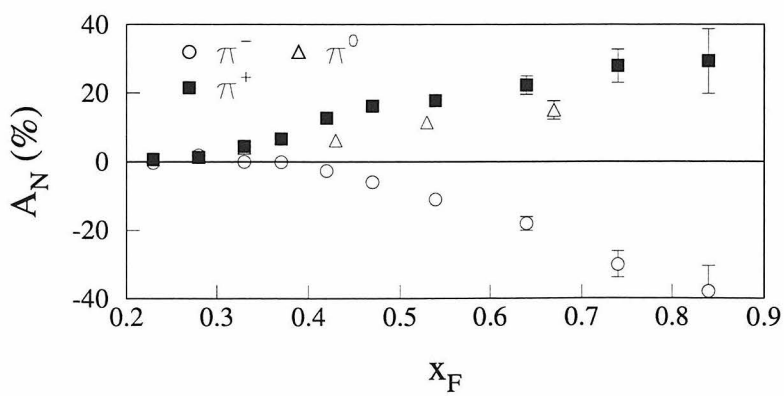

Figure 2.6: Analyzing power A_N of pion production by protons as a function of x_F measured by the Fermilab E704 experiment.

perturbative regime for values of $p_\perp$ larger than Λ_{QCD}, and so many explanations of the effect rely on the fact that the asymmetries are observed at moderate $p_\perp$ values where intrinsic transverse momentum effects in the distribution and fragmentation functions can come into play.

The interpretation of the E704 data is complicated by the fact that more than one mechanism can explain the single spin asymmetry [21]. In addition to the Collins mechanism in which final state interactions allow T-odd fragmentation, a nonzero analyzing power can arise through the Sivers mechanism [22], representing in a sense the "opposite" of the Collins mechanism. In the Sivers mechanism, single spin asymmetries result from soft initial state interactions between the colliding hadrons, permitting a T-odd distribution function that describes the transverse momentum dependence of quarks in a transversely polarized nucleon. The E704 data have been analyzed assuming the action of the two mechanisms separately and in combination and the relevant T-odd distribution and fragmentation functions have been estimated accordingly. [21, 23, 24]

2.3.2 DELPHI

The DELPHI experiment, using the e^+e^- collider at LEP, measured left–right asymmetries in the fragmentation of transversely polarized quarks produced in Z^0 decays [25]. The transverse polarizations of quarks and antiquarks are highly correlated near the Z^0 peak, and through a Collins fragmentation process give rise to an azimuthal asymmetry in the production of a hadron in one jet around the axis of a second hadron in the opposite jet [26]. A nonzero result for $H_1^\perp$ averaged over the full data set was obtained:

$$\left|\frac{H_1^\perp}{D_1}\right| = 6.3 \pm 1.7\%$$

where D_1 is the favored unpolarized fragmentation function of pion production. This result provides further impetus for testing the Collins proposal to measure h_1 in SIDIS.

Analyzing the E704 data under the assumption of the action of Collins fragmentation alone and extracting the favored fragmentation function $H_1^{\perp \text{fav}}$, the following integral can be evaluated [24]:

$$\left| \frac{\int_{0.1}^{1} dz H_1^{\perp \text{fav}}(z)}{\int_{0.1}^{1} dz D_1^{\text{fav}}(z)} \right| = 7.6\%,$$

in agreement with the above experimental result.

2.4 Analyzing Power of Pion Electroproduction

An advantage of SIDIS in exploring spin–azimuthal asymmetries is that the Collins mechanism is expected to be dominant. [21] The initial state interactions are suppressed by higher powers of α_{em}, so the Sivers mechanism does not come into play. In contrast, the Sivers mechanism dominates in the case of prompt photon production $p^{\uparrow}p \to \gamma X$ and the Drell–Yan process $p^{\uparrow}p \to \mu^{+}\mu^{-}X$, so measurements of these processes could provide complementary information to the SIDIS measurements and fully characterize the size of the two mechanisms. It is possible for T-odd distributions to appear in SIDIS even in the absence of initial state interactions [27], but the T-odd distributions extracted from the E704 measurements suggest that even if present in SIDIS, they are expected to be important only in relatively extreme kinematic conditions, namely at very low z. [24]

A complete tree–level calculation of the cross section of pion electroproduction has been carried out to order $1/Q$, showing explicitly the azimuthal dependence and the twist-2 and twist-3 level contributions [3]. The SIDIS cross section can be separated into parts that depend on unpolarized (0) or longitudinally polarized (L) leptons, and unpolarized, longitudinally polarized, or transversely polarized (T) nucleons in the initial state. Up to order $1/Q$ the following terms contribute:

$$\sigma = \sigma_{00} + \sigma_{0L} + \sigma_{0T} + \sigma_{L0} + \sigma_{LL} + \sigma_{LT}$$

where σ_{0L} for instance refers to the cross section for an unpolarized beam on a target

polarized longitudinally with respect to the virtual photon. The unpolarized cross section and the cross sections involving only the target spin are shown in Appendix A.

HERMES is sensitive to the full angular dependence of both σ_{0L} and σ_{0T} through the longitudinal and transverse components of the target spin with respect to the virtual photon direction. For a target polarized longitudinally with respect to the incoming positron, the components of the target spin in the target rest frame parallel and transverse to the virtual photon direction are

$$\lambda = s_\lambda \sqrt{\frac{Q^2}{Q^2+4M^2x^2}}\left(1+\frac{2M^2x^2y}{Q^2}\right) \approx s_\lambda$$

and

$$|\mathbf{S}_\perp| = \sqrt{\frac{4M^2x^2}{Q^2+4M^2x^2}\left(1-y-\frac{M^2x^2y^2}{Q^2}\right)} \approx \frac{2Mx}{Q}\sqrt{1-y},$$

respectively, where $s_\lambda = \lambda/|\lambda| = \pm 1$ is a convenient label for the target polarization state. The Collins effect appears in σ_{0T} as (see Appendix A)

$$\sin(\phi+\phi_s)h_1(x)H_1^\perp(z)$$

where ϕ_s is the azimuthal angle of the target spin with respect to the lepton scattering plane. For a longitudinally polarized target, ϕ_s is restricted to the values 0 or π so that flipping the target spin effectively reverses the sign of the Collins term, that is,

$$\sin(\phi-\phi_s) = -s_\lambda \sin\phi$$

The $\sin\phi$ dependent cross section for a longitudinally polarized target also receives a contribution from σ_{0L} involving, for example, the combination $h_{1L}^\perp H_1^\perp$. $h_{1L}^\perp$ describes transverse quark polarization in a longitudinally polarized nucleon. For a longitudinally polarized target, the contributions from σ_{0T} and σ_{0L} are comparable in that both appear at the same order in $1/Q$: the twist-2 Collins term is multiplied by $|\mathbf{S}_\perp| \propto 1/Q$ while the σ_{0L} contribution is twist-3. Appendix A shows that a $\sin 2\phi$

dependent target spin asymmetry appears at twist-2 in σ_{0L} (in contrast to the twist-3 $\sin\phi$ term) and comes from the combination $h_{1L}^{\perp}H_1^{\perp}$. The only remaining target spin asymmetry to be expected at this order is a $\sin 3\phi$ asymmetry involving $h_{1T}^{\perp}H_1^{\perp}$ (which also appears in $\sin 2\phi$). It also appears at twist-2, multiplied by $|\mathbf{S}_\perp|$. $h_{1T}^{\perp}$ describes the transverse polarization of quarks in a transversely polarized nucleon, but with the quark polarization also transverse to the nucleon polarization. The distribution and fragmentation functions appearing in the cross sections are classified in Appendix B with simple pictorial interpretations of the twist-2 functions in terms of quark spin densities. The $\sin\phi$ dependent single spin asymmetries on a longitudinally polarized target have been estimated to be of the order of a few percent in the HERMES kinematic range. [28]

It is convenient to use the following notation for moments of the above cross sections:

$$\langle W\rangle_{AB} = \int d\phi \frac{W d\sigma_{AB}}{dxdydzdP_\perp d\phi}$$

where A and B are beam and target polarization states, respectively, taking the values 0, L, or T. Including only the most relevant terms, the pion electroproduction cross section may be written

$$\begin{aligned}
\frac{d\sigma}{dxdydzdP_\perp d\phi} &= \langle 1\rangle_{00} + \langle 1\rangle_{LL} + \\
&\quad (2\langle\sin\phi\rangle_{0L} + 2\langle\sin\phi\rangle_{0T})\sin\phi + \\
&\quad (2\langle\sin 2\phi\rangle_{0L} + 2\langle\sin 2\phi\rangle_{0T})\sin 2\phi + \cdots \\
&= \langle 1\rangle_{00}\left(1 + \frac{\langle 1\rangle_{LL}}{\langle 1\rangle_{00}} + s_\lambda \frac{2s_\lambda(\langle\sin\phi\rangle_{0L} + \langle\sin\phi\rangle_{0T})}{\langle 1\rangle_{00}}\sin\phi + \right. \\
&\quad \left. s_\lambda \frac{2s_\lambda(\langle\sin 2\phi\rangle_{0L} + \langle\sin 2\phi\rangle_{0T})}{\langle 1\rangle_{00}}\sin 2\phi + \cdots\right) \\
&\equiv \langle 1\rangle_{00}\left(1 + \frac{\langle 1\rangle_{LL}}{\langle 1\rangle_{00}} + s_\lambda P_T \mathcal{A}^{\phi}\sin\phi + s_\lambda P_T \mathcal{A}^{2\phi}\sin 2\phi + \cdots\right)
\end{aligned}$$

where $s_\lambda^2 = 1$ was used and P_T is the magnitude of the target polarization. The last line defines the analyzing powers $\mathcal{A}^{m\phi}$, the quantities to be extracted in this

thesis. The analyzing powers depend on the distribution and fragmentation functions roughly as

$$\mathcal{A}^{m\phi} \approx \frac{h(x)H_1^{\perp}(z)}{f_1(x)D_1(z)}$$

where the approximation is meant only to display the distribution and fragmentation structure of the numerator and denominator. h represents the chiral odd distribution functions such as h_1 and $h_{1L}^{\perp}$.

This thesis will present the results of the first measurement of analyzing powers in semi–inclusive pion electroproduction. The observation of nonzero analyzing power would provide strong evidence for the existence of chiral odd distribution and fragmentation functions.

Chapter 3 The HERMES Experiment

3.1 HERA Storage Ring at DESY

The HERMES experiment is located at the East Hall of the HERA storage ring at DESY. HERMES is designed to pursue a broad program of measurements of inclusive and semi–inclusive DIS using a polarized positron beam incident on polarized and unpolarized targets.

The HERA facility at DESY [29] is designed for positron–proton collisions. It consists of two counterrotating beams of positrons and protons stored in 6.3 km circumference rings at energies of 27.6 GeV and 820 GeV, respectively. The beams can be collided in four intersection regions at the North, South, East, and West Halls. HERMES makes use of the positron beam only with a fixed target internal to the positron ring. The proton beam remains separate from the positron beam and passes undisturbed through the HERMES area. A schematic diagram of the HERA collider is shown in Figure 3.1.

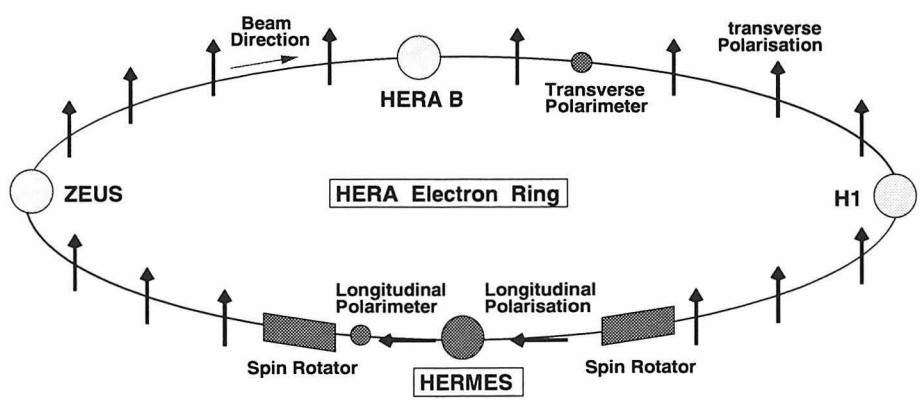

Figure 3.1: Schematic diagram of the HERA collider at DESY.

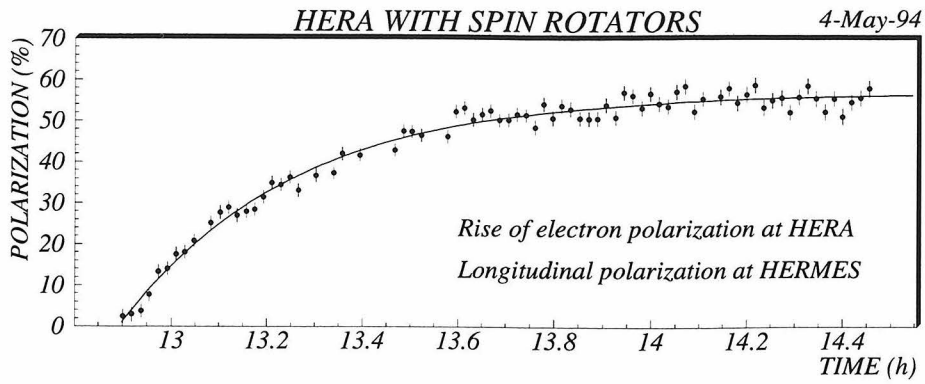

Figure 3.2: Time dependence of positron beam polarization.

3.2 Polarized e^+ Beam

High polarizations of the positron beam are reached in the HERA storage ring via the self–polarizing Sokolov–Ternov effect [30]. As the positrons travel through the storage ring, they emit synchotron radiation that has an asymmetric spin–flip amplitude which causes the beam to become polarized parallel to the fields of the bending magnets. This causes a transverse polarization to build up exponentially over a characteristic polarization rise time τ_p:

$$P_B(t) = P_{\max}(1 - \exp(-t/\tau_p))$$

The rise of the beam polarization in the positron ring is shown in Figure 3.2. Risetimes are typically about 30 minutes and the beam polarization reaches a maximum value of about 50%.

Longitudinal beam polarization is required for the HERMES experiment, and this was achieved via a pair of spin rotators [31] upstream and downstream of the East Hall. The longitudinal polarization was reversed for a portion of the 1997 data.

The beam polarization is measured with a transverse polarimeter [32] based on the Compton backscattering of polarized light. The Compton cross section is spin–dependent and causes a position asymmetry of the scattered photons with opposite polarizations. This asymmetry is measured with a calorimeter. A longitudinal polarization measurement in the region of the HERMES experiment supplements the

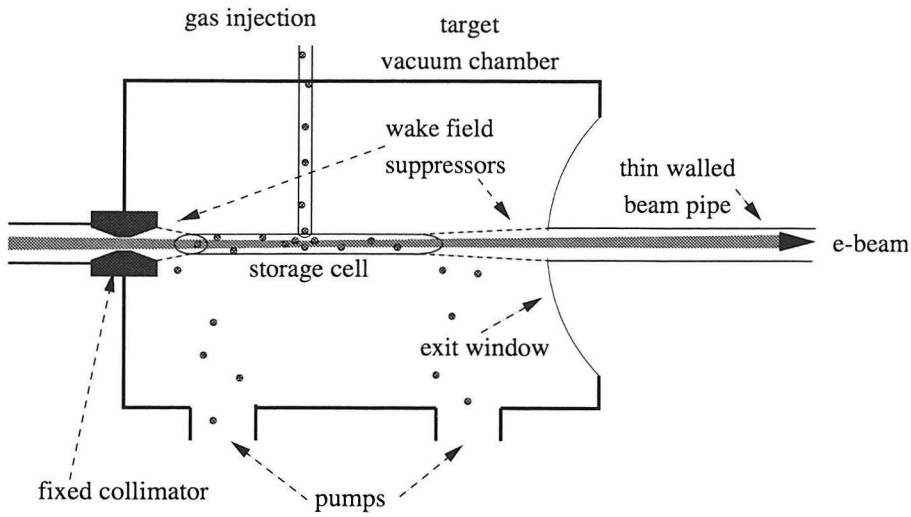

Figure 3.3: Schematic diagram of the target cell.

transverse polarization measurement. The Compton backscattering technique is used, but in this case an asymmetry in the energy distribution of the photons is measured. The locations of the polarimeters are shown in Figure 3.1.

3.3 Polarized Hydrogen Target

The HERMES polarized hydrogen target [33, 34, 35] is generated by an atomic beam source (ABS) that injects polarized hydrogen atoms into a target storage cell, shown schematically in Figure 3.3. Hydrogen atoms are generated in a RF dissociator and their electrons are polarized via Stern–Gerlach separation in a magnetic sextupole system. Adiabatic RF transitions are used to interchange hyperfine substate populations to produce proton polarization parallel or antiparallel to a static magnetic field oriented along the beam direction. The target polarization was reversed at intervals of either one or two minutes, chosen randomly. A 75 μm thick, 400 mm long ultrapure aluminum tube with elliptical cross section 29 mm wide by 9 mm high and cooled to approximately 100 K confines the injected polarized atoms to a small region about the positron beam to maximize the areal density. The atoms leak out the ends of the tube where they are pumped away to avoid further interference with the beam. Scattered particles exit the target chamber through a 0.3 mm stainless steel window.

The target polarization is monitored using a sample of the atoms in the target cell using a Breit–Rabi polarimeter (BRP). The sample is collected via a sampling tube connected to the target cell. The BRP uses adiabatic RF transitions, a sextupole magnet system, and a quadrupole mass spectrometer to count the population of atoms in the various hyperfine substates, allowing the electronic and nuclear polarizations to be calculated. The target polarization measurement is made with 2% statistical accuracy over 60 s.

The target proton polarization P_T is given by

$$P_T = \alpha_0[\alpha_r + (1 - \alpha_r)\beta]P_T^{\text{atom}}$$

where $P_T^{\text{atom}} = 0.92 \pm 0.03$ is the measured proton polarization of the atoms. $\alpha_0 = 0.99 \pm 0.01$ is the fraction of atomic protons, accounting for the small fraction of unpolarized molecules that appear in the target cell from the ABS and the vacuum system. The atomic fraction arising from molecules that are produced by recombination of atoms in the target cell is given by $(1-\alpha_r)$ with $\alpha_r = 0.93 \pm 0.04$. The relative numbers of atoms and molecules are measured using a target gas analyzer that sends a sample of the atoms and molecules from the target cell through a quadrupole mass spectrometer. β is the ratio of polarizations of protons in recombined molecules to atomic protons, and was determined to lie in the range $0.2 \leq \beta \leq 1.0$. The average target polarization P_T is 0.88 with a systematic uncertainty of 0.04.

3.4 Spectrometer

A schematic view of the HERMES spectrometer [36] is shown in Figure 3.4. The spectrometer is a forward angle device split into two identical halves above and below the plane containing the positron ring. The acceptance covers scattering angles within ± 170 mrad in the horizontal direction and within $\pm(40 - 140)$ mrad in the vertical direction. Particle momenta are measured with a series of tracking chambers upstream and downstream of a dipole magnet. The spectrometer is well suited for measurements

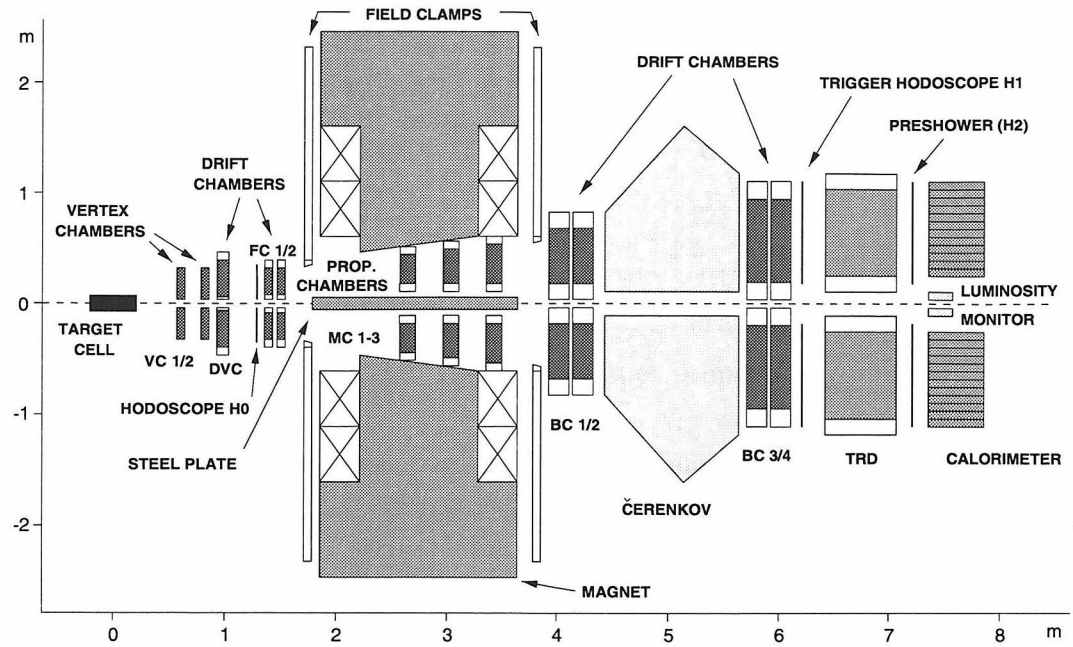

Figure 3.4: Schematic diagram of the HERMES spectrometer (side view).

of SIDIS, providing clean positron and pion identification.

3.4.1 Magnet

The HERMES dipole spectrometer magnet is an H–type with field clamps in front and behind to reduce fringe fields at the positions of the nearby drift chambers. A central, horizontal iron plate shields the positron and proton beams as they pass through the center of the magnet. The gap between the pole faces and the iron plate determines the geometrical acceptance of the spectrometer. The magnet is operated at a deflecting power of $\int Bdl = 1.3$ T·m.

3.4.2 Tracking

The tracking system is designed to measure the event vertex in the target, the scattering angles of charged particles, and the momentum of charged particles via the deflection through the spectrometer magnet. The system consists of a series of microstrip gas counters (vertex chambers), drift chambers (drift vertex chambers, front chambers, and back chambers), and proportional chambers (magnet chambers). The

	Vertex		Drift Vertex	Front		Back	
Name	VC1	VC2	DVC	FC1	FC2	BC1/2	BC3/4
mm from target	731	965	1100	1530	1650	4055	5800
Cell width (mm)	0.193	0.193	6	7	7	15	15
Gas Composition:	DME/Ne		$Ar/CO_2/CF_4$	$Ar/CO_2/CF_4$		$Ar/CO_2/CF_4$	
(%)	50/50		90/5/5	90/5/5		90/5/5	
Resolution/plane (μm)	65		220	225		275	300
Number of modules	1	1	1	1	1	2	2
Module configuration	VUX	XVU	XX'UU'VV'	UU'XX'VV'		UU'XX'VV'	
Channels/module	6014	6386	544	576	576	768	1152

Table 3.1: Tracking chamber properties.

properties of the tracking chambers used in the analysis of data presented in this thesis are summarized in Table 3.1. The chambers measure the track position in three different projections, the horizontal X direction and the U and V directions at ± 30 degrees from horizontal. Only the front chambers were used for tracking in the front region in the analysis of the 1996 data due to low efficiencies in the vertex chambers. For 1997 the drift vertex and vertex chambers were included in the tracking. The resolutions over the HERMES kinematic range for the momentum, x, and Q^2 are 0.7–1.25%, 4–8%, and 2%, respectively. Without the vertex chambers there is approximately a factor of 2 loss in resolution.

3.4.3 Particle Identification

Particle identification is provided by a combination of a lead glass calorimeter, a preshower hodoscope, a transition radiation detector (TRD), and a Čerenkov detector. A threshold Čerenkov was used in the 1996 and 1997 periods of data analyzed in this thesis, but was upgraded in 1998 to a ring–imaging Čerenkov (RICH). The RICH will be discussed in detail in Part II.

Preshower Hodoscope

The spectrometer contains two sets of hodoscopes [37] (H1 and H2), each hodoscope consisting of 42 overlapping vertical scintillator paddles. Each paddle is viewed by a photomultiplier. The scintillators provide a fast response to minimum ionizing particles. The paddles overlap to provide full acceptance. The preshower hodoscope (H2) is

preceded by a sheet of 1 cm thick lead (2 radiation lengths) to induce electromagnetic showers. Since the hadronic interaction length is much longer than the electromagnetic interaction length, positrons deposit much more energy in H2 (approximately 30 MeV) than hadrons (approximately 2 MeV), leading to a pion rejection factor of about 10 with 95% efficiency for positrons.

Calorimeter

A segmented lead glass calorimeter [38], consisting of two walls of 10 rows and 42 columns of radiation resistant lead glass bricks of dimensions $9 \times 9 \times 50$ cm^3, separates electrons from pions, measures the energies of electrons and photons, provides coarse position information, and contributes to the first–level trigger. Each block is viewed from the rear by a photomultiplier.

Like the preshower detector, the calorimeter exploits the difference between the radiation length for electron and photon showers and the (much longer) hadronic interaction length to separate particles by measuring differences in energy deposition. The calorimeter provides a pion rejection factor of 10 in the first–level trigger and 100 in offline analysis with an efficiency of 95% for positron detection.

The length scale of transverse shower energy deposition is given by the Moliere radius, which is approximately 3.3 cm in the HERMES calorimeter. Showers are largely contained within a single block, but a small amount of energy is deposited in surrounding blocks. Using the energies measured in a cluster of calorimeter blocks, the position of the shower can be calculated to within 0.7 cm.

TRD

The transition radiation detector (TRD) provides excellent pion rejection. It consists of two sets of six modules. Each module consists of a radiator followed by a multiwire proportional chamber filled with Xe/CH_4. The radiator consists of a pseudo–random matrix of polypropylene fibers. Relativistic particles crossing the boundary between media with different dielectric constants emit transition radiation at small angles. At

HERMES energies, only positrons emit transition radiation X-rays that can be detected by the proportional chambers. A pion rejection factor of about 150 is achieved with 90% positron efficiency.

Čerenkov

The threshold Čerenkov counter provides pion identification in a limited momentum range. The radiator is a mixture of 70% N_2 and 30% C_4F_{10} gas at atmospheric pressure. The momentum thresholds for pions, kaons, and protons are 3.8, 13.6, and 25.8 GeV, respectively. Čerenkov photons produced throughout the 1 m radiator length are focussed by an array of 20 spherical mirrors onto a corresponding array of 20 photomultiplier tubes. The photomultipliers are equipped with Winston light cones to maximize light collection.

3.4.4 Trigger

The HERMES DIS trigger is used to distinguish positron events from background with high efficiency. It is formed by requiring hits in three planes of scintillator hodoscopes and the calorimeter in coincidence with the accelerator bunch signal. In addition to the H1 and H2 hodoscopes, a forward scintillator H0 was used to reduce backgrounds from the HERA proton beam. The neutral particle background is suppressed with the requirement of signals in H0 and H1. The calorimeter suppresses charged hadronic and muonic background with a threshold (1.4 GeV) set above the minimum ionizing energy deposition (0.8 GeV).

3.4.5 Luminosity Monitor

The luminosity monitor exploits the measurement of well understood cross sections for Bhabha scattering and annihilation of positrons from electrons in the target. The reaction products are detected with a pair of calorimeters positioned to the left and right of the beam pipe 7.2 m downstream of the target. The horizontal acceptance is between 4.6 and 8.9 mrad. The symmetric scattering angle for a 27.5 GeV beam is

6.1 mrad with both particles having half the beam energy. Background processes are suppressed by requiring a coincident signal in both calorimeters of more than 5 GeV. The luminosity measurement has a statistical accuracy of 1% over a measurement period of 100 s. The primary use of the luminosity monitor is to provide a relative luminosity measurement between opposite target spin states rather than an absolute measurement.

Chapter 4 Data Analysis

4.1 Event Reconstruction

The task of the HERMES event reconstruction software (HRC) [39] is to use the raw drift chamber signals to locate tracks and to associate these tracks with signals in the particle identification detectors. In the track reconstruction, the straight partial tracks upstream and downstream of the spectrometer magnet are found using a tree search algorithm and linked together to form the full tracks. The momenta of the tracks are determined using a fast lookup table technique.

4.1.1 Tree Search Algorithm

The reconstruction program identifies particle tracks using hits in the tracking chambers. The partial tracks are found in each of three projections using a tree search algorithm, a process that proceeds in several stages. At the first stage, each detector plane is split into two equal segments, and each part is tested to see whether or not a hit is located within. Each part with a hit is split at the second stage into two more equal subsegments and each of these is tested in turn. This process is repeated a total of about 11 times until the sizes of the subsegments of the detector planes that remain are close to the detector resolution. At each stage of the tree search, the pattern of detector hits at the resulting resolution is tested to see if it contains a subpattern at the next stage's resolution that is consistent with an allowed track. The allowed patterns are generated during the initialization of the program, producing a set of lookup tables to avoid excessive calculation during the tree search.

The tree search algorithm would be very cumbersome if not for the use of some computational shortcuts. First, because the number of allowed subpatterns for a given pattern are strictly limited, the required number of comparisons is greatly reduced

by initializing the program with links between parent and child patterns. Once a pattern is recognized, only a few (4–8) subpatterns have to be checked to proceed to the following stage. Second, the number of patterns that must be stored is greatly reduced by symmetry considerations (translations and mirror reflections).

The tree search algorithm is used to reconstruct partial tracks in the U and V projections. The various combinations of these projections are tested against hits in the X coordinate to find the partial tracks in space. The partial tracks upstream and downstream of the spectrometer magnet are finally joined to produce full tracks.

4.1.2 Fast Momentum Lookup

The momentum of each track determines its deflection through the spectrometer magnet. The momentum could be calculated by extrapolating the straight partial tracks through the inhomogeneous magnetic field, but this is very CPU intensive. Instead, a lookup table is produced only once that contains the momentum as a function of track parameters upstream and downstream of the magnet, namely the position and slope of the track upstream of the magnet and the horizontal slope downstream. The table is filled with enough test cases to calculate the momentum with a precision better than 0.5%.

4.2 Particle Identification

Particle identification of a given track is achieved with a combination of signals in each of four detectors, exploiting the differences in the responses of the detectors to different types of particles. The first stage of the identification involves determining whether the track is a positron or a hadron. If the track is found to be a hadron, a further test on the Čerenkov signal determines whether it is a pion.

A likelihood method [40] is used to perform electron/hadron separation. The response of each detector D is converted into a conditional probability $\mathcal{L}_D^i$ that the response of the detector was caused by particle type i. This can be done using test beam data or very clean samples of each particle type using very restrictive cuts on

the other particle identification detectors. The PID parameter $PID3$ is defined as

$$\begin{aligned} PID3 &= PID_{\rm cal} + PID_{\rm pre} + PID_{\rm cer} \\ &= \log_{10}\left(\frac{\mathcal{L}^e_{\rm cal}\mathcal{L}^e_{\rm pre}\mathcal{L}^e_{\rm cer}}{\mathcal{L}^h_{\rm cal}\mathcal{L}^h_{\rm pre}\mathcal{L}^h_{\rm cer}}\right), \end{aligned}$$

taking into account the responses of the calorimeter, preshower, and Čerenkov detectors. The TRD response is contained in $PID5$.

$$\begin{aligned} PID5 &= PID_{\rm TRD} \\ &= \log_{10}\frac{\mathcal{L}^e_{\rm TRD}}{\mathcal{L}^h_{\rm TRD}} \end{aligned}$$

The combination $PID3 + PID5$ uses all four detectors simultaneously.

Positrons are selected using $PID3 + PID5 > 2.5$ and hadrons using $PID3 + PID5 < 0$. Pions are selected from the hadron sample between 4.9 and 13.5 GeV by requiring a minimum response of 0.25 photoelectrons in the Čerenkov detector. The efficiency and contamination of these cuts are discussed below.

4.3 Data Selection

4.3.1 Burst Selection

A burst is a division of the data lasting approximately ten seconds corresponding to readings of scaler and slow control inromation. It is the smallest time unit used in the analysis. The quality of the data is monitored from burst to burst and several quality requirements are imposed that filter out bursts in which the reliability of the data is suspect. These requirements place restrictions on the beam polarization, beam current, luminosity, and live time. Data quality analyses of individual detectors additionally select bursts in which the detectors are functioning normally. This selection eliminates periods of data that could be affected by drift chamber trips, drops in gain in calorimeter blocks or hodoscope paddles, or target malfunctions.

4.3.2 Event Selection

The cuts at the event level, outlined below, consist of fiducial cuts on the positron and pion tracks, particle identification cuts, and cuts to select the kinematic region of interest. The kinematic cuts are chosen to minimize acceptance variations while maintaining high statistics. The acceptance variations are limited to about 50% overall, and about 30% in regions with high statistics.

- Cuts on the positron

  1. Fiducial cuts

$$\begin{aligned} |\text{vertical scattering angle}| &> 40 \text{ mrad} \\ |\text{calorimeter x position}| &< 175 \text{ cm} \\ |\text{calorimeter y position}| &> 30 \text{ cm} \\ |\text{vertex z position}| &< 18 \text{ cm} \\ \text{vertex radius} &< 0.75 \text{ cm} \end{aligned}$$

     The first cut keeps the track well away from the horizontal septum plate. The second and third cuts ensure that the positron track strikes the calorimeter so that the shower is fully contained. The last two fiducial cuts constrain the location of the event vertex, defined as the distance of closest approach between the positron track and the beam axis. The longitudinal position of the vertex must lie within 18 cm of the center of the target and the transverse position within 0.75 cm of the beam axis.

  2. DIS cuts

$$\begin{aligned} Q^2 &> 1 \text{ GeV}^2 \\ W^2 &> 4 \text{ GeV}^2 \end{aligned}$$

     These cuts restrict the data sample to the region of deep inelastic scattering. The Q^2 cut allows an interpretation of the data in terms of a

quark-parton model while the W^2 cut avoids the resonance region.

3. $0.023 < x < 0.4$
4. PID3 + PID5 > 2.5
5. $y < 0.85$

   The y cut is used to exclude the region where radiative corrections and hadronic backgrounds can be large.

- Cuts on the pion

1. Fiducial cuts

$$\begin{aligned} |\text{vertical scattering angle}| &> 40 \text{ mrad} \\ |\text{calorimeter x position}| &< 175 \text{ cm} \\ |\text{calorimeter y position}| &> 33.5 \text{ cm} \end{aligned}$$

2. PID3 + PID5 < 0
3. $4.9 < p_\pi < 13.5$ GeV

   The lower momentum cut on the pions is chosen somewhat above the pion Čerenkov threshold. The Čerenkov efficiency at this momentum is approximately 80%. [41] By choosing the cut at this momentum, the acceptance variations are reduced to about 30% near the cut. Lowering the cut increases statistics substantially, but only at the expense of a very rapidly changing acceptance.

4. Čerenkov signal > 0.25 photoelectrons
5. Proximity cut

   The proximity cut is related to the spatial separation of tracks in the Čerenkov detector and is used to reduce hadronic contamination of the pion sample. It will be discussed in more detail in Section 4.6.3.

- Kinematic cuts on the pion/positron system

$$\begin{aligned} 0.2 &< z &< 0.9 \\ .05 &< p_\perp &< 1.3 \text{ GeV} \end{aligned}$$

The z cut restricts the kinematics so that the acceptance is large. The lower $p_\perp$ cut is used to allow an accurate measurement of ϕ.

4.4 Extraction of Analyzing Powers

The azimuthal angle ϕ is calculated as

$$\phi = \arccos\left(\frac{(\mathbf{q}\times\mathbf{k})\cdot(\mathbf{q}\times\mathbf{p}_\pi)}{|\mathbf{q}\times\mathbf{k}|\,|\mathbf{q}\times\mathbf{p}_\pi|}\right)\frac{\mathbf{p}_\pi\cdot\mathbf{q}\times\mathbf{k}}{|\mathbf{p}_\pi\cdot\mathbf{q}\times\mathbf{k}|}$$

in accordance with the convention of Figure 2.1.

Neglecting the spectrometer's resolution, the ϕ dependence of the yield of detected events is the product of the cross section times the integrated luminosity $L\sigma(\phi)$ and the acceptance $\epsilon(\phi)$. The yield, measured in each of four different beam/target helicity states, is labeled with the beam helicity λ_e and target helicity s_λ.

$$\begin{aligned} \frac{dN^{\lambda_e s_\lambda}}{d\phi} &= \frac{d(\sigma L)^{\lambda_e s_\lambda}}{d\phi}\epsilon(\phi) \\ \frac{d(\sigma L)^{\lambda_e s_\lambda}}{d\phi} &= L^{\lambda_e s_\lambda}\langle 1\rangle_{00} + L_{BT}^{\lambda_e s_\lambda}\langle 1\rangle_{LL} + \\ &\quad L_T^{\lambda_e s_\lambda}(2\langle\sin\phi\rangle_{0L} + 2\langle\sin\phi\rangle_{0T})\sin\phi + L_B^{\lambda_e s_\lambda}2\langle\sin\phi\rangle_{L0}\sin\phi + \\ &\quad L_T^{\lambda_e s_\lambda}(2\langle\sin 2\phi\rangle_{0L} + 2\langle\sin 2\phi\rangle_{0T})\sin 2\phi + \cdots \end{aligned}$$

Here $L^{\lambda_e s_\lambda}$ is the integrated luminosity in each beam/target spin state while $L_{B/T/BT}^{\lambda_e s_\lambda}$ is the integrated luminosity weighted by the beam/target/(beam×target) polarization.

It is convenient to write these functions as Fourier series.

$$\frac{2\pi}{\sigma L}\frac{d(\sigma L)}{d\phi} = 1 + \sum_m (a_m\cos m\phi + b_m\sin m\phi)$$

$$2\pi \frac{\epsilon(\phi)}{\int \epsilon(\phi) d\phi} = 1 + \sum_m (A_m \cos m\phi + B_m \sin m\phi)$$

Each Fourier coefficient of the yield, shown in Appendix D, depends on a complex mixture of the Fourier coefficients of σL and ϵ. For example, the $\sin\phi$ coefficient of the yield depends not only on the $\sin\phi$ coefficient of the cross section b_1, but also on the product $A_1 b_2$. In other words, the $\cos\phi$ component of the acceptance couples the $\sin 2\phi$ component of the cross section into the $\sin\phi$ component of the yield. As will be discussed below, the HERMES acceptance has a complicated ϕ dependence that depends strongly on kinematics, making the extraction of the various moments more difficult because of these coupling effects.

The normalized yield can be written

$$\frac{2\pi}{N}\frac{dN}{d\phi} = 1 + \sum_m (\alpha_m \cos m\phi + \beta_m \sin m\phi) .$$

The first moment of $\sin m\phi$,

$$\hat{\beta}_m = 2\frac{\sum_{i=1}^{N} \sin m\phi_i}{N},$$

is used to extract β_m. The sum is taken over all events i, and N is the number of events in the data sample. This is an unbiased estimator with variance

$$\sigma^2_{\beta_m} = \frac{2}{N}(1 - \alpha_{2m}/2 - \beta_m^2/2) \approx \frac{2}{N}.$$

Measurements of the moments are performed in each of the four different beam/target helicity states.

Due to acceptance effects, the $\sin m\phi$ moments are related to the analyzing powers $\mathcal{A}^{m\phi}$ in a complicated way. To illustrate, a simplified expression for $\hat{\beta}_1$ including only the most important contributions is shown below.

$$\beta_1^{\lambda_e s_\lambda} = \frac{1}{1 + \frac{1}{2}A_1 a_1} \frac{s_\lambda P_T \left[(1 - A_2/2)\mathcal{A}^{\phi} + \sum_{m>1}(A_{m-1}/2 - A_{m+1}/2)\mathcal{A}^{m\phi}\right]}{1 + \lambda_e s_\lambda P_B P_T \langle 1 \rangle_{LL} / \langle 1 \rangle_{00}}$$

$$a_1 = \frac{2}{1 + \lambda_e s_\lambda P_B P_T \langle 1 \rangle_{LL} / \langle 1 \rangle_{00}} \frac{\langle \cos\phi \rangle_{00}}{\langle 1 \rangle_{00}}$$

If $A_1 \ldots A_4$ are small, $\beta_1^{\lambda_e s_\lambda}$ will be dominated by $\mathcal{A}^\phi$.

The analyzing powers $\mathcal{A}^\phi \ldots \mathcal{A}^{3\phi}$ can be related to weighted averages of the moments $\hat{\beta}_1 \ldots \hat{\beta}_3$ measured in all beam/target states with a relative minus sign between measurements with opposite target spins.

$$\begin{aligned}
\overline{\beta}_m &= \frac{\sum_{\lambda_e s_\lambda} s_\lambda \left(\hat{\beta}_m / \sigma^2_{\beta_m} \right)^{\lambda_e s_\lambda}}{\sum_{\lambda_e s_\lambda} \left(1/\sigma^2_{\beta_m} \right)^{\lambda_e s_\lambda}} \\
&\approx 2 \frac{\sum_{\lambda_e s_\lambda} s_\lambda \sum_{i=1}^{N_{\lambda_e s_\lambda}} \sin m\phi_i}{\sum_{\lambda_e s_\lambda} N_{\lambda_e s_\lambda}} \\
&\equiv \sum_{n=1}^{3} \mathbf{M}_{mn} \mathcal{A}^{n\phi}
\end{aligned}$$

Effects which do not have a single target spin dependence largely cancel out in the average. Finally,

$$\mathcal{A}^{m\phi} = \sum_{n=1}^{3} \mathbf{M}^{-1}_{mn} \overline{\beta}_n$$

The analyzing powers are extracted as a function x, $p_\perp$, and z. x and z are chosen because the distribution and fragmentation functions are expressed primarily in terms of these variables so that the x and z dependence of the analyzing powers might provide clues as to the nature of the distribution and fragmentation processes separately. The data can be compared to some simple theoretical predictions for the expected $p_\perp$ behavior.

4.5 HERMES Monte Carlo

A Monte Carlo simulation of the HERMES experiment was employed to determine the Fourier coefficients of the acceptance, their dependence on kinematic variables, and the resolution of the spectrometer. The Monte Carlo software consists of gener-

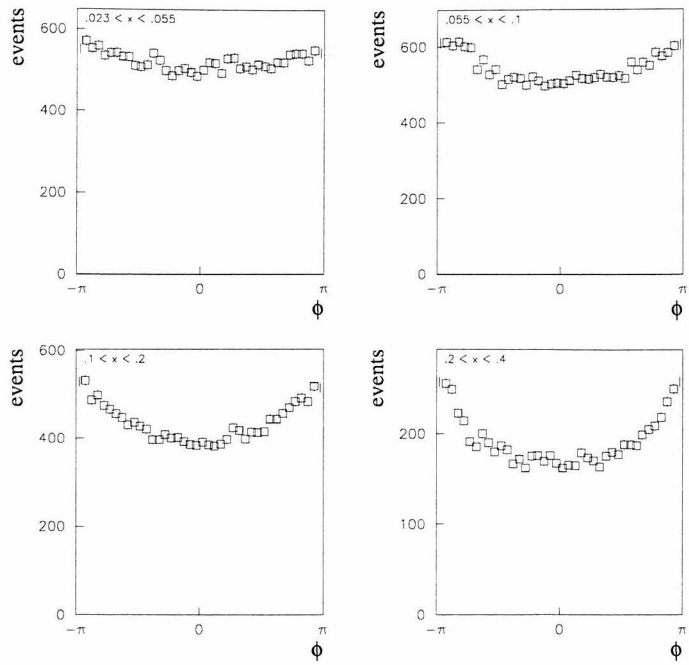

Figure 4.1: Generated π^+ azimuthal distributions.

ators for deep inelastic scattering and a GEANT-based simulation of the HERMES spectrometer and the passage of particles through the various detectors. The input cross section to the Monte Carlo does not include a a singly polarized azimuthal dependence, but only unpolarized or doubly polarized azimuthal dependences. The output of the Monte Carlo has the same structure of raw HERMES data and is processed in the analysis in identical fashion as the data.

Monte Carlo generated π^+ azimuthal distributions are shown in Figure 4.1 for four different x ranges. The distributions are asymmetric in the sense of being nonuniform in ϕ. This is due to the presence of unpolarized $\langle \cos\phi \rangle_{00}$ and $\langle \cos 2\phi \rangle_{00}$ terms in the physics input to the Monte Carlo. [42, 43] These unpolarized effects have been measured in deep inelastic muon-proton scattering [44, 45] and are described theoretically as a result of several kinds of influences including the intrinsic transverse momenta of quarks within the nucleon [46] and hard gluon emission by the quark before or after the interaction [47].

4.5.1 External Bremsstrahlung Correction

The observed ϕ distribution must be corrected for "instrumental" effects. That is, if ϕ_{MC} is the true ϕ, then for various reasons the reconstructed ϕ_{rec} may differ from ϕ_{MC}, and this must be taken into account when extracting the analyzing powers. The most obvious reason this happens is simply that the finite granularity of the tracking chambers makes impossible a perfect measurement of ϕ_{MC}.

Another reason, included in the same correction, is the influence of external bremsstrahlung processes. After the positron is scattered from a target proton, it may interact with material such as the target cell exit window in its path through the spectrometer, producing a real photon and reducing the positron's momentum. The kinematic quantities reconstructed using the momentum of the multiply scattered positron differ from their true values, in particular the reconstructed virtual photon momentum. This can alter the value of ϕ_{rec} considerably. The impact of the tracking chamber resolution is small in comparison to this effect, so the correction will be called an external bremsstrahlung correction.

The process of internal bremsstrahlung has no associated correction since it occurs in the primary interaction of the electron with the target. The azimuthal angle ϕ can only be consistently defined as the angle between the electron scattering plane and the hadron production plane, where the hadron production plane is calculated under the assumption that no internal bremsstrahlung occurs, i.e. the true virtual photon momentum coincides with $k - k'$. Therefore the occurrence of internal bremsstrahlung cannot alter ϕ. The two types of bremsstrahlung processes are illustrated in Figures 4.2 and 4.3.

Azimuthal distributions of accepted ϕ_{MC} and reconstructed ϕ_{rec} are plotted in Figure 4.4. The ϕ_{rec} distribution has a steeper "valley" than ϕ_{MC}. A shallower valley would be expected if only instrumental smearing effects came into play. In contrast, the external bremsstrahlung process tends to shift the reconstructed virtual photon momentum closer to the beam axis and therefore to move events away from zero and towards $\pm\pi$.

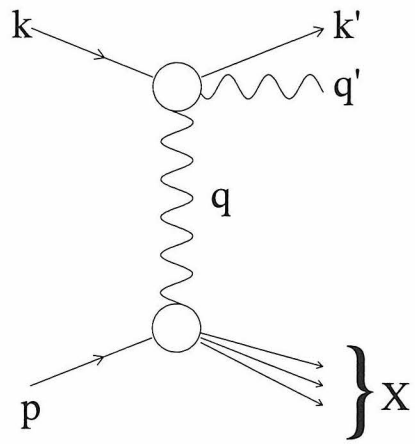

Figure 4.2: Illustration of internal bremsstrahlung. A real photon is emitted from the incoming or outgoing positron line.

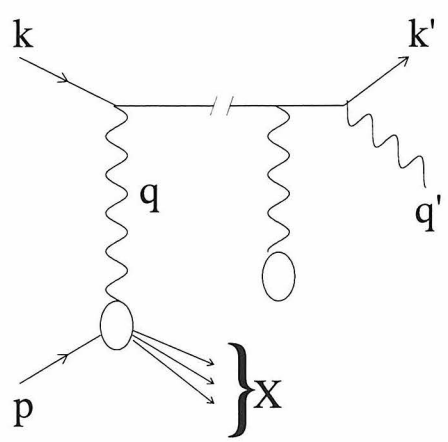

Figure 4.3: Illustration of external bremsstrahlung. After the deep inelastic scattering, the outgoing positron interacts incoherently with a second nucleus, emitting a real photon.

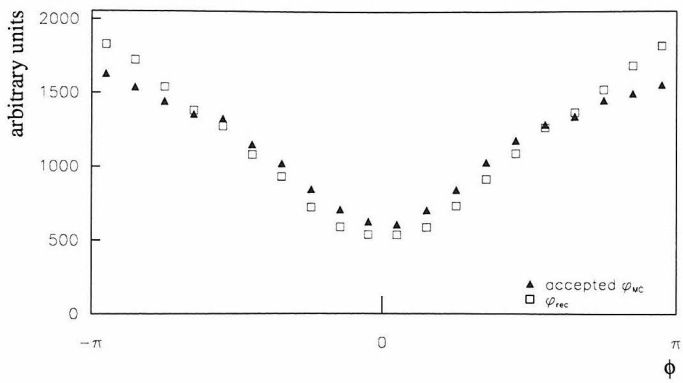

Figure 4.4: Azimuthal distributions of accepted $\phi_{\rm MC}$ and reconstructed $\phi_{\rm rec}$.

The Monte Carlo generated distributions have no $\sin m\phi$ components. Since the observables of interest are $\sin m\phi$ moments, the external bremsstrahlung correction cannot be corrected by simply determining the change in the $\sin m\phi$ moments of the accepted and reconstructed distributions. A solution is to apply an additional weight to the Monte Carlo events of the form (for the case $m = 1$)

$$1 + B \sin \phi_{\rm MC}$$

and study the dependence of the error introduced by external bremsstrahlung, given by

$$\begin{aligned} \delta &\equiv \langle \sin \phi_{\rm MC} \rangle - \langle \sin \phi_{\rm rec} \rangle \\ &= B/2 - B_{\rm rec}/2 \\ &= \frac{\sum_{i=1}^{N} (\sin \phi^i_{\rm MC} - \sin \phi^i_{\rm rec}) \, (1 + B \sin \phi^i_{\rm MC}) \, w_i}{\sum_{i=1}^{N} (1 + B \sin \phi^i_{\rm MC}) \, w_i} \end{aligned}$$

on the parameter B. In the last line the sum is over the N events labeled by i and w_i is the original Monte Carlo event weight. It can be seen from the last line that the error depends linearly on B for all practical purposes.

It is possible to exploit the fact that the moments are calculated in opposite target helicity states to determine the appropriate external bremsstrahlung correction. The

x range	$\langle \sin\phi \rangle$ correction	$\langle \sin 2\phi \rangle$ correction	$\langle \sin 3\phi \rangle$ correction
0.023–0.055	0.0181 ± 0.0006	0.0356 ± 0.0016	0.0457 ± 0.0022
0.055–0.100	0.0143 ± 0.0005	0.0446 ± 0.0018	0.0515 ± 0.0017
0.100–0.200	0.0102 ± 0.0006	0.0505 ± 0.0013	0.0625 ± 0.0012
0.200–0.400	0.0059 ± 0.0007	0.0495 ± 0.0016	0.0704 ± 0.0023

Table 4.1: Fractional external bremsstrahlung corrections to the analyzing powers for π^+ in four x bins.

$p_\perp$ range (GeV)	$\langle \sin\phi \rangle$ correction	$\langle \sin 2\phi \rangle$ correction	$\langle \sin 3\phi \rangle$ correction
0.05– 0.40	0.0106 ± 0.0004	0.0591 ± 0.0015	0.0691 ± 0.0018
0.40– 0.70	0.0159 ± 0.0006	0.0285 ± 0.0010	0.0383 ± 0.0017
0.70– 0.95	0.0204 ± 0.0013	0.0219 ± 0.0019	0.0386 ± 0.0034
0.95– 1.30	0.0214 ± 0.0016	0.0258 ± 0.0010	0.0336 ± 0.0023

Table 4.2: Fractional external bremsstrahlung corrections to the analyzing powers for π^+ in four $p_\perp$ bins.

following quantity is used as an estimator for B

$$\begin{aligned} \hat{B} &= B^+_{\rm rec}/2 - B^-_{\rm rec}/2 \\ &= (B^+ - B^-)/2 - (\delta^+ - \delta^-) \end{aligned}$$

where the $\pm$ superscripts represent the target helicity state and $B^\pm = \pm B$. Thus the fractional correction is given by

$$\begin{aligned} \frac{B - \hat{B}}{B} &= \frac{\delta^+ - \delta^-}{B} \\ &= \frac{d\delta}{dB} \\ &\approx \frac{\sum_{i=1}^N (\sin\phi^i_{\rm MC} - \sin\phi^i_{\rm rec}) \sin\phi^i_{\rm MC} w_i}{\sum_{i=1}^N w_i}, \end{aligned}$$

which is easily calculated in the Monte Carlo. The external bremsstrahlung corrections are shown in Table 4.1 for the first three $\sin m\phi$ moments for π^+ in four x bins, in Table 4.2 in four $p_\perp$ bins, and in Table 4.3 in four z bins. The size of the corrections tends to be slightly smaller for π^-. The size of the corrections increases from about 1-2% for $m = 1$ to 4-7% for $m = 2$ or 3.

z range	$\langle \sin\phi \rangle$ correction	$\langle \sin 2\phi \rangle$ correction	$\langle \sin 3\phi \rangle$ correction
0.20– 0.30	0.0120 ± 0.0003	0.0266 ± 0.0018	0.0290 ± 0.0010
0.30– 0.40	0.0175 ± 0.0007	0.0444 ± 0.0007	0.0456 ± 0.0020
0.40– 0.55	0.0161 ± 0.0007	0.0496 ± 0.0014	0.0605 ± 0.0017
0.55– 0.90	0.0094 ± 0.0008	0.0445 ± 0.0014	0.0632 ± 0.0025

Table 4.3: Fractional external bremsstrahlung corrections to the analyzing powers for π^+ in four z bins.

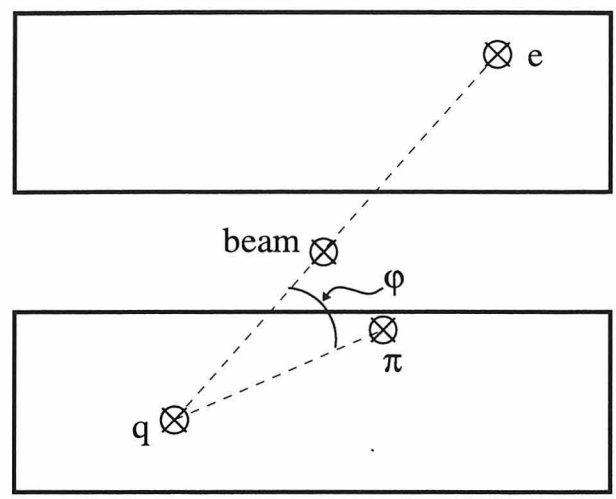

Figure 4.5: Illustration of the HERMES acceptance.

4.5.2 Acceptance Calculation

The most important characteristic of the HERMES acceptance for the purpose of calculating analyzing powers is the presence of the central horizontal shielding plate in the spectrometer magnet that prohibits the detection of particles scattered near the horizontal midplane. Figure 4.5 illustrates the HERMES acceptance, with two boxes representing the two halves of the HERMES spectrometer. The incoming beam, scattered positron, virtual photon, electroproduced pion, and the azimuthal angle ϕ are shown. Pions produced at small lab angles with respect to the positron beam go undetected, and these undetected pions are concentrated at values of ϕ near zero.

Reconstructed π^+ azimuthal distributions for both the data and the Monte Carlo are shown in Figure 4.6. The agreement between the data and Monte Carlo is satisfactory. The distributions are shown in four different x ranges and illustrate the rapidly varying nature of the acceptance. The general features can be understood

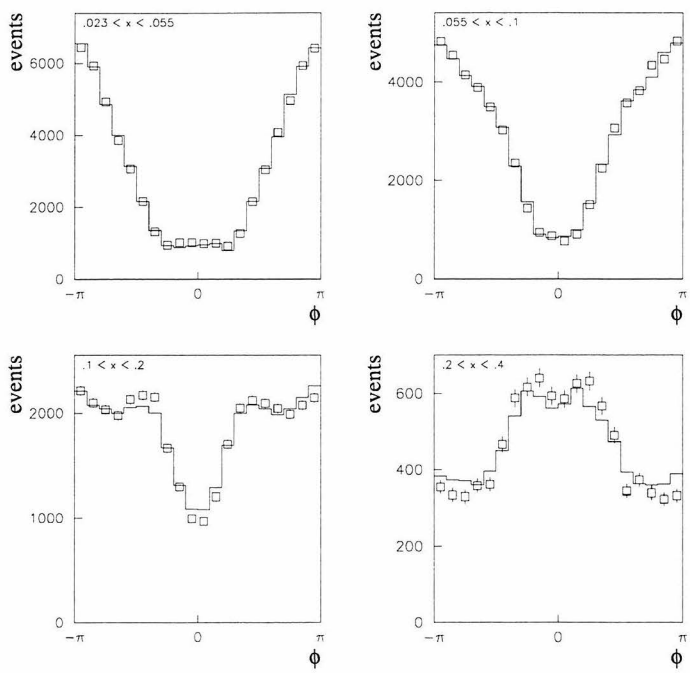

Figure 4.6: Reconstructed π^+ azimuthal distributions in four different x ranges. Histograms are Monte Carlo and squares are data. The statistical error on the Monte Carlo is roughly comparable to that of the data.

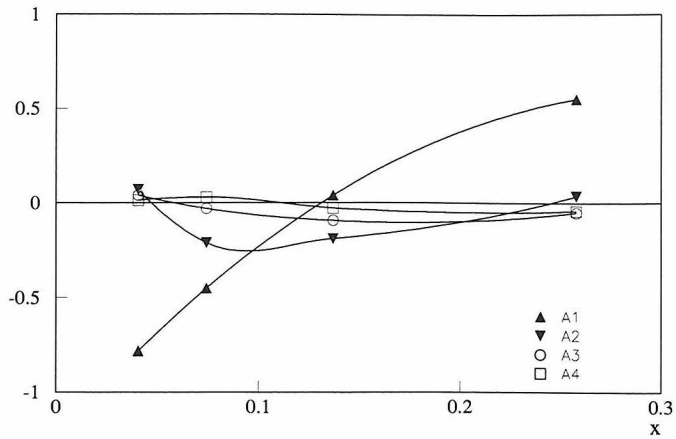

Figure 4.7: Fourier coefficients of the HERMES acceptance as a function of x. Curves are drawn to guide the eye.

as the result of the lab angle of the virtual photon increasing with increasing x. For small lab angles, the acceptance is low for ϕ near zero as discussed above, while for large lab angles, the acceptance is low for ϕ near $\pm\pi$.

The acceptance is calculated using the generated and accepted Monte Carlo azimuthal distributions and fit with a sum of trigonometric functions to extract the Fourier components. The first four even components $A_1, \ldots, A_4$ are plotted in Figure 4.7. The odd components are consistent with zero as expected. The large magnitude of A_1 is the most important feature of the HERMES acceptance, giving rise to a relatively strong coupling of the $\sin 2\phi$ component of the cross section with the $\sin\phi$ component of the yield. Therefore, the largest acceptance corrections are to be expected at low and high x. Figures 4.8 and 4.9 show the acceptance as a function of $p_\perp$ and z, respectively.

4.6 Systematic Errors

The systematic error of the analyzing power measurement comes from several sources, including the target polarization uncertainty, uncertainties in the acceptance and cross sections that enter in the analyzing power extraction, contaminations of the positron

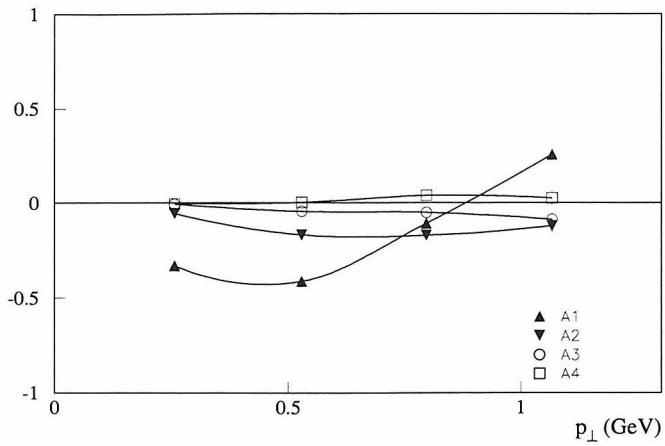

Figure 4.8: Fourier coefficients of the HERMES acceptance as a function of $p_\perp$. Curves are drawn to guide the eye.

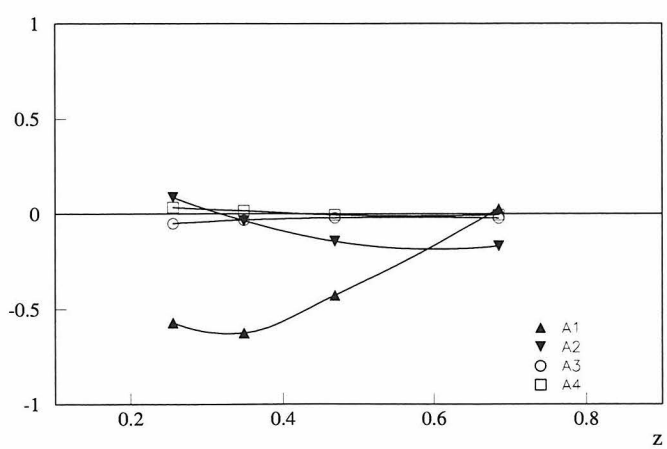

Figure 4.9: Fourier coefficients of the HERMES acceptance as a function of z. Curves are drawn to guide the eye.

and pion samples, and radiative corrections.

4.6.1 Target Polarization

The systematic error on the target polarization was discussed in Section 3.3. The fractional error due to this uncertainty is 5%.

4.6.2 Acceptance and Cross Section Uncertainties

Systematic errors of ± 0.1 and ± 0.02 are applied to the even and odd Fourier coefficients of the acceptance, respectively. The Monte Carlo events are generated with cuts on the scattering angle of the positrons such that they lie approximately within the HERMES spectrometer acceptance. The systematic errors account for the differences between the azimuthal distributions with and without these cuts. The contribution to the systematic error of the analyzing powers depends strongly on kinematics, with a maximum contribution of about $\pm 15\%$ in the lowest x bin.

Knowledge of both polarized and unpolarized cross sections is required to extract the analyzing powers. The most important of these are the unpolarized, $\cos m\phi$ dependent cross sections $\langle \cos m\phi \rangle \,/\, \langle 1 \rangle_{00}$ and the double polarized, ϕ independent cross section $\langle 1 \rangle_{LL} \,/\, \langle 1 \rangle_{00}$. These are calculated with the data. The $\cos m\phi$ dependent cross sections are extracted by calculating moments of $\cos m\phi$ summed over all helicity states and applying acceptance and external bremsstrahlung corrections. The ϕ independent cross section is calculated using a double spin asymmetry. The statistical uncertainties of these cross sections are included as systematic errors.

4.6.3 Contaminations

Contamination of the Positron Sample

The hadronic contamination of the positron sample was calculated by constructing distributions of the PID likelihood parameter $PID3 + PID5$. The hadrons appear at low likelihoods and positrons at high likelihoods. A small number of hadrons are

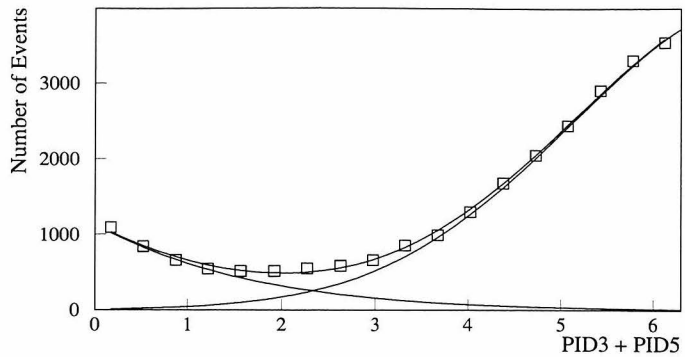

Figure 4.10: Illustration of the calculation of the hadronic contamination of the positron sample.

found above the positron cut at $PID3 + PID5 = 2.5$. This number is calculated by fitting the distributions with a sum of two gaussians in the neighborhood of the valley at the positron cut. [40] A sample is shown in Figure 4.10.

The positron sample is also contaminated by non-DIS positrons. These positrons are assumed to originate from charge symmetric processes, so the yield can be estimated as the yield of electrons that pass all the required lepton identification and DIS cuts. The electron sample, however, is contaminated by pions, and since the flux of electrons is very low, the contamination can be very large. In order to avoid overestimating the charge symmetric background, it is necessary to calculate the pion contamination of the electron sample and subtract it. The pion contamination of the electron sample was calculated in identical fashion as the positron sample and found to be more than 20%.

The processes which contaminate the positron analyzing power are assumed to have zero analyzing power with an uncertainty of $\pm 5\%$. The contaminations are shown in Table 4.4. The same contaminations are shown as a function of $p_\perp$ in Table 4.5 and as a function of z in Table 4.6. The total contamination is about 4% at low z. A dilution correction is applied to the analyzing power and an absolute systematic uncertainty depending on the contamination level is calculated. Since the worst case contamination is about 4%, the absolute systematic error is at most 0.002.

x range	hadronic	non-DIS
0.023–0.055	0.014	0.010
0.055–0.100	0.009	0.002
0.100–0.200	0.010	0
0.200–0.400	0.010	0

Table 4.4: Contamination of positron samples by hadrons and non-DIS positrons in four x bins. The hadronic contaminations in the third and fourth x bins are not well determined due to low statistics, so the values shown are considered to be conservative estimates. The non-DIS positron contaminations in the third and fourth bins are negligible.

$p_\perp$ range (GeV)	hadronic	non-DIS
0.05–0.4	0.008	0.002
0.4–0.7	0.010	0.006
0.7–0.95	0.012	0.006
0.95–1.3	0.011	0.012

Table 4.5: Contamination of positron samples by hadrons and non-DIS positrons in four $p_\perp$ bins.

Contamination of the Pion Sample

The pion sample has two sources of contamination. The first is muons that activate the Čerenkov but have hadron-like signatures in other PID detectors. The second is due to kaons and protons whose trajectories lie close to a pion or lepton trajectory.

z range	hadronic	non-DIS
0.20–0.30	0.018	0.022
0.30–0.40	0.009	0.003
0.40–0.55	0.010	0
0.55–0.90	0.010	0

Table 4.6: Contamination of positron samples by hadrons and non-DIS positrons in four z bins. The hadronic contaminations in the third and fourth z bins are not well determined due to low statistics, so the values shown are considered to be conservative estimates. The non-DIS positron contaminations in the third and fourth bins are negligible.

x range	μ^+/π^+	μ^-/π^-	p or K^+ / π^+	$\overline{p}$ or K^- / π^-
0.023–0.055	0.0044	0.0044	0.0102	0.0056
0.055–0.100	0.0045	0.0039	0.0065	0.0035
0.100–0.200	0.0050	0.0034	0.0050	0.0021
0.200–0.400	0.0047	0.0028	0.0044	0.0015

Table 4.7: Contamination of pion samples by muons and protons/kaons in four x bins.

$p_\perp$ range (GeV)	μ^+/π^+	μ^-/π^-	p or K^+ / π^+	$\overline{p}$ or K^- / π^-
0.05– 0.40	0.0056	0.0042	0.0058	0.0029
0.40– 0.70	0.0038	0.0038	0.0072	0.0036
0.70– 0.95	0.0023	0.0035	0.0113	0.0067
0.95– 1.30	0.0033	0.0012	0.0140	0.0090

Table 4.8: Contamination of pion samples by muons and protons/kaons in four $p_\perp$ bins.

Since the threshold Čerenkov detector is only coarsely segmented, the signal from the lepton or pion track is associated with the nearby kaon or proton track so that it passes for a pion. This second source of contamination is substantially reduced by a proximity cut on pion candidates. This cut requires that the pion candidate be the only track to intersect the Čerenkov mirror, ensuring that the Čerenkov signal is generated by the pion candidate alone. The proximity cut is unable to completely eliminate the hadronic background because it is possible for an unreconstructed track such as a delta electron to produce the Čerenkov signal. The contaminations were calculated using the HERMES Monte Carlo program. The results are shown in four x bins in Table 4.7, in four $p_\perp$ bins in Table 4.8, and in four z bins in Table 4.9.

z range	μ^+/π^+	μ^-/π^-	p or K^+ / π^+	$\overline{p}$ or K^- / π^-
0.20– 0.30	0.0055	0.0066	0.0162	0.0070
0.30– 0.40	0.0056	0.0045	0.0113	0.0054
0.40– 0.55	0.0052	0.0037	0.0059	0.0028
0.55– 0.90	0.0033	0.0024	0.0021	0.0017

Table 4.9: Contamination of pion samples by muons and protons/kaons in four z bins.

x range	$\pi^+/(p, K^+)$	$\pi^-/(\overline{p}, K^-)$
.023–.055	.12	.19
.055–.100	.12	.21
.100–.200	.12	.24
.200–.400	.11	.30

Table 4.10: Contamination of proton/kaon samples by pions in four x bins.

In order to assign a systematic error for the contamination of the pion sample, it is necessary to have an estimate of the analyzing power for the various sources of contamination. In the case of muons, it is likely that the analyzing power is small compared to the pions. The muons come from decaying particles that may have a nonzero analyzing power, but the decay process will tend to wash out the ϕ distribution.

The analyzing power of kaon and proton production is potentially large. It was measured in similar fashion as the pions in order to rule out a very large contaminating effect. The sample of protons and kaons was obtained with the requirement that the Čerenkov signal be less than 0.25 photoelectrons. Due to the inefficiency of the Čerenkov, this sample is significantly contaminated by pions, but is still useful for the purpose of assigning a limit to the size of the kaon and proton analyzing power. The pion contaminations of the proton and kaon samples are shown in Table 4.10. The uncorrected analyzing powers $\overline{\beta}_1$ and $\overline{\beta}_2$ for the p/K^+ sample are shown as a function of x in Figure 4.11. The results for $\overline{\beta}_1$ are significantly positive. The uncorrected $\overline{p}/K^-$ analyzing powers are shown in Figure 4.12.

Based on these measurements, it is assumed that all muon, proton, and kaon analyzing powers are less than 10%. Since the worst case contamination is about 1.5%, the absolute systematic error is at most 0.0015.

4.6.4 Radiative Corrections

A number of radiative processes including internal bremsstrahlung, vertex corrections, and two photon exchange contribute to the electroproduction cross section. On the

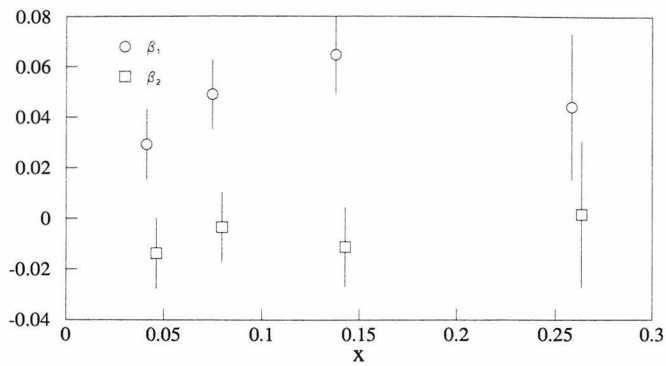

Figure 4.11: Uncorrected analyzing powers of the p/K^+ sample as a function of x.

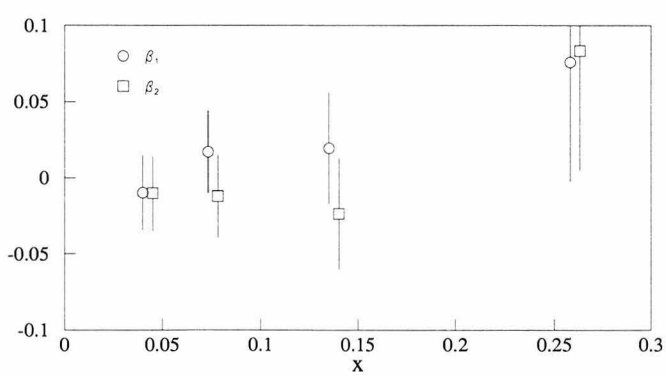

Figure 4.12: Uncorrected analyzing powers of the $\overline{p}/K^-$ sample as a function of x.

source	error
Target polarization	5% relative
Contamination of positrons	0.002 absolute
Contamination of pions	0.0015 absolute
Acceptance	15% relative

Table 4.11: Summary of major contributions to the overall systematic error.

other hand, the description of the SIDIS process is made in terms of the single photon exchange diagram. To extract the single photon exchange cross section from the observed cross section, these radiative processes must be calculated and a correction applied. Radiative corrections have been calculated for unpolarized semi-inclusive processes with nontrivial azimuthal dependence. [48] For the $\sin\phi$ dependent cross section, the radiative corrections do not exceed 0.01%. In this thesis it will be assumed that polarized radiative corrections are negligible.

4.6.5 Summary of Systematic Errors

The principal sources of systematic error are summarized in Table 4.11. The sizes of the contamination effects can vary with kinematics considerably, and the values shown represent worst case values, typically appearing at low x or z or high $p_\perp$.

Chapter 5 Results and Interpretation

5.1 ϕ Dependent Single Target Spin Asymmetry

The ϕ dependence of the single spin effect can be illustrated straightforwardly by calculating the following asymmetry

$$A(\phi) = \frac{N^- L^+ - N^+ L^-}{N^- L_T^+ + N^+ L_T^-} \tag{5.1}$$

$N^+(N^-)$ is the number of events for target spin parallel(antiparallel) to the beam momentum. $L^\pm$ and $L_T^\pm$ are the deadtime corrected integrated luminosity for each target spin state with the latter weighted by the target polarization for each target spin state.

While the above asymmetry can show the sensitivity of the data, it is not used in extracting the analyzing power. It is possible to evaluate moments of the above asymmetry as $\int \sin m\phi A(\phi) d\phi$ with numerically similar results as the technique presented in the previous chapter, but the evaluation of systematic effects is more difficult.

The single spin asymmetries are shown for π^+ and π^- in Figure 5.1. Both asymmetries are adequately fit with a $\sin\phi$ dependence. The π^+ asymmetry oscillates with an amplitude of over 2% while the π^- asymmetry has zero amplitude within experimental errors. The average asymmetries (fit parameter P_1) reflect the azimuthally averaged asymmetry which is dominated by the double polarized, ϕ independent cross section, roughly proportional to $g_1 D_1 / f_1 D_1$. Since the data are averaged over roughly but not exactly equal periods with opposite beam helicity, the double polarized term nearly cancels out.

With Figure 5.1 it is already possible to point out the most important features of the data assuming that acceptance effects are reasonably small. First, the sign of the effect is in agreement with the results of the E704 experiment. Based on Figure 5.1 and

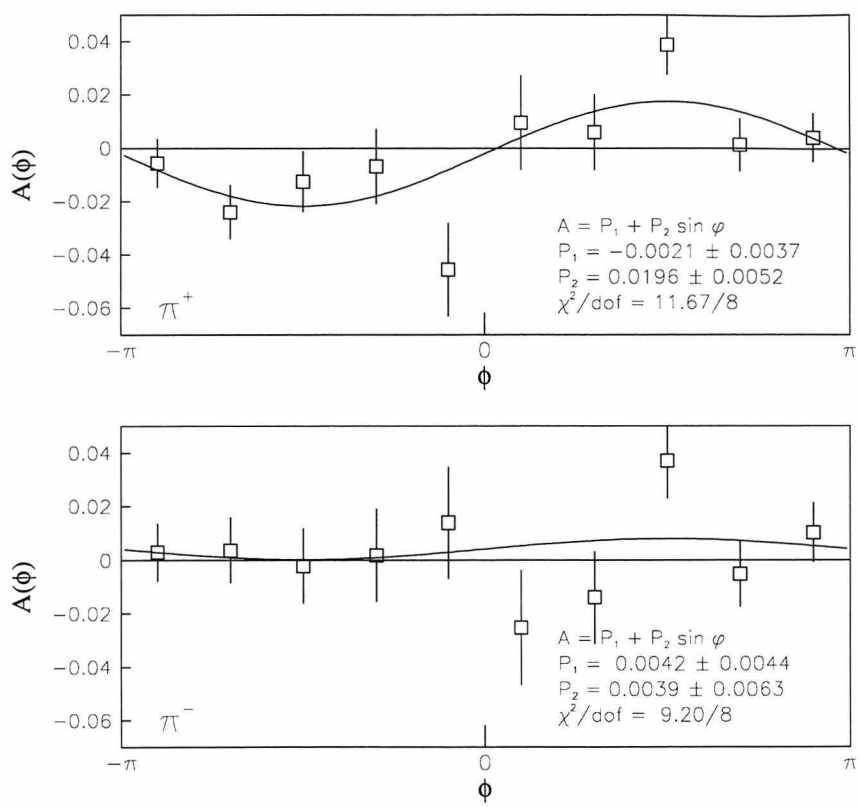

Figure 5.1: Single spin asymmetries $A(\phi)$ for π^+ and π^-.

Equation 5.1, positively charged pions favor $\phi > 0$ for target polarization antiparallel to the virtual photon. That is, for an upwardly polarized proton, positively charged pions favor production towards the left, in agreement with the E704 results shown in Figure 2.6.

Second, the difference in magnitude between the π^+ and π^- can be explained by the fact that the virtual photon couples four times more strongly to u quarks than d quarks based on the ratio of their squared charges. Since the u quarks and d quarks tend to fragment into π^+ and π^-, respectively, one would expect the size of the π^+ to be roughly four times larger than the π^-, with opposite signs reflecting the opposite polarizations of the valence u and d quarks. In the case of E704, the interaction takes place through gluon exchange with equal couplings for u and d quarks, so the magnitudes of the analyzing powers are comparable.

Third, it is clear that the $\sin\phi$ Fourier component of the asymmetry dominates over $\sin 2\phi$ or any other component. Naively, this might be a surprising result because it is the $\sin 2\phi$ component of the cross section that appears at leading twist in σ_{0L}. The $\sin\phi$ component is twist-3 in σ_{0L} and twist-2 in σ_{0T} where it is multiplied by $|\mathbf{S}_T|$. However, the twist-3 cross sections are multiplied by Q_T/Q (where $Q_T \equiv p_\perp/z$), which at HERMES kinematics amounts to only a small suppression.

5.2 Analyzing Powers

The analyzing power $\mathcal{A}^\phi$ is shown for π^+ and π^- as a function of x in Figure 5.2. The analyzing power is compared with the $\sin\phi$ component of the single target spin asymmetry (Equation 5.1) in Figure 5.3. The difference between every set of points is small, demonstrating the near equivalence of the two techniques and the small impact of acceptance and bremsstrahlung corrections.

The analyzing power for the π^+ is nonzero throughout the entire range of x and shows a hint of increasing behavior with x. The π^- analyzing power is consistent with zero through the entire x range.

The major contributing influences to the analyzing power appear at $1/Q$ because

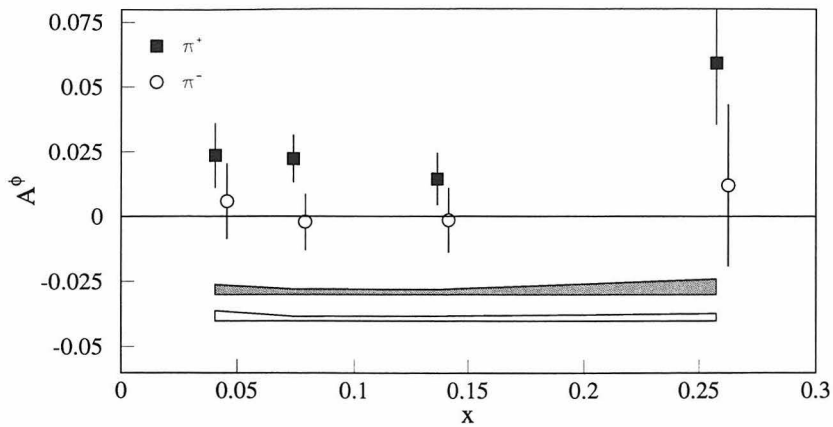

Figure 5.2: Analyzing power $\mathcal{A}^\phi$ for π^+ and π^- as a function of x. The upper band represents the systematic error on the π^+ measurement and the lower band the systematic error on the π^- measurement. The x values for π^- are offset by 0.005 for clarity.

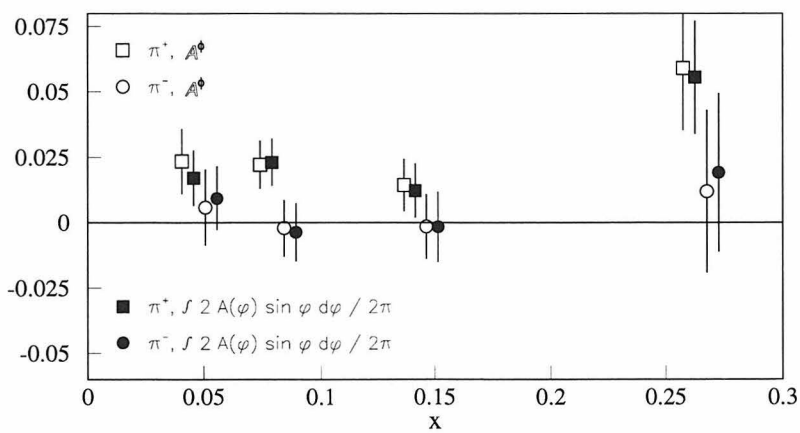

Figure 5.3: Analyzing power $\mathcal{A}^\phi$ for π^+ and π^- as a function of x compared with $\int \sin m\phi A(\phi) d\phi$. Points are offset in x for clarity.

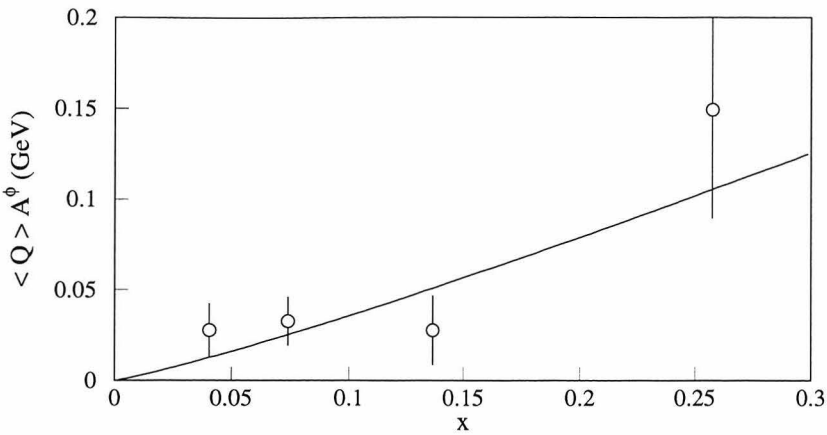

Figure 5.4: Analyzing power $\mathcal{A}^{\phi}$ for π^+ function of x multiplied by $\langle Q \rangle$. The curve represents the function xg_1/f_1, arbitrarily normalized.

they are either subleading twist or are multiplied by $\mathbf{S}_\perp$. Figure 5.4 shows the π^+ analyzing power multiplied by the average value of Q in each x bin. The x dependence of the resulting weighted analyzing power behaves roughly as $xh_1(x)/f_1(x)$. If the x dependence of h_1 is approximated using the longitudinal polarized distribution $g_1^{u_V}(x)$ for valence u quarks, the x dependence of the analyzing power becomes

$$\mathcal{A}^{\phi} \sim xg_1^{u_V}/f_1^{u_V} \sim x \times x^{0.18}$$

where parametrizations [49] of polarized distributions based on fits to world data are used in the second approximation. The result is shown as a curve in Figure 5.4 and is in agreement with the data. The agreement suggests that the analyzing power is dominated by valence quarks rather than sea quarks as has been assumed in most theoretical interpretations of the hadron-hadron single spin asymmetries.

The results for $\mathcal{A}^{\phi}$ are roughly comparable to the raw analyzing power of the proton and K^+ sample shown in Figure 4.11. Since the pion contamination of the proton and K^+ data is only 10%, there is a strong suggestion of a nonzero analyzing power in proton and/or K^+ electroproduction. Kaon analyzing powers comparable to those of pions are predicted in recent theoretical studies [21].

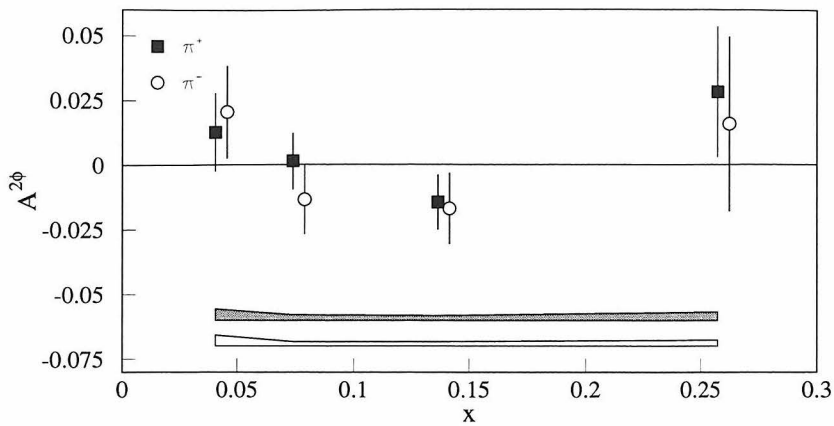

Figure 5.5: Analyzing power $\mathcal{A}^{2\phi}$ for π^+ and π^- as a function of x. The upper band represents the systematic error on the π^+ measurement and the lower band the systematic error on the π^- measurement. The x values for π^- are offset by 0.005 for clarity.

The analyzing power $\mathcal{A}^{2\phi}$ is shown for π^+ and π^- as a function of x in Figure 5.5. The analyzing power is consistent with zero in all cases. $\mathcal{A}^{3\phi}$ was also found to be consistent with zero.

The analyzing power $\mathcal{A}^{\phi}$ is shown for π^+ and π^- as a function of $p_\perp$ in Figure 5.6. For the π^+ case there is strong evidence for increasing behavior with $p_\perp$. The size of the analyzing power is constrained kinematically to be zero at $p_\perp = 0$. It is expected to reach a maximum at a $Q_T = p_\perp/z$ scale of the order of a typical hadronic mass [12] or hadronic radius [3]. The analyzing power should decrease at high $p_\perp$ where perturbative QCD applies and collinear parton configurations dominate. The analyzing power $\mathcal{A}^{2\phi}$ is shown for π^+ and π^- as a function of $p_\perp$ in Figure 5.7. It is consistent with zero within errors in all cases.

Finally, the z dependence of the analyzing powers is shown in Figures 5.8 and 5.9. $\mathcal{A}^{\phi}$ is nonzero and shows no clear z dependence in the π^+ channel. The other analyzing powers are consistent with zero.

The results of this Section are listed in Tables 5.1 through 5.6.

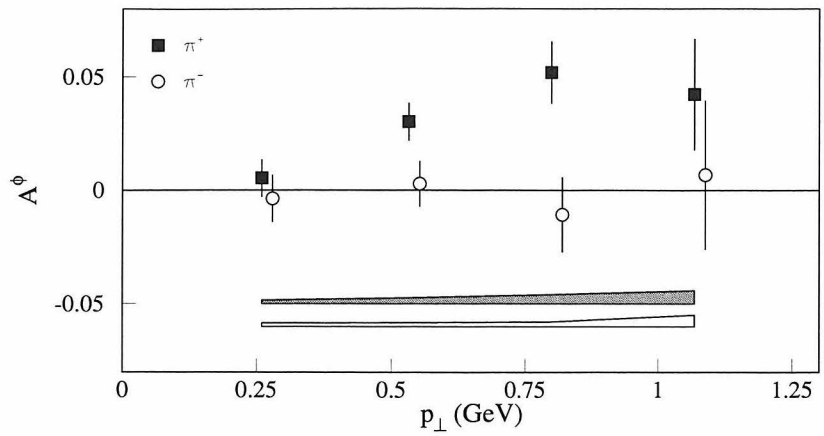

Figure 5.6: Analyzing power $\mathcal{A}^{\phi}$ for π^+ and π^- as a function of $p_\perp$. The upper band represents the systematic error on the π^+ measurement and the lower band the systematic error on the π^- measurement. The $p_\perp$ values for π^- are offset by 0.02 for clarity.

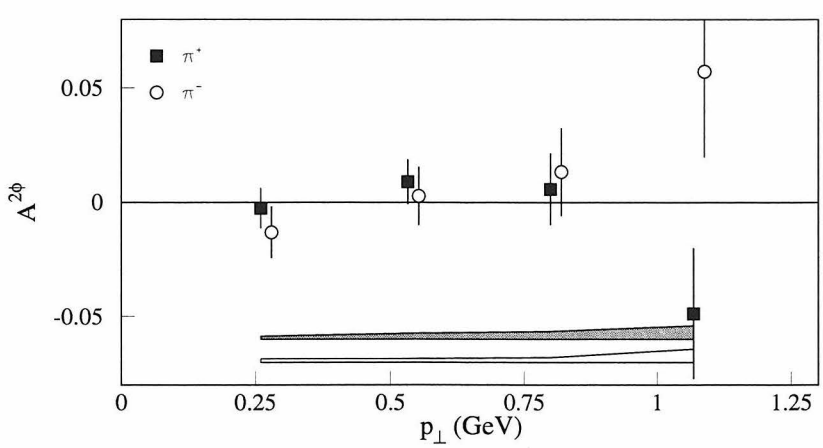

Figure 5.7: Analyzing power $\mathcal{A}^{2\phi}$ for π^+ and π^- as a function of $p_\perp$. The upper band represents the systematic error on the π^+ measurement and the lower band the systematic error on the π^- measurement. The $p_\perp$ values for π^- are offset by 0.02 for clarity.

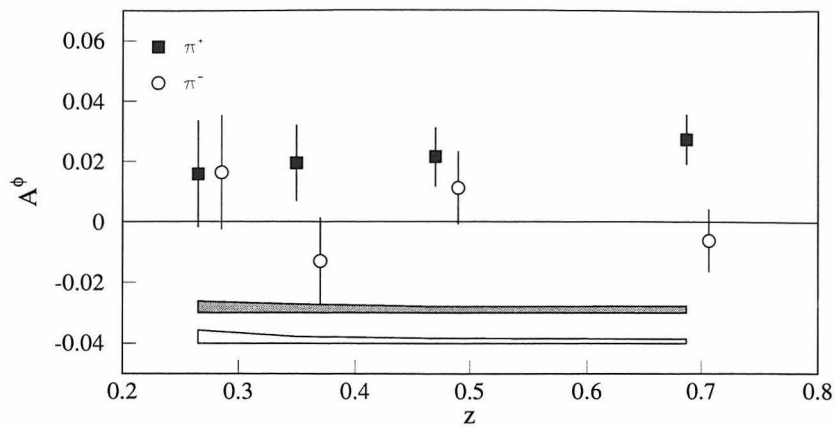

Figure 5.8: Analyzing power $\mathcal{A}^{\phi}$ for π^+ and π^- as a function of z. The upper band represents the systematic error on the π^+ measurement and the lower band the systematic error on the π^- measurement. The z values for π^- are offset by 0.02 for clarity.

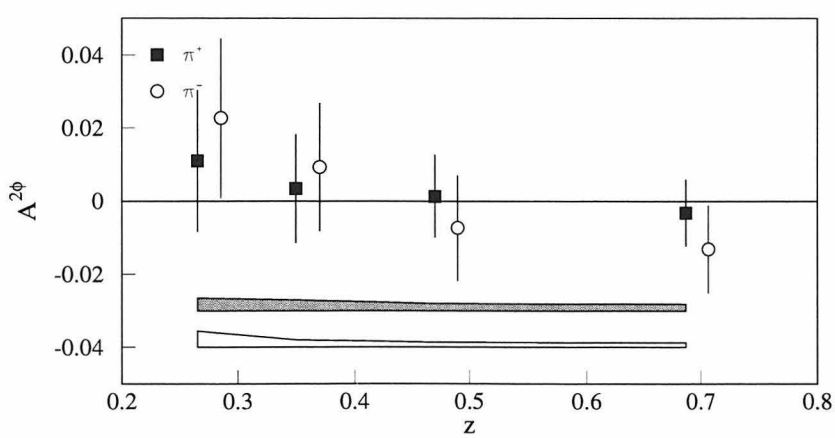

Figure 5.9: Analyzing power $\mathcal{A}^{2\phi}$ for π^+ and π^- as a function of z. The upper band represents the systematic error on the π^+ measurement and the lower band the systematic error on the π^- measurement. The z values for π^- are offset by 0.02 for clarity.

$\langle x \rangle$	$\langle Q^2 \rangle$ (GeV^2)	$\mathcal{A}^{\phi}$	$\mathcal{A}^{2\phi}$
0.0406	1.38	0.0234 ± 0.0126 ± 0.0038	0.0126 ± 0.0152 ± 0.0042
0.0743	2.14	0.0221 ± 0.0092 ± 0.0022	0.0013 ± 0.0110 ± 0.0021
0.1365	3.62	0.0145 ± 0.0100 ± 0.0021	-0.0145 ± 0.0107 ± 0.0019
0.2575	6.35	0.0590 ± 0.0238 ± 0.0060	0.0281 ± 0.0254 ± 0.0032

Table 5.1: π^+ analyzing powers as a function of x.

$\langle x \rangle$	$\langle Q^2 \rangle$ (GeV^2)	$\mathcal{A}^{\phi}$	$\mathcal{A}^{2\phi}$
0.0403	1.38	0.0058 ± 0.0145 ± 0.0068	0.0205 ± 0.0181 ± 0.0042
0.0739	2.14	-0.0022 ± 0.0109 ± 0.0029	-0.0136 ± 0.0134 ± 0.0018
0.1358	3.64	-0.0015 ± 0.0125 ± 0.0033	-0.0170 ± 0.0138 ± 0.0017
0.2566	6.32	0.0120 ± 0.0312 ± 0.0053	0.0157 ± 0.0338 ± 0.0024

Table 5.2: π^- analyzing powers as a function of x.

$\langle p_\perp \rangle$ (GeV)	$\mathcal{A}^{\phi}$	$\mathcal{A}^{2\phi}$
0.26	0.0052 ± 0.0083 ± 0.0016	-0.0027 ± 0.0089 ± 0.0014
0.53	0.0300 ± 0.0084 ± 0.0027	0.0089 ± 0.0099 ± 0.0027
0.80	0.0518 ± 0.0139 ± 0.0040	0.0057 ± 0.0157 ± 0.0034
1.07	0.0422 ± 0.0247 ± 0.0059	-0.0487 ± 0.0288 ± 0.0060

Table 5.3: π^+ analyzing powers as a function of $p_\perp$.

$\langle p_\perp \rangle$ (GeV)	$\mathcal{A}^{\phi}$	$\mathcal{A}^{2\phi}$
0.26	-0.0038 ± 0.0103 ± 0.0026	-0.0132 ± 0.0113 ± 0.0016
0.53	0.0027 ± 0.0101 ± 0.0025	0.0028 ± 0.0129 ± 0.0016
0.80	-0.0108 ± 0.0166 ± 0.0033	0.0133 ± 0.0194 ± 0.0021
1.07	0.0067 ± 0.0329 ± 0.0098	0.0573 ± 0.0376 ± 0.0057

Table 5.4: π^- analyzing powers as a function of $p_\perp$.

$\langle z \rangle$	$\mathcal{A}^{\phi}$	$\mathcal{A}^{2\phi}$
0.27	0.0158 ± 0.0177 ± 0.0038	0.0110 ± 0.0194 ± 0.0034
0.35	0.0193 ± 0.0126 ± 0.0029	0.0034 ± 0.0149 ± 0.0029
0.47	0.0214 ± 0.0098 ± 0.0021	0.0013 ± 0.0114 ± 0.0020
0.69	0.0273 ± 0.0083 ± 0.0023	-0.0033 ± 0.0092 ± 0.0018

Table 5.5: π^+ analyzing powers as a function of z.

$\langle z \rangle$	$\mathcal{A}^{\phi}$	$\mathcal{A}^{2\phi}$
0.26	0.0163 ± 0.0190 ± 0.0072	0.0226 ± 0.0219 ± 0.0045
0.35	-0.0130 ± 0.0145 ± 0.0039	0.0093 ± 0.0176 ± 0.0021
0.47	0.0112 ± 0.0121 ± 0.0028	-0.0074 ± 0.0145 ± 0.0014
0.68	-0.0061 ± 0.0103 ± 0.0024	-0.0132 ± 0.0120 ± 0.0013

Table 5.6: π^- analyzing powers as a function of z.

5.3 Summary

Analyzing powers of pion electroproduction were measured for the first time between $0.023 < x < 0.4$ and $p_\perp < 1.3$ GeV. A positive $\sin\phi$ analyzing power for π^+ production was observed that was found to increase with $p_\perp$. The signs and relative magnitudes of the π^+ and π^- analyzing powers are in agreement with a simple model of T-odd fragmentation. The observation of the analyzing power strongly suggests the existence of at least one chiral odd distribution function and supports the existence of T-odd fragmentation measured by the DELPHI experiment. There is an indication of a positive analyzing power in the proton and/or K^+ production channels.

Part III

The Aerogel Radiator of the HERMES RICH

Chapter 6 Overview of the HERMES RICH

6.1 Physics Motivation

Before the 1998 data taking period, the HERMES experiment had only limited particle identification capabilites. As described in Section 3.4.3, pions could be identified in the momentum range of approximately 4 to 14 GeV. Time-of-flight techniques could additionally be used for particle momenta near 1 GeV. Full identification of pions, kaons, and protons throughout the entire momentum range of 1–20 GeV, however, was impossible.

The threshold Čerenkov counter was originally designed with the possibility of a future upgrade in mind, and this upgrade was made possible with the recent availability of low density, highly transparent aerogels. The threshold counter was replaced in 1998 with a dual radiator ring–imaging Čerenkov (RICH) counter having the capability of full particle identification.

The HERMES semi–inclusive physics program will benefit greatly with its enhanced particle identification capabilities. Some of the major benefits include more sensitive measurements of the flavor decomposition of nucleon spin structure, polarization transfer in Λ production, and open charm production.

The flavor decomposition of nucleon spin structure was outlined in Section 1.4. This analysis was carried out on the 1996-1997 proton data to extract the valence contributions $\Delta u_v/u_v$ and $\Delta d_v/d_v$ and the sea contribution $\Delta q_{sea}/q_{sea}$ using only electron/hadron separation. The RICH counter would allow the first measurement of polarized electroproduction of kaons which would be sensitive to $\Delta s/s$.

The RICH will also provide clean identification of Λ's. Before 1998, the impossibility of distinguishing pions from protons below the pion threshold of 4 GeV gave

rise to poor signal to noise ratios for low momentum Λ's due to the abundance of low energy pions producing a large combinatorial background. [50] The improvement in the signal to noise ratio with the RICH will allow HERMES to detect longitudinal and transverse Λ polarization with greater statistical significance.

Combinatorical backgrounds have also hindered efforts to detect the open charm decay channels $D^0 \to K^-\pi^+$ and $\overline{D^0} \to K^+\pi^-$. [51] Without kaon identification, the detection of these processes suffers from large backgrounds from pions. The RICH is part of a larger charm detection upgrade program which will enhance the capability of HERMES to measure both open charm and J/ψ production, with the eventual goal of extracting $\Delta G/G$.

6.2 Time Constraint

The HERMES experiment embarked on a very ambitious schedule to perform the RICH upgrade. The RICH proposal [52] was approved in early 1997, and the window of opportunity to install the RICH, dependent on the HERA shutdown schedule, was in the spring of 1998. The next opportunity would not come until the year 2000. The strict timeline denied HERMES the possiblity to explore certain avenues in the development of the RICH, and those involving the aerogel radiator will be mentioned in the following when appropriate.

6.3 Aerogel in the HERMES RICH

The difficulty with a RICH detector in the HERMES experiment is primarily the momentum coverage required. To achieve separation of pions, kaons, and protons between 2–9 GeV, a radiator with a moderate refractive index of approximately 1.03 is required. This index is not found in atmospheric pressure gases or liquids, leaving aerogel as the only available option.

6.3.1 Aerogel Properties

Aerogel consists of clusters of silica particles arranged in a highly porous, three-dimensional netlike structure. One of the most important properties of aerogel which determines its usefulness as a RICH radiator is the size of its structural features at nanometer length scales. The particle size is of the order of a few nanometers while the pore size is on the order of tens of nanometers. These length scales are much smaller than the wavelength of visible and ultraviolet Čerenkov radiation. The refractive index is therefore much lower than that of fully dense silica and it increases linearly with the density of the aerogel.

The absorption length of aerogels is much longer than the scattering length and for most purposes can be neglected. Rayleigh scattering is the dominant scattering mechanism, and its cross section depends strongly on the size of the scattering centers. Rayleigh scattering is nearly isotropic, causing the Čerenkov radiation to be scattered diffusely throughout the material. This does not prevent its usefulness as a threshold detector because the scattered radiation can be effectively collected and detected due to the large absorption length of the material. But until recently, the scattering length of aerogels has been too short for RICH detectors, reducing the unscattered photon yield to levels too low to be practically measurable.

6.3.2 Aerogel Production

Recent advances [53] in aerogel production techniques have reduced the average size of the silica particles, thereby decreasing the Rayleigh scattering cross section and providing a more transparent material.

The conventional aerogel production technique [54] uses a single step with an acid catalyst. Tetraalkoxysilane and water are mixed in an excess of alcohol solvent, and the following hydrolysis and condensation take place.

$$\begin{aligned} m\mathrm{Si(OR)_4} + 4m\mathrm{H_2O} &\rightarrow m\mathrm{Si(OH)_4} + 4m\mathrm{ROH} \\ m\mathrm{Si(OH)_4} &\rightarrow (\mathrm{SiO_2})_m + 2m\mathrm{H_2O} \end{aligned}$$

The solution becomes colloidal and through an aging processes, a three dimensional network of SiO_2 clusters with siloxane linkages is formed. The resulting alcogel is dried in an autoclave above the critical point to remove the alcohol. The density is controlled with the amount of alcohol solvent used in the initial alcogel formation. This technique cannot be used to produce low density aerogels because adding more solvent to reduce the density promotes the backward reactions taking place.

To produce aerogels with lower refractive index, a two step method [55] is employed. The first step consists of producing a partially hydrolysed and partially condensed silica oil. The alcohol is distilled off from the silica oil and the resulting solution is mixed with a non-alcohol solvent. Polymerization proceeds using a base rather than an acid catalyst, which results in smaller pore sizes. The aged and supercritically dried aerogels are more transparent and can be produced with lower density than the single step method.

The technique used to produce the HERMES aerogel is a simplified version of the two step method with the additional feature that the resulting aerogels are highly hydrophobic, unlike conventional aerogels. The hydrophobicity is achieved by placing the alcogel in a solution of alcohol and a hydrophobic agent such as hexamethyldisilazane, replacing hydrophilic OH groups with $OSi(CH_3)_3$. Furthermore, the alcohol is replaced by carbon dioxide before supercritical drying. The pressure and temperature at the carbon dioxide critical point are lower than alcohol, making the supercritical drying process safer and more economical.

6.3.3 Feasibility Studies

The feasibility of using modern aerogels in RICH detectors has been experimentally demonstrated [56]. In particular, the technique of detecting aerogel Čerenkov rings with photomultipliers has been developed, with results that agreed with expectations for the Rayleigh scattered and unscattered photoelectron yields [57]. Beam tests with the new aerogels will be discussed in Section 8.1.1.

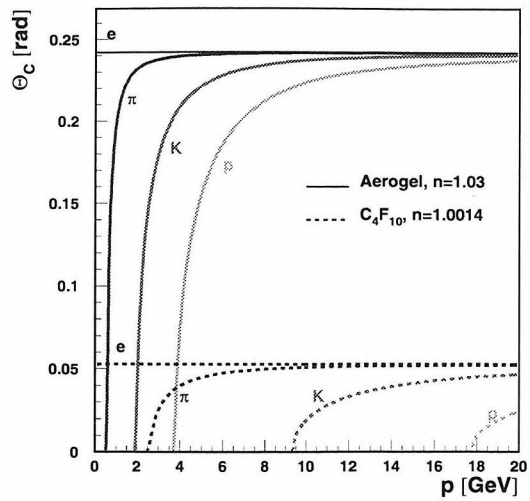

Figure 6.1: Čerenkov angles for aerogel and C_4F_{10}.

6.4 HERMES RICH Design

In the HERMES experiment, two radiators are needed to span the entire momentum range because the aerogel rings for different particles become difficult to distinguish above about 10 GeV. Therefore atmospheric pressure C_4F_{10} gas ($n = 1.0014$) is used to complement the aerogel, providing particle separation in the high momentum range. The Čerenkov angles of electrons, pions, kaons, and protons for aerogel and C_4F_{10} gas are shown in Figure 6.1.

The layout of one half of the RICH is shown in Figure 6.2. It uses the same housing as the previous threshold counter but introduces the aerogel radiator at the entrance and uses a new mirror system and photon detector. The aerogel radiator will be described in detail in the following chapter. The RICH housing is 1.26 m long and made of aluminum, with a total volume of about 4000 liters. The entrance and exit windows are each made of foils of 100 μm mylar and 30 μm tedlar.

The spherical mirror has a radius of curvature of 2.2 m and consists of 8 individually aligned segments with a total area of 250 $\times$ 80 cm. It is made of a thin aluminum reflective layer on a 3 mm carbon fiber backing.

Each photon detector, shown schematically in Figure 6.3, consists of 1934 hexag-

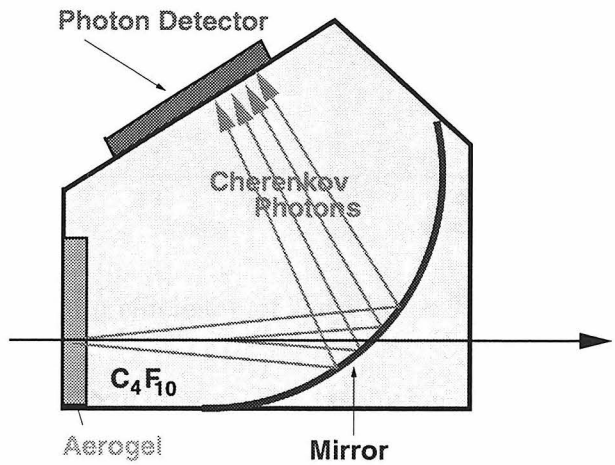

Figure 6.2: Schematic diagram of the HERMES RICH.

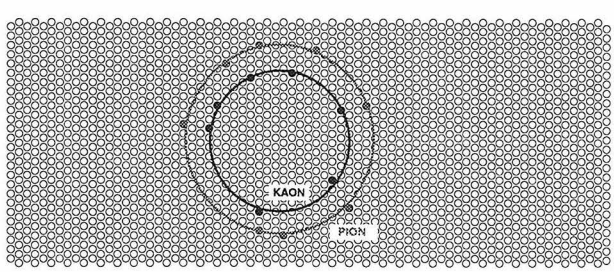

Figure 6.3: Schematic diagram of the RICH photomultiplier matrix.

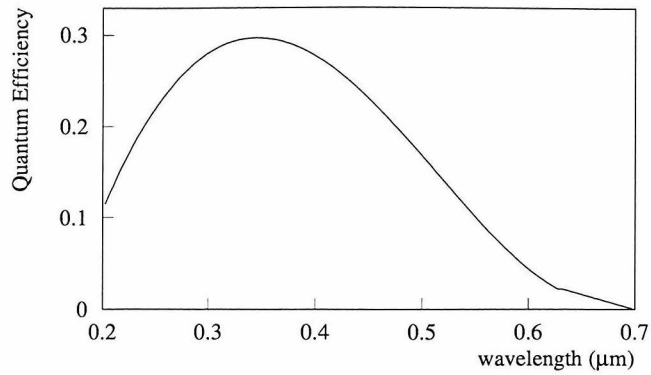

Figure 6.4: Quantum efficiency of the Philips XP1911 photomultipliers.

onally packed 3/4" photomultipliers. The resolution of the Čerenkov rings is largely determined by the granularity of the photon detector, and the granularity was chosen to resolve the aerogel ring size at roughly the 1% level. The gas rings are detected with low resolution. Philips XP1911-UV/A photomultipliers were chosen for their high quantum efficiency in the ultraviolet and visible regions, shown in Figure 6.4. The gas photons that reach the photon detector are mostly in the ultraviolet region while the aerogel photons are in the visible. To maximize the coverage of the photon detector, light collecting cones were installed in front of the photomultipliers. The cones increase the geometric coverage from 38% to 81%. The cones are fitted with aluminized mylar foil with 90% reflectivity down to 200 nm. The RICH photomultipliers are read out digitally, recording only the identities of the photomultipliers that produce signals above a certain threshold.

6.5 Aerogel Ring Resolution Goal

Above the kaon gas threshold of about 9.3 GeV, the gas radiator provides clean separation of all three hadrons. Between 3 and 9.3 GeV the gas identifies pions. Below 3 GeV, only crude aerogel ring resolution is required to identify pions, kaons, and protons. The only uncertainty in the RICH performance is proton/kaon separation between 3 and 9.3 GeV which must be provided by the aerogel radiator. Good aerogel

n_σ	contamination
2	.11
2.5	.03
3	.005

Table 6.1: PID contaminations for a 95% cut efficiency assuming equal fluxes of each particle.

ring resolution is therefore most critical at 9.3 GeV.

The ring separations are calculated using (for example)

$$n_\sigma^{p/K} = \frac{|\theta_p - \theta_K|}{\sqrt{d\theta_p^2 + d\theta_K^2}},$$

where θ_p is the proton Čerenkov angle, $d\theta_p$ is the angular width of the proton ring, and $n_\sigma^{p/K}$ is the number of standard deviations separating the proton and kaon rings. In order to achieve 3σ proton/kaon ring separation at 9.3 GeV, the aerogel ring resolution must be

$$\left(\frac{d\theta}{\theta}\right)_{\text{goal}} \leq 1.4\%.$$

PID contaminations for a 95% cut efficiency assuming equal fluxes of protons and kaons are shown in Table 6.1 as a function of ring separation. The ring separation assuming a 1.4% ring resolution, calculated according to formulas describing Čerenkov radiation to be presented in the following chapter, is plotted in Figure 6.5.

Several factors contribute to the overall aerogel ring resolution, including the pixel size of the phototube array, the photon collection efficiency, chromatic aberrations due to optical dispersion in aerogel, and aerogel density variations on several length scales. These effects are discussed in the following chapters with pertinent measurements to aid in estimating the contribution of each to the overall resolution.

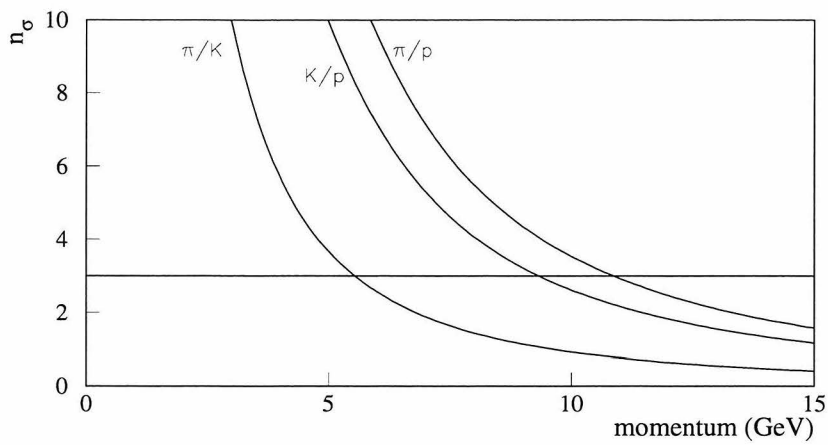

Figure 6.5: Aerogel ring separation as a function of momentum assuming a 1.4% ring resolution.

Chapter 7 The Aerogel Radiator

The aerogel radiator design is influenced by many considerations, some related fundamentally to the optical characteristics of aerogel and others more practical in nature. The expected photoelectron yields for Rayleigh scattered and unscattered radiation depend on the scattering properties of aerogel and determine the optimal radiator thickness. The wavelength dependence of the scattered and unscattered yields and the refractive index constrains the choices for the radiator exit window. The aerogel was manufactured in the form of small tiles, the shape and size of which also influenced the radiator design. Each of these subjects will be discussed before describing the aerogel radiator at the end of this chapter.

7.1 Čerenkov Radiation

The yield of Čerenkov radiation for a particle of unit charge and velocity β traversing a medium of refractive index n is

$$\frac{d^2N}{dzd\lambda} = \frac{2\pi\alpha}{\lambda^2}\left(1 - \frac{1}{\beta^2 n^2(\lambda)}\right), \tag{7.1}$$

where N is the number of photons, λ is the photon wavelength, and z is the distance traveled in the material. [58]

Čerenkov radiation is emitted at the Čerenkov angle θ with respect to the particle's trajectory, calculated as

$$\cos\theta = \frac{1}{\beta n}.$$

From this equation, the important relationship between refractive index variations and the resolution of the Čerenkov angle can be derived in the relativistic limit of

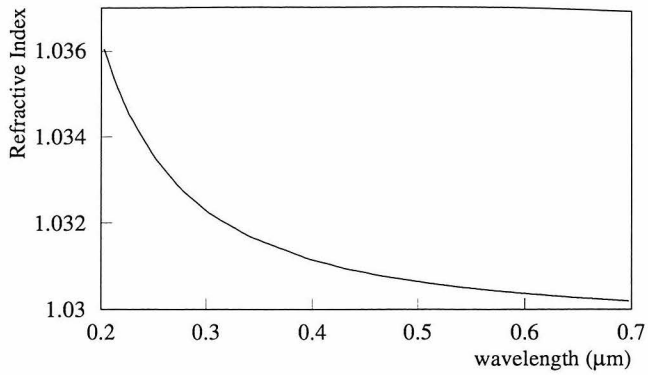

Figure 7.1: Dispersion relation of aerogel as predicted by Equation 7.3.

$\beta = 1$:

$$\frac{d\theta}{\theta} = \frac{1}{2}\frac{dn}{\tilde{n}}. \tag{7.2}$$

The notation $\tilde{n} \equiv n - 1$ will be used frequently in this thesis.

7.2 Optical Dispersion in Aerogel

Equation 7.1 shows that the photoelectron yield is influenced weakly by optical dispersion. Optical dispersion also plays a more important role through its impact on the resolution of the Čerenkov rings.

Optical dispersion in aerogel can be modeled approximately [59] by averaging the refractive indices of fully dense silica and air:

$$n^{\text{aerogel}}(\lambda) = A \cdot n^{\text{air}}(\lambda) + B \cdot n^{\text{SiO}_2}(\lambda). \tag{7.3}$$

Using the well known dispersion relations of air and fused silica [60], the constants A and B can be determined by a measurement of n^{aerogel} at a single wavelength, fixing the λ-dependence of n^{aerogel}. Figure 7.1 shows the refractive index of aerogel as predicted by Equation 7.3 assuming $n = 1.0303$ at a wavelength of 633 nm. This model predicts a rapid change in the refractive index of aerogel in the ultraviolet region. It is clear

from Figure 7.1 and Equation 7.2 that such a large change in refractive index at the low wavelengths can have an impact on the resolution of well over 1%. Measurements of optical dispersion will be presented in the following chapter.

7.3 Scattering Properties of Aerogel

7.3.1 Rayleigh–Debye Scattering in Inhomogeneous Media

Light scattering in inhomogeneous materials results from fluctuations in the dielectric constant. The scattering is described by Rayleigh-Debye theory. For unpolarized light, the scattered intensity at scattering angle Θ is [61]

$$I(\Theta) = I_o \frac{\pi^2 V \overline{\eta^2}}{\lambda^4 r^2}(1 + \cos^2\Theta)w, \tag{7.4}$$

where I_o is the incident intensity, $\overline{\eta}$ is the rms variation of the dielectric constant, V is the illuminated volume of the material, λ is the wavelength, and r is the distance from the material to the detector. The correlation volume w is given by

$$w = \int_0^\infty 4\pi s^2 \gamma(s) \frac{\sin qs}{qs} ds,$$

where $\gamma(s)$ is the correlation function and $q = (4\pi/\lambda)\sin(\Theta/2)$ is the momentum transfer. The correlation function describes index fluctuations η at points a and b separated by a distance s:

$$\overline{\eta^2}\gamma(s) = \eta_a \eta_b$$

7.3.2 Random Two Phase Medium Model

Aerogel can be modeled as a random matrix of glass and air. It can be shown that for a two phase random medium, the correlation function has the form [61]

$$\gamma(s) = \exp\left(-\frac{s}{a_c}\right),$$

where a_c is the correlation length, a parameter that reflects the distance scale of fluctuations in the dielectric constant. With this correlation function, the correlation volume becomes

$$w = \frac{8\pi a_c^3}{(1 + a_c^2 q^2)^2}.$$

For the case $a_c \ll \lambda$, w becomes independent of angle so that the scattering is symmetric about $\pi/2$ and proportional to λ^{-4}. This is the long wavelength Rayleigh scattering approximation. If on the other hand a_c is comparable to or greater than λ, the scattering becomes forward peaked and nearly independent of λ.

The scattering length due to Rayleigh-Debye scattering is calculated by integrating Equation 7.4 and is given by [61, 62]

$$\begin{aligned} \frac{1}{L_{\text{scat}}} &= 2k^4\overline{\eta^2}a_c^3\left[\frac{(b+2)^2}{b^2(b+1)} - \frac{2(b+2)}{b^3}\log(b+1)\right], \\ b &= 4k^2a_c^2, \end{aligned}$$

where $k = 2\pi/\lambda$.

7.3.3 Long Wavelength Limit and Hunt Parameters

The correlation length a_c in aerogel is related to the nanometer scale silica cluster and pore sizes. Since the wavelengths of interest are in the visible and ultraviolet range, the approximation $a_c \ll \lambda$ is valid. In this case the scattering length becomes [62]

$$\begin{aligned} \frac{1}{L_{\text{scat}}} &= \frac{64}{3}\pi^4\overline{\eta^2}a_c^3\lambda^{-4} \\ &\equiv C\lambda^{-4} \end{aligned}$$

where C, called a Hunt parameter, characterizes the amount of isotropic Rayleigh scattering.

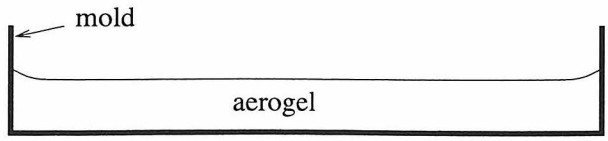

Figure 7.2: Illustration of the effects of capillary forces acting on aerogel during its manufacture on the final aerogel tile shape.

The transmission through an aerogel sample of length L is thus given by

$$T = A \exp\left(-\frac{CL}{\lambda^4}\right) \tag{7.5}$$

where A is an additional Hunt parameter that accounts for absorption effects which are assumed to be independent of wavelength. Highly transparent aerogels have $A \approx 1$ and small values of C.

Transmission measurements on HERMES aerogel presented in the next chapter show very good agreement with Equation 7.5 with $A \sim 0.96$ and $C \sim 0.01$ $\mu\text{m}^4\text{cm}^{-1}$. The earlier generations of aerogel had transparencies of at best $C \sim 0.02$ $\mu\text{m}^4\text{cm}^{-1}$.

7.4 Tile Properties

The aerogel was manufactured by Matsushita Electric Works (located in Osaka, Japan) in the form of tiles of dimensions $114 \times 114 \times 11.3$ mm^3, the only size commercially available. For reasons to be discussed below, larger tile sizes would have been more desirable. The gellation of aerogel is a process that is very sensitive to environmental conditions, and it is not straightforward to "double the recipe" to produce larger tiles without losing transparency.

Furthermore, the tiles are not perfectly flat. Through a kind of meniscus interaction of the pre-solidified aerogel with its mold, the tiles become thicker on average near the edges than the center. This is illustrated in Figure 7.2. The thickness dimension reported above represents the edge thickness. The tile thickness variations were measured mechanically [63] using a SurfTester (Mitutoyo Co.) with a resolution of 0.05 μm. The edges of the tiles were found to be nearly 2 mm thicker than the

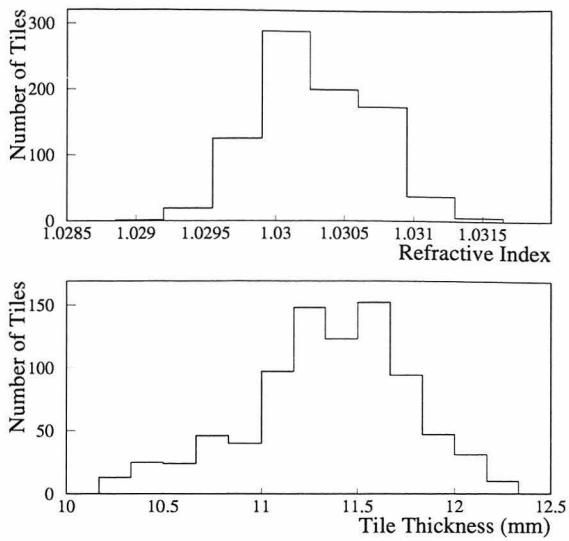

Figure 7.3: Distributions of refractive indices and thicknesses of the tiles installed in the HERMES RICH.

centers. The increase in thickness is confined to mostly within 5 mm of the edge, and the remaining area of the tile is relatively flat with an average thickness of about 9.3 mm.

The distributions of the refractive indices and thicknesses of the tiles installed in the HERMES RICH are shown in Figure 7.3. The refractive indices were measured using the laser deflection technique described in the following chapter.

7.5 Aerogel Radiator Design

A schematic view of the HERMES RICH with a cutaway view of the aerogel radiator is shown in Figure 7.4. The container consists of an aluminum frame with a 1 mm aluminum entrance window and a 3.2 mm lucite exit window. While there is no reason to believe that the aerogel will be damaged by the C_4F_{10} environment of the RICH, there is no direct evidence to the contrary. The aerogel is isolated by making the container air tight and circulating dry nitrogen at a slow rate. The aerogel tiles are stacked 5 tiles longitudinally, 5 rows vertically, and 17 columns horizontally as required to span the spectrometer acceptance. Black plastic spacers of various

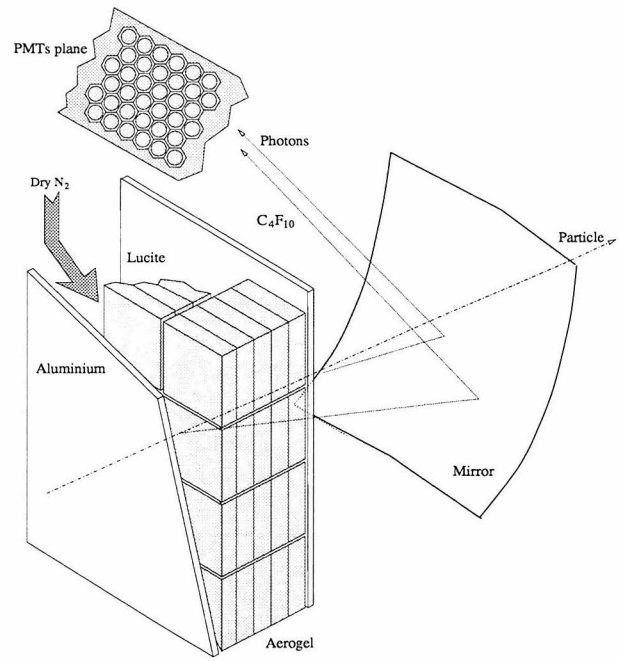

Figure 7.4: Schematic view of the HERMES RICH with aerogel radiator.

thicknesses were inserted between the aluminum frame and the aerogel tiles to prevent the tiles from shifting while the radiator is moved.

7.5.1 Photoelectron Yield

The photoelectron yields of Rayleigh-scattered and unscattered aerogel radiation can be calculated using Equations 7.1, 7.3, and 7.5 and the measured optical properties of elements of the HERMES RICH. These include the XP1911 quantum efficiency shown in Figure 6.4, the transmissions of the lucite exit window and glass windows of the photon detector, and the reflectivity of the spherical mirror. The results are shown in Figure 7.5 as a function of wavelength and the distance of the emission point from the radiator exit window.

7.5.2 Choice of Radiator Thickness

The bottom of Figure 7.5 displays the distributions of Rayleigh-scattered and unscattered light in the distance from the emission point to the exit window. As this distance increases, the likelihood that the Čerenkov light will escape unscattered de-

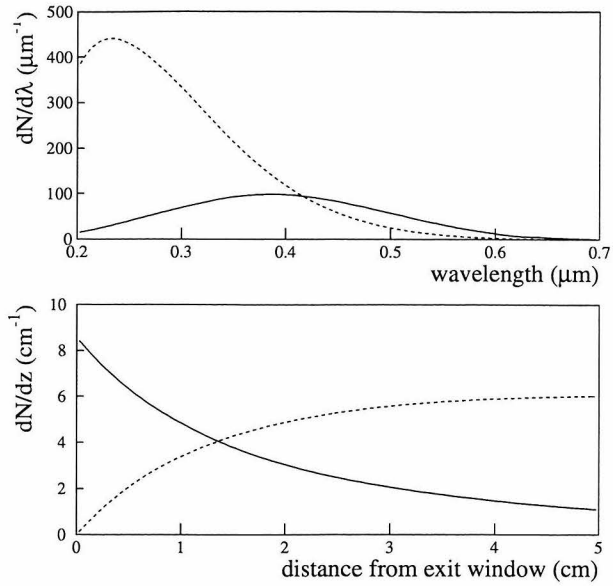

Figure 7.5: Top: Rayleigh-scattered (dashed) and unscattered (solid) light yields as a function of wavelength multiplied by the XP1911 quantum efficiency. Bottom: Light yields as a function of the distance into the aerogel radiator from the exit window multiplied by the quantum efficiency, lucite and glass transmissions, and mirror reflectivity.

creases. The 5 cm radiator thickness was chosen as the optimal point beyond which the unscattered light yield would only increase slightly while the backgrounds would increase noticeably.

7.5.3 Choice of Exit Window Material

The choice of exit window was driven principally by its transmission properties. The top of Figure 7.5 shows the wavelength distribution of aerogel-generated photons multiplied by the XP1911 quantum efficiency. The distribution of Rayleigh-scattered light is centered at smaller wavelengths than unscattered light due to the λ^{-4} dependence of the scattering length. The Rayleigh-scattered light is produced isotropically and produces a fairly uniform background over the photon detector. The low wavelength range is also a problem due to optical dispersion. Thus the exit window material must transmit as much unscattered radiation as possible while suppressing the backgrounds and optical dispersion in the low wavelength range.

Most readily available materials including most glasses and plastics absorb strong-

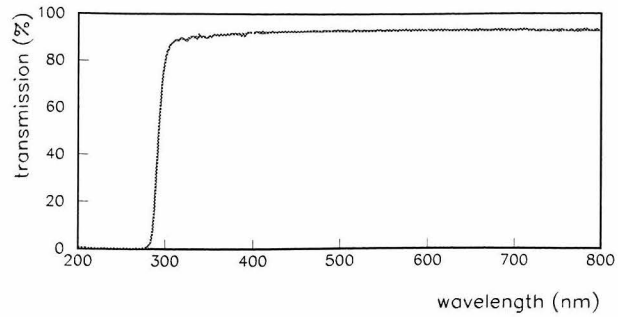

Figure 7.6: Transmission spectrum of the 3.2 mm ultraviolet-transmitting lucite radiator exit window.

ly below about 400 nm. This amount of absorption would be unacceptable in the HERMES RICH, losing about 50% of the signal. Fortunately, an ultraviolet-transmitting lucite (UVT) is commercially available with an absorption cutoff at approximately 290 nm. Its transmission spectrum is shown in Figure 7.6.

Unfortunately, UVT is a Čerenkov radiator with $n = 1.5$ which will produce background photons. The total Čerenkov light yield of 3.2 mm UVT lucite is roughly half the total Čerenkov yield of 5 cm aerogel for a relativistic particle.

The refractive index of UVT is sufficiently high that the Čerenkov angle is greater than the total internal reflection angle for a UVT-air interface, so that for particles normally incident on the UVT, none of the Čerenkov light produced in the UVT will escape. However, for particles that strike the UVT surface at non-normal incidence, some light produced in the UVT may strike the surface at an angle smaller than the total internal reflection angle and may therefore be transmitted. The average transmission of Čerenkov photons generated in lucite is shown in Figure 7.7a as a function of the track angle.

Fortunately, the transmitted photons are deflected away from the RICH mirrors due to the change in refractive index as they traverse the UVT-air interface. The average exit angle of the photons as a function of the incident track angle is shown in Figure 7.7b. Transmitted photons do not enter the mirror acceptance for track angles less than approximately 200 mrad.

The distribution of track angles behind the HERMES spectrometer magnet is shown in Figure 7.8. Most of the tracks lie between 50 and 300 mrad, with few above

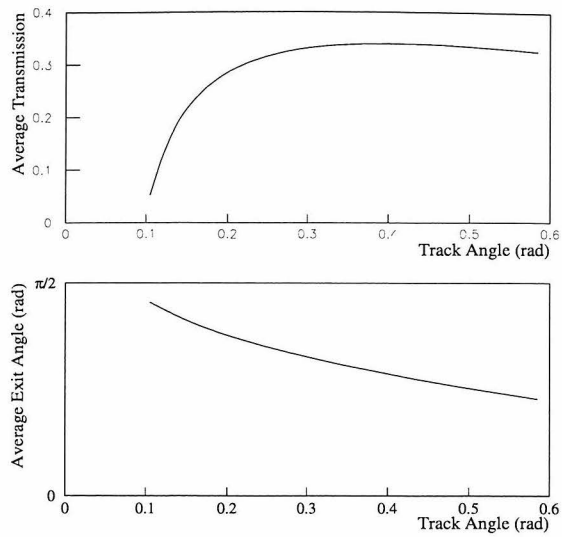

Figure 7.7: (a) Transmission and (b) exit angle of UVT-generated Čerenkov light calculated by Monte Carlo methods.

400 mrad. Using the observed distribution of particle momenta and trajectories in the HERMES experiment and a simple box acceptance to model the RICH mirror, the average photoelectron yield per track arising from non-Rayleigh scattered aerogel light, Rayleigh scattered aerogel light, and UVT light was calculated using Monte Carlo techniques. Similar calculations were performed for other choices of exit window, including no exit window at all and 3.2 mm standard ultraviolet absorbing lucite (UVA). The average photoelectron yields are shown in Figure 7.9. The UVT is seen to reduce the Rayleigh scattered aerogel yield by more than a factor of 2 while transmitting most of the non-Rayleigh scattered light. The UVA dramatically reduces the Rayleigh scattered light, but absorbs an unacceptable fraction of unscattered aerogel light, as do materials with similar absorption properties such as glass and mylar.

7.5.4 Choice of Exit Window Thickness

While a thinner exit window presents less material in the spectrometer and produces fewer background photons, a minimum thickness is required for reasons of mechanical stability. The window must be able to support the weight of the aerogel tiles to prevent

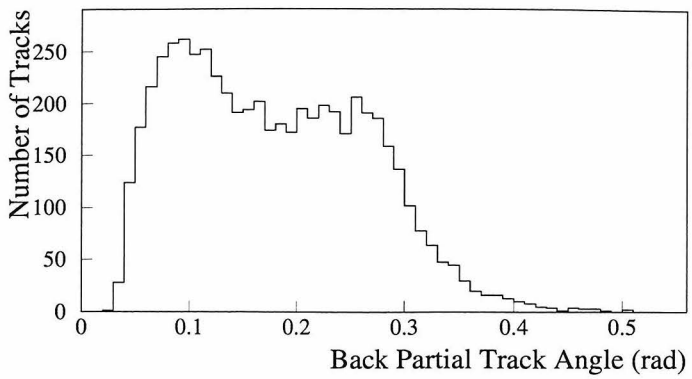

Figure 7.8: Back partial track angles in the HERMES spectrometer.

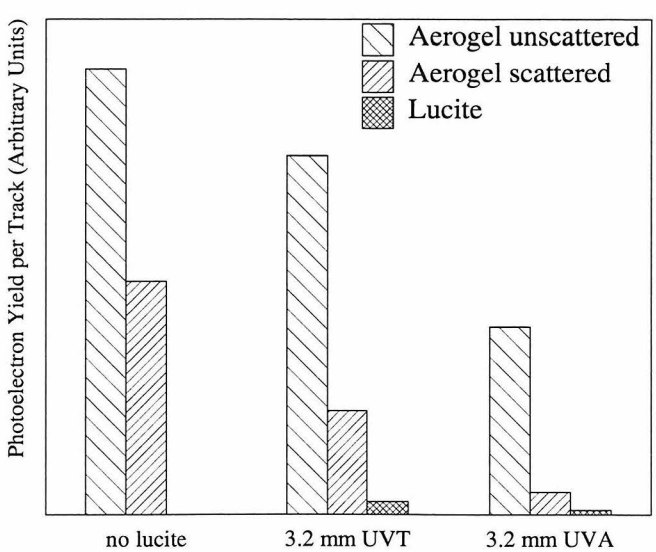

Figure 7.9: Comparison of average photoelectron yields for a variety of exit windows.

them from slipping out of place. It must also be able to withstand the pressures of having holes drilled and being clamped in place without developing cracks.

A further consideration is the pressure differences between the radiator and the external C_4F_{10} environment. The nitrogen pressure inside the radiator is very nearly atmospheric since the outlet is vented directly to the atmosphere. The C_4F_{10} gas, on the other hand, is a closed system which is regulated to be typically within 0.2 torr of atmospheric pressure. The size of the exit window is so large that even small pressure differences can cause deflections large enough for the window to come into contact with the aerogel and squeeze the tiles. The exit window is thick enough that it is not expected to contact the aerogel tiles at overpressures of 0.2 torr. Aerogel tile stacks can withstand pressures up to 2 torr without visible signs of damage.

7.5.5 Use of Tedlar

The shape and size of the tiles have two undesirable and practically unavoidable consequences. The thickness variations, described in Section 7.4, cause deflections of light rays passing near the edges of the tiles simply as a consequence of Snell's Law. Based on the thickness measurements described in Section 7.4, light rays are expected to be deflected by several mrad when traversing aerogel tiles within a few mm of their edges. Measurements of the deflection will be presented in the next chapter.

The tile edges are a source of a second problem, namely the internal reflection of light rays striking side boundaries. This process is illustrated in Figure 7.10. The Čerenkov angle and the total internal reflection angle are nearly complementary, so that for tracks normally incident on the aerogel tile, the non-Rayleigh scattered Čerenkov photons will strike the side of the tile at nearly the total internal reflection angle. Light that is reflected at the side surface of an aerogel tile will appear to have originated from an imaginary track which is the mirror reflection of the actual track, where the mirror is formed by the plane containing the side of the tile. At the image plane, some of the photons will land at positions on the mirror image Čerenkov cone, giving rise to severe distortions.

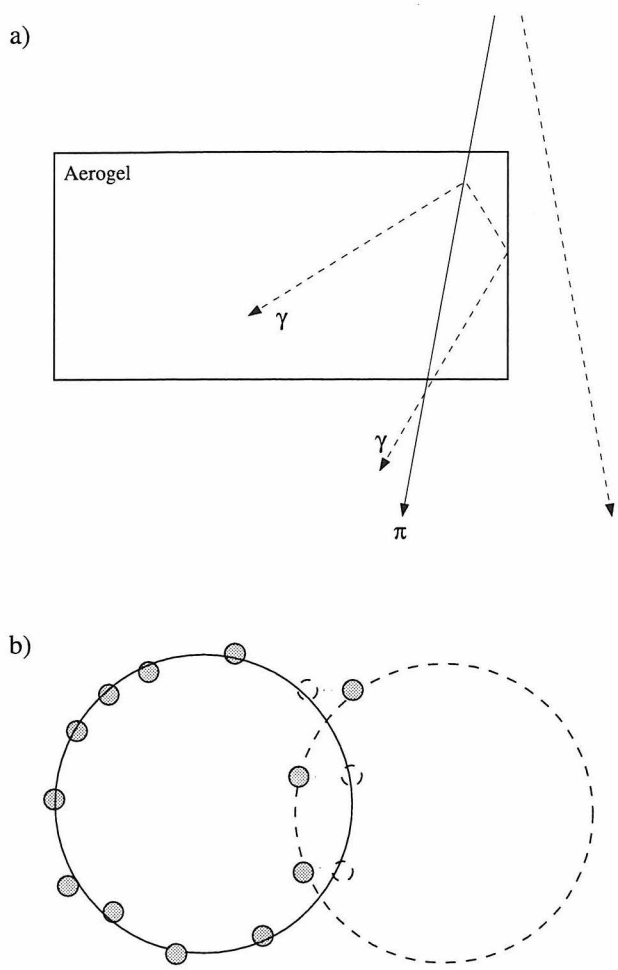

Figure 7.10: Illustration of total internal reflection at aerogel tile boundaries.

In reality, the quality of the surfaces of the tile sides is so poor that the idealized picture of Figure 7.10 is not accurate. Photons that are either transmitted or reflected through a tile boundary are often deflected in unpredictable directions. Unfortunately, these photons are likely to land in the vicinity of the Čerenkov ring and will give rise to a background which could be much more damaging to the resolution than the semi-random background of Rayleigh scattering.

Several solutions to these edge problems were considered. One was to machine the tiles, cutting off about 5 mm of material on each side. Since the thickness variations were largely confined to the edge regions of the tiles, these problems could be reduced dramatically. A second was to coat the sides with black paint. This idea was tested and the results showed that internal reflections could be partially reduced. These solutions were unrealistic given the time constraints and the amount of handling of the tiles required. Internal reflections are also reduced by squeezing the tiles together so as to eliminate the air gaps between them, but this requires more pressure than could be realistically achieved without risking severe damage to the tiles.

Finally, it was decided to place opaque black sheets of tedlar between the aerogel tile stacks. While this does not noticeably affect the amount of internal reflection, it does reduce distortions from light crossing stack boundaries.

7.5.6 Arrangement of Tiles

The locations chosen for the tiles in the radiator took into consideration the refractive indices, the thicknesses, and the surface quality of the tiles simultaneously.

In order to achieve the best ring resolution, it is important to place tiles with similar refractive index together in the same stack so that particles passing through the radiator emit photons with very similar Čerenkov angles. It is less important to have the same refractive index in different stacks because it is possible to use the rings of relativistic electrons to calibrate the detector for the refractive index in each stack. In other words, refractive index variations in the longitudinal direction give rise to unavoidable spreading of the rings while refractive index variations in the transverse

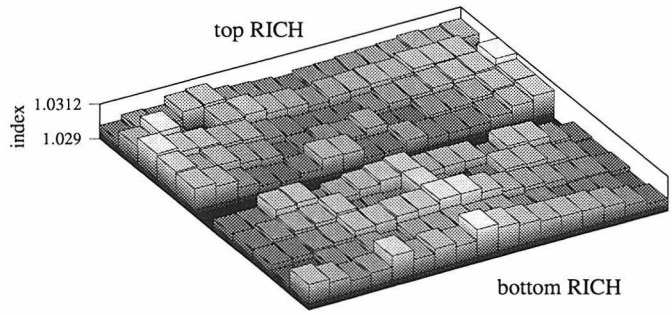

Figure 7.11: Average refractive indices of tile stacks.

298	301	301	305	306	302	300	300	298	300	301	302	302	303	304	303	304
304	310	296	293	305	306	303	303	301	303	303	304	304	306	306	307	297
309	306	306	304	303	300	299	297	297	297	299	302	302	304	306	307	311
308	303	305	302	301	296	299	300	299	303	297	297	300	300	303	305	308
307	305	300	298	296	298	304	303	297	298	301	299	298	298	301	305	307

298	298	306	307	299	302	305	306	308	304	304	304	299	306	305	301	297
298	301	302	304	307	299	299	298	308	300	297	299	305	304	301	299	296
298	299	300	301	305	306	307	308	310	310	307	304	303	302	299	299	298
295	296	299	300	302	299	303	303	304	302	302	299	301	298	298	298	295
306	303	300	302	309	303	306	304	311	308	306	305	304	304	303	300	297

Table 7.1: Average refractive indices $\tilde{n} \cdot 10^4$ of tile stacks. The top and bottom halves of the table correspond the the top and bottom halves of the RICH, respectively.

direction can be calibrated away. The average refractive indices in each stack are plotted in Figure 7.11 and tabulated in Table 7.1. On average, the top half of the RICH has a lower refractive index than the bottom half in the region of high particle fluxes near the beam axis.

The tile thicknesses vary considerably from tile to tile, as shown in Figure 7.3. If the tiles are not chosen carefully, large variations in the stack thicknesses can result. In order to avoid the possibility of tiles falling out of their stacks due to lack of support from surrounding stacks, the tiles were placed in stacks in a way that minimized the stack thickness variations.

The tiles were classified qualitatively in terms of the quality of their edges, paying attention to large chips or cracks that could deflect light rays in unpredictable ways.

The tiles with the best quality were placed in the region of the radiator nearest the beam that experiences the largest particle fluxes and in the layers nearest the exit window.

Finally, each tile was placed with its flat face (as opposed to its concave face, see Figure 7.2) towards the exit window. This is important in modeling the effect of tile thickness variations in Monte Carlo simulations and eliminates the effect of the thickness variations on the resolution for the layer of tiles nearest the exit window.

Chapter 8 Optical Characterization of Aerogel

8.1 Čerenkov Light Yield

The aerogel ring resolution depends on the yield of Čerenkov photons generated by particles traversing the RICH, improving roughly with the square root of the yield. Therefore it is important to determine whether the actual yield agrees with the expectations of Equation 7.1.

8.1.1 Test Beam

Beam tests using aerogels produced by similar methods as the HERMES aerogel were carried out using a 10 GeV pion beam at CERN. [57] The Čerenkov rings were detected with photomultipliers. The yields of unscattered and Rayleigh scattered photons were consistent with Monte Carlo calculations based on the measured transmission properties of the aerogel. The apparatus was not capable of a precision measurement of the Čerenkov angle resolution.

Another test at CERN used a 5 GeV mixed proton and pion beam with an apparatus that contained all the essential features of the HERMES RICH, including Matsushita aerogel and a hexagonally packed array of Philips XP1911 photomultipliers. [64] The aerogel rings were clearly observed, with the number of fired photomultipliers measured to be consistent with expectations. A single photon resolution of approximately $3.6\% \pm 0.5\%$ was observed, giving a ring resolution of 1.2% assuming 9 photoelectrons per ring.

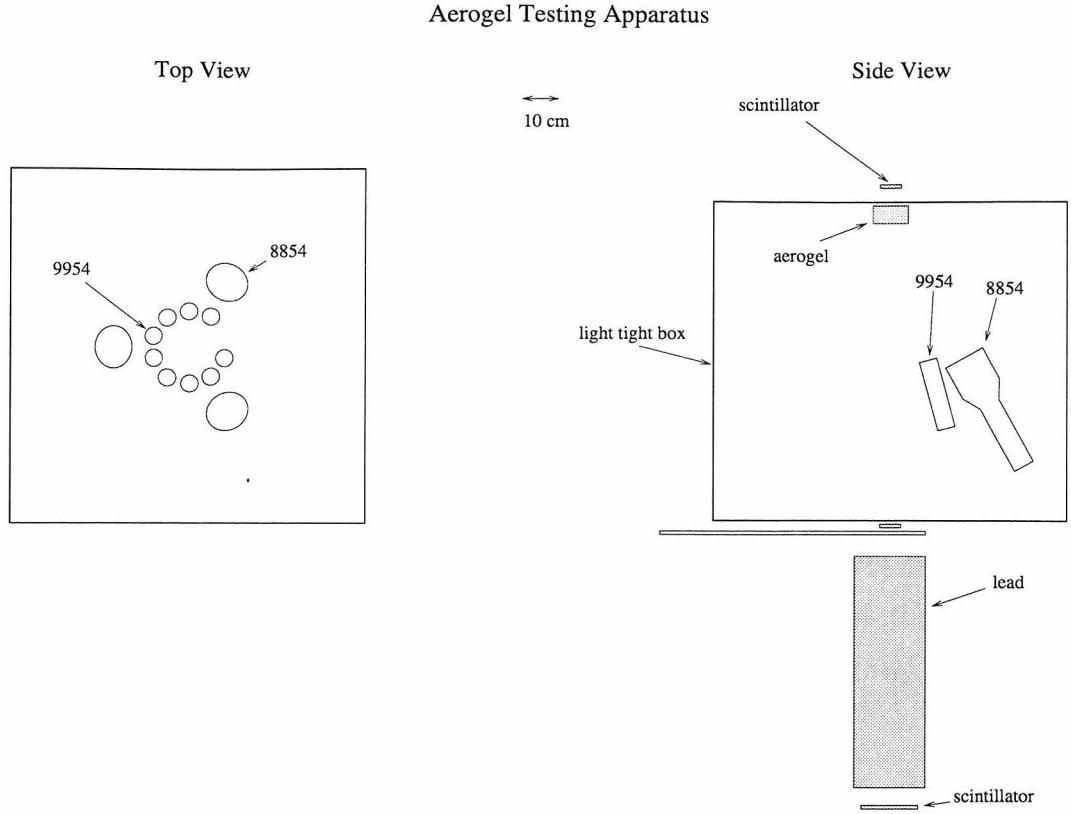

Figure 8.1: Schematic of apparatus for measuring the Čerenkov light yield of cosmic rays passing through aerogel.

8.1.2 Cosmic Ray Tests

The Čerenkov light yield of cosmic ray muons passing through aerogel was measured at Caltech using the apparatus shown in Figure 8.1. Using scintillator paddles, cosmic ray trajectories were constrained to pass through a 5×5 cm^2 area above and below a light tight box. Another scintillator situated below a 1 m thick stack of lead bricks selected muons with energies greater than 1 GeV so that all triggers would originate from highly relativistic particles producing saturated Čerenkov rings. The measured trigger rate was in rough agreement with expectations. [58] The aerogel was held near the roof of the box where it was viewed by a collection of PMTs. Nine 2" Thorn EMI model 9954 PMTs viewed non-Rayleigh scattered Čerenkov light and three 5" RCA model 8854 PMTs viewed Rayleigh scattered Čerenkov light. Measurements of light yield were performed on a combination of 4 aerogel tiles followed by 3 mm ultraviolet-transmitting lucite, the material used as the exit window of the aerogel

	photoelectron yield per PMT per trigger	
	unscattered	scattered
data	0.55 ± 0.03	0.095 ± 0.020
Monte Carlo	0.61 ± 0.03	0.075 ± 0.005

Table 8.1: Comparison of measured light yields with Monte Carlo prediction.

container.

A Monte Carlo program was written to calculate the expected cosmic ray light yield using Equations 7.1 and 7.5 along with the quantum efficiencies of the PMTs supplied by the manufacturers. The transmission properties of UVT, the density fluctuations, surface scattering properties, and dispersion relation of aerogel were modeled using the results of the measurements presented in this thesis. Rayleigh scattered light is assumed to be scattered isotropically and to exit the aerogel after a single scattering.

Table 8.1 summarizes the light yield measurements and compares them to the Monte Carlo prediction. The errors on the Monte Carlo calculations reflect the uncertainty in the Hunt parameters A and C for the aerogel tiles used in the measurement. The widths of the Hunt parameter distributions were taken from the transmission measurements described below. [65] The measured yields are consistent with Monte Carlo expectations. The main usefulness of the result is to demonstrate that the lucite window has no unexpected effect on the photoelectron yields.

8.2 Transmission, Absorption, Reflection

Transmission spectra for 200 aerogel tiles were measured [65] between 200 and 900 nm using a double beam UV-vis spectrophotometer. The best and worst case spectra are shown in Figure 8.2. The spectra are well (but not perfectly) described by the Rayleigh scattering law, Equation 7.5. The Hunt parameters were measured to be

$$\begin{aligned} A &= 0.964 \\ CL &= 0.0094\ \mu\mathrm{m}^4 \end{aligned}$$

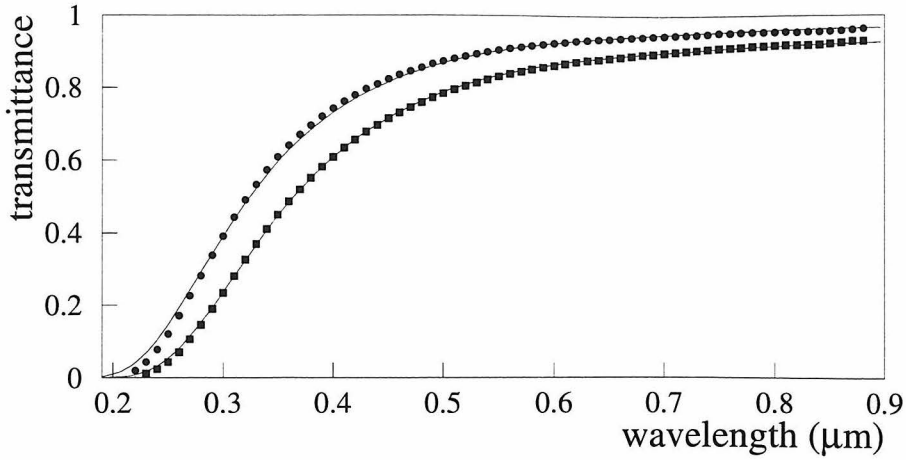

Figure 8.2: Best and worst case transmission spectra of the 200 tiles (1 cm thickness) tested. Two-parameter Rayleigh scattering law fits (Equation 7.5) are superimposed.

The standard deviations for the distributions are 2.4% and 8.3%, respectively.

The absorption spectrum was measured for a single tile using an integrating sphere with the UV-vis spectrophotometer. The absorption is calculated as the ratio of the transmittances measured with and without the tile in the sphere. As expected, the absorption length was measured to be much longer than the scattering length below wavelengths of about 500 nm. Above about 300 nm, the absorption length becomes practically wavelength independent and at the longest wavelengths is comparable or shorter than the scattering length. It is the dominant influence on the Hunt parameter A.

Specularly backscattered light was measured and found to be practically zero, as expected from the low refractive index of aerogel.

8.3 Refractive Index Variations

8.3.1 Optical Dispersion

A straightforward application of Snell's law is used to measure the refractive index of aerogel. It is simple to calculate the exit angle of light incident on a material having flat surfaces that intersect at a right angle, as is the case with an aerogel tile. If the

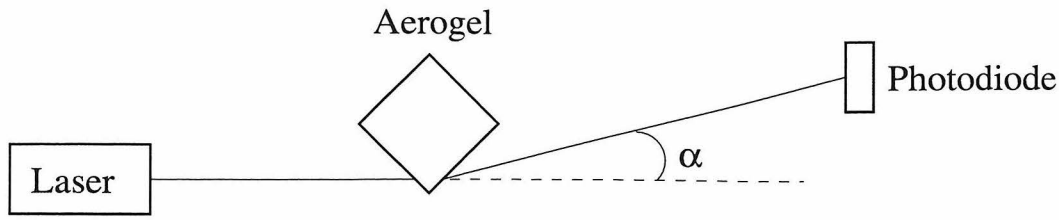

Figure 8.3: Schematic of apparatus for measurement of aerogel dispersion relation.

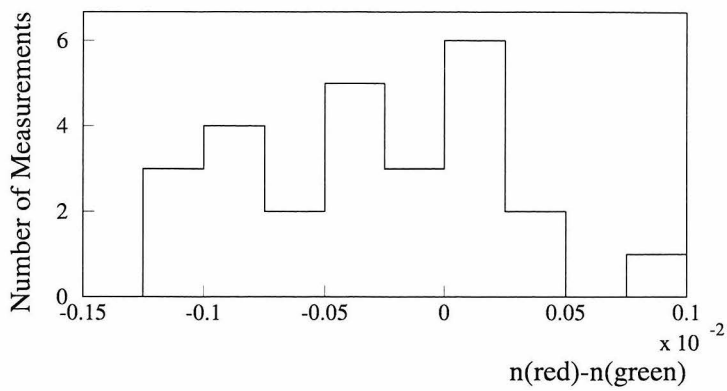

Figure 8.4: Difference in refractive index of aerogel tiles between wavelengths of 633 nm and 544 nm.

light beam is incident at 45° to the normal to the surface, the beam is deflected by an angle α given by

$$\alpha = \arcsin\left(n \sin\left(\frac{\pi}{2} - \arcsin\frac{1}{\sqrt{2}n}\right)\right) - \frac{\pi}{4}.$$

By measuring α, n is easily extracted.

A red (633 nm) or green (544 nm) HeNe laser was shone through a corner of an aerogel tile and the deflected beam angle α was measured with a photodiode sensitive to the beam position. A schematic of the apparatus is shown in Figure 8.3. Refractive index measurements in the red and green were made on several corners of several aerogel tiles (with $n = 1.035$). The results are shown in Figure 8.4. The refractive index changes by $(3.5 \pm 1.0) \times 10^{-4}$ between 544 nm and 633 nm. Equation 7.3 predicts 2.0×10^{-4}. Equation 7.3 is also consistent with earlier measurements of optical dispersion in aerogels taken at wavelengths of 337 and 633 nm.[66]

8.3.2 Density Variations

A linear relationship between refractive index n and density ρ has been measured for aerogels manufactured at DESY and Lund over a range of refractive indices between 1.01 and 1.05. [66] The quantity $\tilde{n}$ was shown to be directly proportional to ρ so that

$$\frac{dn}{\tilde{n}} = \frac{d\rho}{\rho}.$$

Variations in density thus produce refractive index variations that in turn produce variations in the Čerenkov angle.

Direct Density Measurements

Two tiles ($n = 1.035$) were sacrificed for the purpose of measuring density fluctuations. Portions of the tiles were cut with a slitting saw into cubes approximately 8 mm on each side. The density of each cube was calculated from measurements of the mass and volume. The mass was measured using a balance and the volume was measured using a dial indicator. The cube locations within the first of the aerogel tiles and the measured densities are shown in Figure 8.5. The cube locations of the second tile were chosen randomly. The densities shown are not corrected for the buoyancy of aerogel in air, which adds an additional 1.2 mg/cm^3. There is an observable correlation between the measured density and the position of the cube within the tile. The combined density measurements of both tiles (which had a similar average density) are shown in Figure 8.6. The distribution is gaussian with the exception of two measurements at considerably higher density. Taking account of the measurement errors, the density fluctuations extracted from the gaussian fit are 0.6%.

Laser Deflection

These density variations should be compared to the refractive index variations measured with the laser deflection technique. Refractive index variations can be classified into position-independent and position-dependent variations. The refractive index as

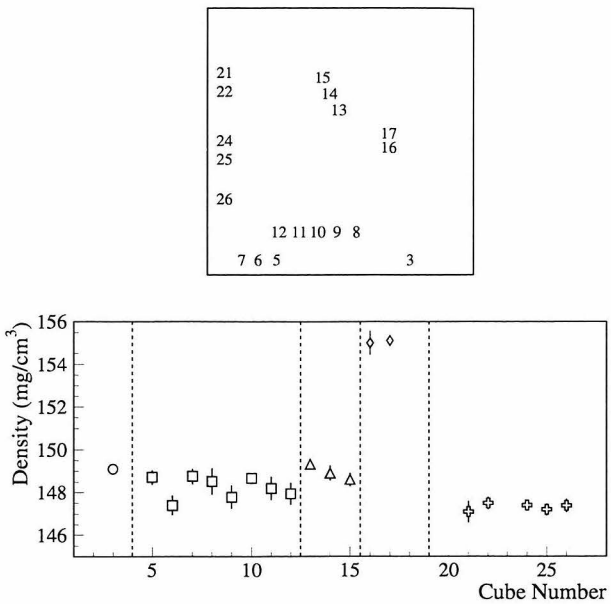

Figure 8.5: Locations of $8\times8\times8\text{mm}^3$ cubes cut from an aerogel tile and the measured density at each location. Dashed lines separate groups of cubes cut from nearby locations within the tile.

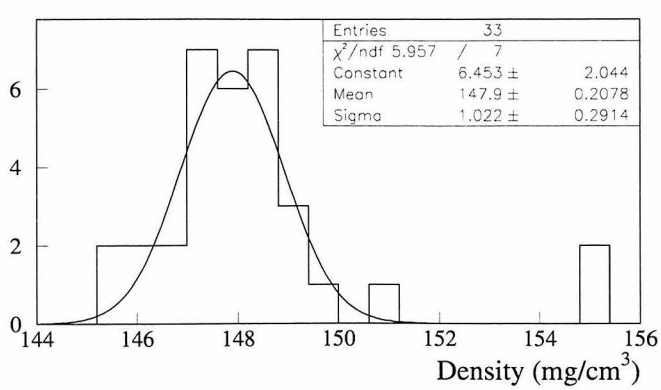

Figure 8.6: Combined results of all density measurements on two aerogel tiles.

a function of position within a given tile is

$$n(x,y,z) = \bar{n} + \epsilon_1 + \epsilon_2(x,y,z)$$
$$\epsilon_1 = \frac{\int\int\int n(x,y,z)dxdydz}{\int\int\int dxdydz} - \bar{n}$$

where $\bar{n}$ denotes the average refractive index of all the tiles in the RICH and the integral is taken over the volume of the tile in question. The position-independent variations are contained in ϵ_1 and the position-dependent variations are contained in ϵ_2.

The total variations are approximately

$$dn^2 = \left(\frac{d\epsilon_1}{G}\right)^2 + d\epsilon_2^2$$

if the tiles are sorted into G groups by refractive index. Divisions of the collection of tiles into smaller groups by refractive index will only reduce the total index variations to a lower limit set by $d\epsilon_2$ since the resolution can only be improved if tiles can be stacked such that n is constant along z for a given x and y. As discussed in Section 7.5.6, it is possible to calibrate large distance scale refractive index changes in the x and y directions if the index is constant along z, but impossible to compensate for refractive index changes along z. In the first case, all Čerenkov photons generated along a track have the same Čerenkov angle, but in the latter case they have different Čerenkov angles. The position-dependent density fluctuations give rise to unavoidable refractive index changes along z and therefore set a lower bound to the total refractive index variations.

Let the refractive indices at each of the four corners of a tile be denoted by $n_1, \ldots, n_4$. The following quantities were measured using laser deflection. [63]

$$\begin{aligned} n_{av} &\equiv \frac{1}{4}(n_1 + \cdots + n_4) = 1.0303 \\ dn_{av} &= 4.1 \times 10^{-4} \\ dn &\equiv dn_1 = \cdots = dn_4 = 4.5 \times 10^{-4} \end{aligned}$$

$$
\begin{aligned}
d(n - n_{av}) &\equiv d(n_1 - n_{av}) = \cdots = d(n_4 - nav) = 1.9 \times 10^{-4} \\
dm &\equiv \text{single measurement error} = 1.6 \times 10^{-4}
\end{aligned}
$$

The following relationships between these quantities and $d\epsilon_1$ and $d\epsilon_2$ hold,

$$
\begin{aligned}
dn^2 &= d\epsilon_1^2 + d\epsilon_2^2 + dm^2 \\
dn_{av}^2 &= d\epsilon_1^2 + \frac{1}{4} d\epsilon_2^2 + \frac{1}{4} dm^2 \\
d(n - n_{av})^2 &= \frac{12}{16} \left(d\epsilon_2^2 + dm^2 \right)
\end{aligned}
\tag{8.1}
$$

so that $d\epsilon_1$ and $d\epsilon_2$ are overdetermined. They are found to be

$$
\begin{aligned}
d\epsilon_1 &= 4.0 \times 10^{-4} \\
d\epsilon_2 &= 1.4 \times 10^{-4}
\end{aligned}
$$

and the three equations are found to be consistent. The laser deflection measurements show a 0.5% position-dependent index variation in good agreement with the density measurements.

The position-independent index variation of the entire collection of tiles $d\epsilon_1/\tilde{n}$ is 1.3%. By sorting tiles according to their average refractive indices, the tiles were placed into stacks in such a way that the position-independent index variations within each stack, plotted in Figure 8.7, were reduced to an average of $d\epsilon_1/G\tilde{n} \approx dn_{\text{av}}^{\text{stack}}/\tilde{n} =$ 0.5%.

8.4 Tile Thickness Variations

Variations in refractive index and path length due to local density fluctuations and tile surface features can deflect the trajectories of photons away from the Čerenkov cone. The deflection is approximately

$$
d\vec{\theta} = \hat{z} \times \nabla \left\{ \tilde{n}(x, y)\, L(x, y) \right\}, \tag{8.2}
$$

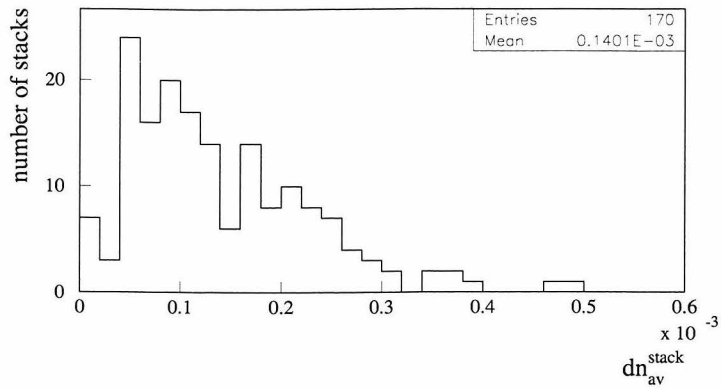

Figure 8.7: Position-independent refractive index variations within tile stacks.

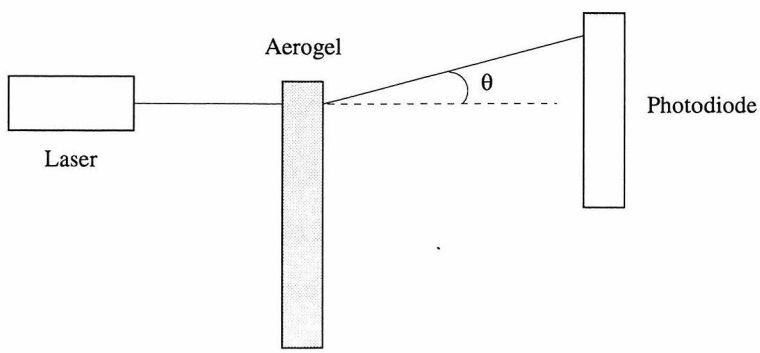

Figure 8.8: Schematic of apparatus for measuring light propagation near tile edges.

where x and y are lateral dimensions along the tile, z is normal to the surface, and $L(x, y)$ is the tile thickness. Variations in thickness or density will give rise to distortions.

A laser setup shown schematically in Figure 8.8 was used to measure light deflection near tile edges. The deflection of a laser beam through a single aerogel tile as a function of the distance from the tile edge is shown in Figure 8.9. The Figure displays measurements made on three different tile edges and demonstrates that light trajectories are deflected in a fairly consistent manner. It is difficult to make measurements closer than about 2 mm from the tile edge because poor surface quality and the rapid increase in tile thickness come into play, giving large deflections in unpredictable directions.

Using Figure 8.9 and Equation 8.2, the product $L \times \tilde{n}$ is deduced to be more than

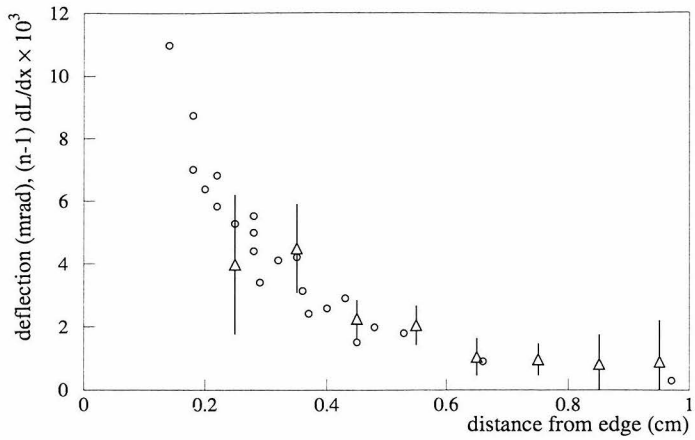

Figure 8.9: Measured light deflection near tile edges (circles) compared with measured gradient of tile thickness (triangles).

10% higher at the tile edges than at locations 1 cm from the edge. There are several indications that it is L that increases rather than n. The gradient of the tile thickness has been measured and the deflection calculated according to Equation 8.2 assuming constant n is shown in Figure 8.9. The amount of deflection is consistent with the observed beam deflections. In contrast, the measurements of Section 8.3.2 do not show an appreciable increase in density near the edges.

The deflections near tile edges are important and will result in both distortions of the Čerenkov rings and shifts in position with respect to the expected ring location. Approximately 10% of all Čerenkov rings will be deflected by more than 4 mrad. The impact on the resolution is difficult to estimate without detailed Monte Carlo studies.

8.5 Small Angle Light Scattering

One of the surprising features of aerogel is that while the random two phase medium model describes the scattering well, not one but two different correlation lengths are required [67, 68, 69]. The first correlation length, typically in the range of a few nanometers, describes scattering in the bulk of the aerogel material. A much longer correlation length describes surface scattering.

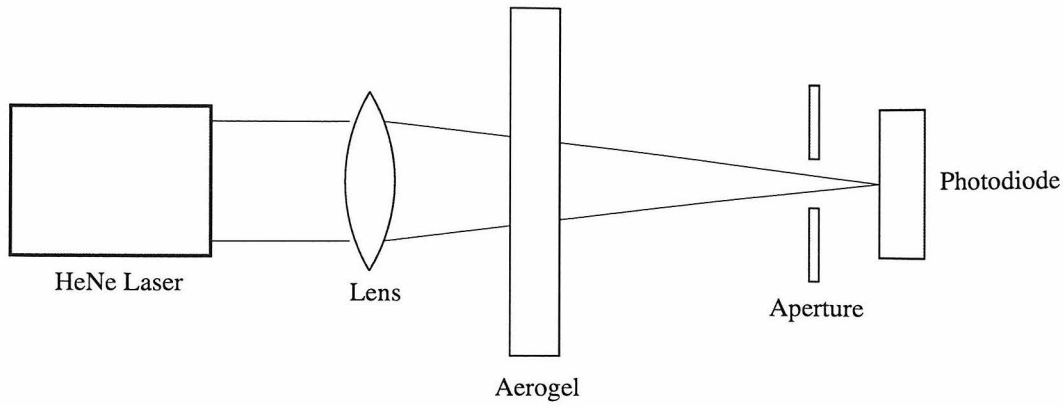

Figure 8.10: Schematic of light scattering measurement apparatus.

This surface correlation length is comparable to the visible wavelengths of interest, giving rise to a forward peaked distribution of scattered light. Samples of earlier generations of aerogel scattered light through several degrees. It is this surface scattering that gives rise to the "hazy" appearance of objects viewed through aerogel of low quality. This level of surface scattering would be disastrous in a RICH counter in which a resolution on the order of 1 mrad is required, so it is important to measure the surface scattering in HERMES aerogel. It is clear simply by looking through a HERMES aerogel tile that the surface scattering is not significant at the level of a few degrees.

To study the deflection of forward surface scattered light in the HERMES aerogel, the transmitted power of a laser beam passing through an aerogel tile and then through an aperture was measured as a function of the solid angle subtended by the aperture. A schematic of the apparatus is shown in Figure 8.10. A 544 nm or 633 nm HeNe laser beam was focused on a photodiode using a convex lens of focal length 100 cm. A circular aperture 1 mm in diameter was centered about the beam a few cm from the photodiode. Larger aperture sizes were also used for some measurements. Without aerogel placed in the beam, the power transmitted through the aperture was nearly 100% of the power with no aperture. An aerogel tile was then placed in the laser beam and the aperture was moved moved towards or away from the tile using a computer-controlled motorized translator. The transmitted power passing through the aperture was recorded.

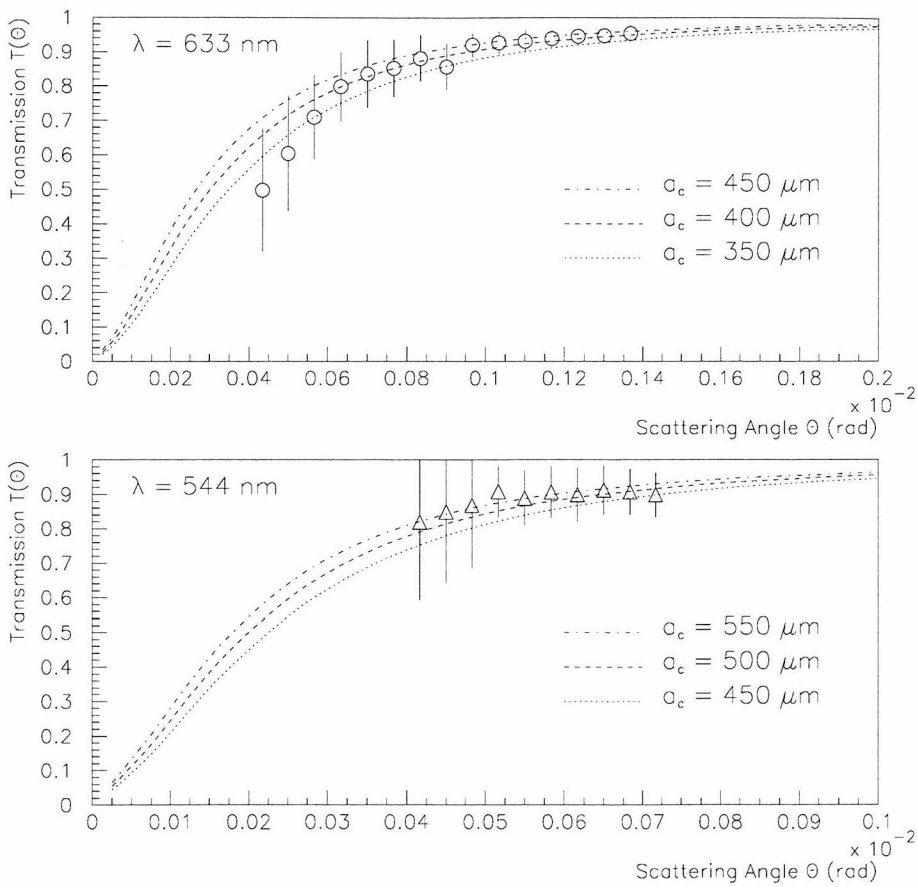

Figure 8.11: Angular profile of laser light scattered by aerogel. Error bars represent the width of the distribution of transmissions measured for several different tiles and locations within the tiles.

The fraction of laser light transmitted as a function of the polar angle subtended by the aperture is shown as a profile histogram in Figure 8.11. The error bars represent the widths of the transmissions measured for several different tiles and locations within the tiles. Also shown on the figures are predictions based on Equations 7.4 and 7.5 using several different values for the correlation length. The scattering is qualitatively well described using a correlation length of $a_c = 450$ microns. The range of correlation lengths is approximately ± 200 microns.

The correlation lengths measured for aerogel samples produced in two separate batches differed by a factor of 3. The difference in correlation lengths between batches suggests that the surface scattering is due to features produced during the manufacturing process rather than extrinsic effects such as dust particles or scratches.

Chapter 9 Projected Performance

9.1 Contributions to the Aerogel Ring Resolution

The number of photomultipliers fired per relativistic track is expected to be more than 11 in the ideal case, i.e. tracks that pass through the centers of aerogel tiles and whose rings are fully contained within the acceptance of the mirror array. Tracks with small vertical scattering angles produce Čerenkov cones that partially overlap the floor of the RICH, resulting in a loss of light. The acceptance for the rings is approximately 30% lower in the innermost rows of aerogel tiles compared to the rest of the other rows. Since a large portion of the particle flux strikes the innermost rows, this significantly reduces the light yield. For the purpose of estimating the aerogel ring resolution, 9 photoelectrons per ring will be taken as the average yield.

9.1.1 Pixel Size

For each track generating an aerogel ring in the RICH, the Čerenkov angles are calculated for each photomultiplier that fires using the center of the photomultiplier as the location of the detected photon. The difference between the center of the photomultiplier and the actual hit location can be as large as the photomultiplier's radius, so the finite size of the photomultiplier introduces an uncertainty in the reconstructed angle. For an array of photomultipliers of diameter D measuring circular Čerenkov rings of radius R, the pixel size contribution to the ring resolution is approximately

$$\left(\frac{d\theta}{\theta}\right)_{\text{pixel size}} = \frac{D}{4R}\frac{1}{\sqrt{N_{\text{pe}}}}$$

With $D = 2.3$ cm, $R = 26$ cm, and $N_{\text{pe}} = 9$, the above formula gives a resolution of approximately 0.8%. In reality, the rings are not perfectly circular so that the pixel

resolution is 1.0%.

9.1.2 Dispersion Relation

Using Equation 7.3 and the distribution of detected unscattered Čerenkov light presented in Figure 7.5, the expected variations in the refractive index due to optical dispersion are calculated to be approximately $dn = 5 \times 10^{-4}$. Optical dispersion therefore contributes to the ring resolution in the amount

$$\left(\frac{d\theta}{\theta}\right)_{\text{dispersion}} = \frac{1}{2}\frac{dn}{\tilde{n}}\frac{1}{\sqrt{N_{\text{pe}}}} \approx 0.3\%$$

9.1.3 Density Fluctuations

Density variations contribute to the ring resolution in the amount

$$\frac{d\theta}{\theta} = \frac{1}{2}\frac{dn}{\tilde{n}} = \frac{1}{2}\frac{d\rho}{\rho} \tag{9.1}$$

The usual factor of $\sqrt{N_{\text{pe}}}$ is omitted in this case. Assuming for the moment that density fluctuations are the only source of smearing of the Čerenkov rings, a stack of ℓ aerogel layers, each with its own constant density, will give rise to ℓ discrete (zero width) Čerenkov rings when a charged particle traverses the stack. If $N_{\text{pe}} \ll \ell$, the number of photons per ring is much less than one so that each photon provides *unique* information about the Čerenkov angle, and in calculating the uncertainty in the average Čerenkov angle, a factor of $\sqrt{N_{\text{pe}}}$ should be included. On the other hand, if $N_{\text{pe}} \gg \ell$, the average number of photons per ring is much greater than one, and most of the photons provide only *redundant* information about the Čerenkov angle. There are at most only ℓ *different* position measurments so that at best, a factor of $\sqrt{\ell}$ should be inserted in Equation 9.1.

A Monte Carlo calculation was used to study the ring resolution as a function of N_{pe} with $\ell = 5$. The results are shown in Table 9.1. The resolution does improve with increasing N_{pe}, but not as quickly as $\sqrt{N_{\text{pe}}}$. For $N_{\text{pe}} = 9$, the contribution of

N_{pe}	Monte Carlo resolution	$\frac{0.9\%}{\sqrt{N_{pe}}}$
1	0.90%	0.90%
2	0.82%	0.63%
4	0.71%	0.45%
8	0.60%	0.31%
14	0.58%	0.24%

Table 9.1: Monte Carlo calculation of ring resolution due to density fluctuations as a function of N_{pe}.

the position-dependent density fluctuations to the ring resolution should be reduced by a factor of approximately 2/3 rather than 1/3.

Position-Dependent

The laser deflection measurements and direct density measurements revealed a position-dependent index variation of the order of 0.5%. This results in $d\theta/\theta \approx 0.2\%$.

Position-Independent

The aerogel tiles were arranged in stacks in such a way as to minimize the position-independent index variations. The position-dependent index variations in each stack were measured to be 0.5%, giving $d\theta/\theta \approx 0.2\%$.

9.1.4 Light Scattering

The contribution from forward surface scattering to the aerogel ring resolution can be estimated based on the measurements of Figure 8.11. Assuming a correlation length of 450 microns, the angular deflection is less than 1 mrad for 633 nm photons that pass through three aerogel surfaces (the typical case). The wavelengths of the detected non-Rayleigh scattered radiation are predominantly near 400 nm, and according to Equation 7.5, the angular deflection at 400 nm is approximately 2/3 the deflection at

contribution	resolution
pixel size	1.0%
dispersion	0.3%
density, position-dependent	0.2%
density, position-independent	0.2%
scattering	0.1%
total	1.1%

Table 9.2: Summary of contributions to the aerogel ring resolution.

600 nm. The impact on the ring resolution can therefore be estimated as

$$\left(\frac{d\theta}{\theta}\right)_{\text{scattering}} = \frac{2}{3}\frac{1 \text{ mrad}}{242 \text{ mrad}}\frac{1}{\sqrt{N_{\text{pe}}}} \approx 0.1\%.$$

9.2 Summary

The estimates of the previous section comprise the more easily quantifiable influences on the aerogel ring resolution. These are summarized in Table 9.2. The overall resolution to be expected from all the effects discussed is about 1.1%, well below the goal of 1.4%. The resolution is dominated by the pixel size, with little impact from the optical characteristics of the aerogel radiator beyond the photoelectron yield. The result is consistent with the resolution measured in the CERN beam tests described in Section 8.1.1. Other influences on the ring resolution that are difficult to estimate include small irregularities in the shape of the spherical mirror and backgrounds from sources including overlapping rings, Rayleigh-scattered photons, and photomultiplier noise.

This estimate of the resolution is expected to be realistic for tracks passing near the centers of the aerogel stacks. However, as discussed in Section 7.5.5, tile edge effects come into play for tracks within about 0.5 cm of a tile edge, or roughly 20% of all tracks. These effects are difficult to quantify and require accurate modeling in a Monte Carlo simulation of the detector in order to be studied properly. The next chapter will explore tile edge effects observed in the analysis of recently collected data. The resolution near the tile edges will be affected by both the reduction in

the photoelectron yield due to photons that strike the tedlar foils and the smearing of the rings due to the tile thickness variations. The resolution near the edges may very well be worse than the 1.4% level, giving a ring separation less than 3σ near the kaon gas threshold, but according to Figure 6.5, the separation increases rapidly with decreasing momentum so that the particle identification will be compromised only within a limited momentum range.

The tile edge effects could be reduced substantially with larger, thicker, and flatter tiles. This was not possible in the aerogel production for the HERMES RICH. The increase in size is difficult to achieve without compromising optical quality. Attempts have been recently made to produce tiles with dimensions $30 \times 20 \times 2$ cm^3 for a future upgrade of the aerogel radiator, but with only limited success thus far.

Chapter 10 Early Results

The HERMES RICH began operation in August 1998. Observations of gas and aerogel rings followed soon after, making HERMES the first physics experiment to operate an aerogel-based RICH.

A sample event is shown in Figure 10.1. A track has been reconstructed in each half of the detector. The top half has a 4.1 GeV track and the bottom one has a 3.1 GeV track. Information from other PID detectors in the spectrometer indicates they are hadron tracks. The RICH portion of the display shows that the top track has a nearly full sized aerogel ring but no gas ring, indicating a kaon track. The bottom track has a full size aerogel ring and a small gas ring and is thus identified as a pion.

The data analysis is in its early stages of development. The spherical mirror alignment assumed in the analysis has not yet been fully optimized, and since it influences the reconstruction of the size and width of the aerogel rings, current results must be considered preliminary. Even so, it is already possible to discern some general features of the data. For example, the number of photmultipliers fired per aerogel ring decreases near the tile edges while the ring width increases as shown in Figure 10.2.

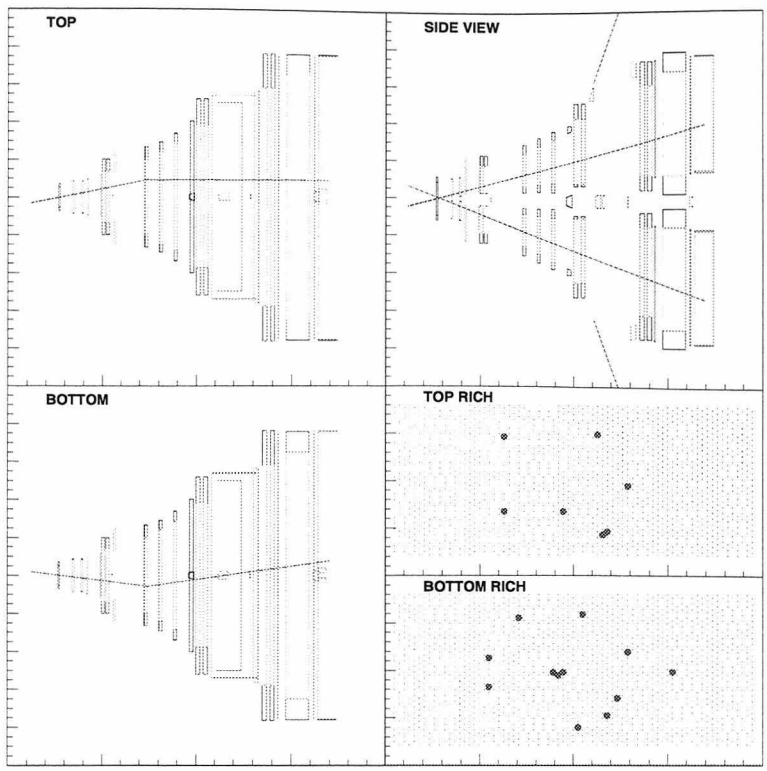

Figure 10.1: Event display showing Čerenkov rings detected by the RICH.

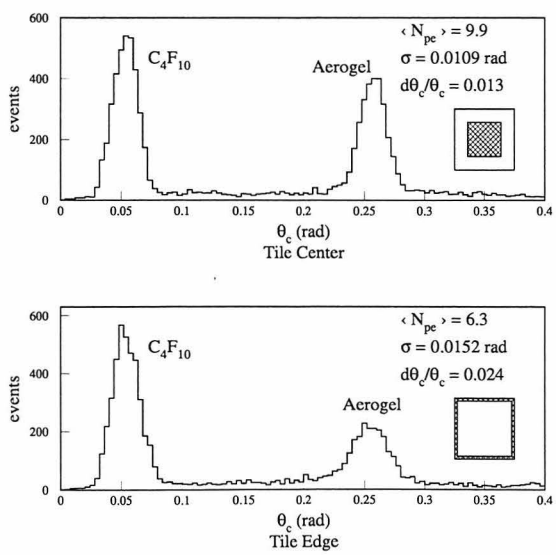

Figure 10.2: Preliminary reconstructed Čerenkov angles of single photons generated by positron tracks near tile centers (top) and edges (bottom). The regions of the tiles selected are shown by the hatched areas of the inset squares.

Part IV

Summary

Chapter 11 Conclusions and Future Prospects

The HERMES experiment has made the first measurement of the spin and azimuthal dependence of semi-inclusive charged pion electroproduction with a significantly positive result in the π^+ channel. A number of related measurements are already analyzeable or will be available in the near future.

Polarized ^{3}He target data from the 1995 running period are available for analysis. These data are limited by low target polarization (less than 50%) and low statistics. Pure nitrogen gas was used for the 1995 running period, placing the Čerenkov thresholds for pions and kaons at 5.7 and 20.2 GeV, respectively. The size of the asymmetry is expected to be small.

Based on theoretical expectations [12, 21] and experimental results from polarized hadron–hadron scattering [16], the π^0 asymmetry is expected to lie between the π^+ and π^-. HERMES is capable of reconstructing π^0 decays with the use of the calorimeter, so it is possible to calculate the analyzing powers for this channel. The π^0 channel has somewhat less potential than the charged pions due to lower acceptance and the presence of background. The background comes mostly from uncorrelated photons, many from π^0, that can also have a significant analyzing power. It is therefore necessary to measure the asymmetry of the background and make the appropriate subtraction.

Low momentum hadrons may be indentified using time of flight techniques. [40, 70] The HERA bunch crossing signal is used as starting time input to TDCs and signals from the hodoscope planes H1 and H2 as stopping time inputs. The hodoscopes are 6–7 m from the target cell, providing a roughly 20 ns delay. Pions, kaons, and protons can be identified below about 1.5 GeV and proton separation from pions and kaons is possible up to about 2.5 GeV. These samples could be used to calculate analyzing

powers at low z.

Several unpolarized azimuthal moments such as $\langle \cos\phi \rangle_{00}$ and $\langle \cos 2\phi \rangle_{00}$ contain interesting physics, as discussed in Section 4.5. The unpolarized $\cos\phi$ moment has been measured in deep inelastic muon scattering experiments [44, 45], and a preliminary analysis suggests an even larger effect at HERMES where the enhancement may be due to its relatively low Q^2 [46]. In Appendix A the $\cos\phi$ moment is shown as a twist-3 effect involving relatively exotic distribution and fragmentation functions. The unpolarized $\cos 2\phi$ moment is twist-2 and involves the combination $h_1^\perp H_1^\perp$, where $h_1^\perp$ is a twist-2 T-odd distribution function describing transverse quark polarization in an unpolarized nucleon. The measurement of unpolarized moments is strongly influenced by the acceptance, and will require a more detailed Monte Carlo analysis.

Perhaps the most exciting possibility is the incoming 1998 data on a polarized deuterium target. With the availability of the RICH, it is possible to separate the azimuthal asymmetries of pions, kaons, and protons throughout a much larger momentum range. The suggestion of a measurable signal in the 1996 and 1997 data in the proton and/or kaon channel makes this analyis a very interesting prospect.

Appendix A Leptoproduction Cross Sections

The tree level spin independent and target spin dependent cross sections up to order $1/Q$ of pion electroproduction containing contributions from T-even distribution functions are shown below. [3]

$$\frac{d\sigma_{00}}{dxdydzd^2\mathbf{p}_\perp} = -\frac{4\pi\alpha^2 s}{Q^4}\sum_{a,\bar{a}} e_a^2 \left\{ \left(\frac{y^2}{2}+1-y\right) x f_1^a(x) D_1^a(z) - 2(2-y)\sqrt{1-y}\cos(\phi)\frac{Q_T}{Q}\times \left(\frac{R^2}{R_H^2}x^2 f^{\perp a}(x) D_1^a(z) - \frac{R^2}{R_h^2} x f_1^a(x)\frac{\tilde{D}^{\perp a}(z)}{z}\right)\right\}\frac{\mathcal{G}(Q_T;R)}{z^2}$$

$$\frac{d\sigma_{0L}}{dxdydzd^2\mathbf{p}_\perp} = -\frac{4\pi\alpha^2 s}{Q^4}\lambda\sum_{a,\bar{a}} e_a^2 \left\{ (1-y)\sin(2\phi)\frac{Q_T^2 R^4}{M M_h R_H^2 R_h^2} x h_{1L}^{\perp a}(x) H_1^{\perp a}(z) - 2(2-y)\sqrt{1-y}\sin(\phi)\frac{Q_T}{Q}\left(\frac{R^6}{M M_h R_H^4 R_h^4}\left(\frac{R_h^2-R_H^2}{R^2} - Q_T^2 R_h^2\right) x h_{1L}^{\perp a}(x) H_1^{\perp a}(z) + \frac{M R^2}{M_h R_h^2} x^2 \tilde{h}_L^a(x) H_1^{\perp a}(z) - \frac{M_h R^2}{M R_H^2} x h_{1L}^{\perp a}\frac{\tilde{H}^a(z)}{z}\right)\right\}\frac{\mathcal{G}(Q_T;R)}{z^2}$$

$$\frac{d\sigma_{0T}}{dxdydzd^2\mathbf{p}_\perp} = -\frac{4\pi\alpha^2 s}{Q^4}|\mathbf{S}_\perp|\sum_{a,\bar{a}} e_a^2 \left\{ (1-y)\sin(\phi+\phi_s)\frac{Q_T R^2}{M_h R_h^2} x h_1^a(x) H_1^{\perp a}(z) + (1-y)\sin(3\phi-\phi_s)\frac{Q_T^3 R^6}{2M^2 M_h R_H^4 R_h^2} x h_{1T}^{\perp a}(x) H_1^{\perp a}(z)\right.$$

$$
\begin{aligned}
&- 2(2-y)\sqrt{1-y}\sin(\phi_s) \times \\
&\left(\frac{Q_T}{Q} \frac{Q_T R^8}{2M^2 M_h R_H^6 R_h^4} \left(\frac{2R_H^2 - R_h^2}{R^2} + Q_T^2 R_h^2 \right) x h_{1T}^{\perp a}(x) H_1^{\perp a}(z) \right. \\
&+ \frac{M_h}{Q} x h_1^a(x) \frac{\tilde{H}(z)}{z} - \frac{Q_T}{Q} \frac{Q_T R^4}{2M_h R_H^2 R_h^2} x^2 \left(\tilde{h}_T^a(x) + \tilde{h}_T^{\perp a}(x) \right) H_1^{\perp a}(z) \Bigg) \\
&+ 2(2-y)\sqrt{1-y}\sin(2\phi - \phi_s) \left(\frac{Q_T}{Q} \frac{Q_T R^4}{2M_h R_H^2 R_h^2} x \left(2h_1^a(x) - x\tilde{h}_{1L}^{\perp a}(x) \right) H_1^{\perp a}(z) \right. \\
&\left. \left. - \frac{M_h}{Q} \frac{Q_T^2 R_4}{2M^2 R_H^4} x h_{1T}^{\perp a}(x) \frac{\tilde{H}^a(z)}{z} \right) \right\} \frac{\mathcal{G}(Q_T; R)}{z^2}
\end{aligned}
$$

The subscripts of the cross sections represent the polarizations of the beam and target hadrons, with L for longitudinal polarization and T for transverse polarization.

The distribution and fragmentation functions appearing in the cross sections are summarized in Appendix B. The functions with tildes are obtained by splitting twist-3 distribution or fragmentation functions into a twist-2 part and an interaction dependent part. For example,

$$
\begin{aligned}
h_L(x) &= -2\frac{h_{1L}^{\perp(1)}(x)}{x} + \frac{m}{M}\frac{g_1(x)}{x} + \tilde{h}_L(x) \\
h_{1L}^{\perp(1)} &\equiv \int d^2\mathbf{p}_T \frac{\mathbf{p}_T^2}{2M^2} h_{1L}^{\perp}(x, \mathbf{p}_T^2).
\end{aligned}
$$

There are also relationships between the distribution functions such as

$$
h_L(x) = h_1(x) - 2\frac{d}{dx} h_{1L}^{\perp(1)}(x).
$$

In the above expressions for the cross sections a gaussian form is assumed for the transverse momentum dependence of the distribution and fragmentation functions with a width characterized by the radii R_H and R_h, respectively.

$$
\begin{aligned}
f(x, \mathbf{p}_T^2) &= f(x, 0)\exp(-R_H^2 \mathbf{p}_T^2) \\
&= f(x)\frac{R_H^2}{\pi}\exp(-R_H^2 \mathbf{p}_T^2) \equiv f(x)\mathcal{G}(|\mathbf{p}_T|; R_H) \\
D(z, \mathbf{k}_T^2) &= D(z, 0)\exp(-R_h^2 \mathbf{k}_T^2) \\
&= D(z)\frac{R_h^2}{\pi z^2}\exp(-R_h^2 \mathbf{k}_T^2) = \frac{D(z)}{z^2}\mathcal{G}(|\mathbf{k}_T|; R_h) = D(z)\mathcal{G}\left(z|\mathbf{k}_T|; \frac{R_h}{z}\right)
\end{aligned}
$$

It is possible to have hadronic radii that depend on the distribution and fragmentation functions so that for example $R_H \to R_H^f$. For the purpose of calculating cross sections, the convolution of the distribution and fragmentation functions becomes

$$\begin{aligned}\int d^2\mathbf{p}_T f(x,\mathbf{p}_T^2 D(z,|\mathbf{p}_\perp - z\mathbf{p}_T|^2) &= \frac{\pi}{R_H^2+R_h^2}\exp\left(-\frac{Q_T R_H^2 R_h^2}{R_H^2+R_h^2}\right) f(x,0)D(z,0) \\ &= f(x)D(z)\frac{\mathcal{G}(Q_T;R)}{z^2}\end{aligned}$$

with $Q_T \equiv p_\perp/z$ and $R^2 \equiv R_H^2 R_h^2/(R_H^2+R_h^2)$.

ϕ_s is the azimuthal angle of the target spin with respect to the lepton scattering plane. For a target polarized longitudinally with respect to the incoming lepton beam, the target spin is contained in the lepton scattering plane. The longitudinal component of the target polarization λ may be written $\lambda = s_\lambda |\lambda|$ where s_λ is the target helicity. It follows that $\phi_s = (1+s_\lambda)\pi/2$ and so

$$\sin(\phi - \phi_s) = -s_\lambda \sin\phi$$

Reference [3] appears to use a different ϕ convention from that of this thesis which flips the sign of ϕ.

In addition to the above contributions to the cross section, the following cross section appears at leading order when T-odd distribution functions are allowed: [71]

$$\left\langle \frac{Q_T}{M}\sin(\phi_h - \phi_s)\right\rangle_{0T} = \frac{4\pi\alpha^2 s}{Q^4}|\mathbf{S}_\perp|(1-y+\frac{1}{2}y^2)\sum_{a,\bar{a}} e_a^2 x f_{1T}^{\perp(1)a}(x)D_1^a(z)$$

where in this case

$$\langle W\rangle_{AB} = \int dp_\perp d\phi \frac{W d\sigma_{AB}}{dxdydzdp_\perp d\phi}$$

This contribution represents the Sivers mechanism. There is also an interesting un-

polarized moment involving a T-odd distribution that appears at leading order:

$$\left\langle \frac{Q_T^2}{4MM_h}\cos(2\phi_h)\right\rangle_{00} = \frac{4\pi\alpha^2 s}{Q^4}(1-y)\sum_{a,\bar{a}} e_a^2 x h_1^{\perp(1)a}(x) H_1^{\perp(1)a}(z)$$

Appendix B Distribution and Fragmentation Functions in Leptoproduction

The distribution and fragmentation functions involved in pion leptoproduction are summarized in the Tables B.1, B.2, B.3, and B.4. [72] Those in boldface survive after integration over transverse momenta.

T-even Distribution			
twist	polarization	chiral even	chiral odd
2	0	$\mathbf{f}_1$	
	L	$\mathbf{g}_{1L}$	$h_{1L}^{\perp}$
	T	g_{1T}	$\mathbf{h}_1$ $h_{1T}^{\perp}$
3	0	$f^{\perp}$	$\mathbf{e}$
	L	$g_L^{\perp}$	$\mathbf{h}_L$
	T	$\mathbf{g}_T$ $g_T^{\perp}$	h_T $h_T^{\perp}$

Table B.1: Summary of T-even distribution functions.

T-odd Distribution			
twist	polarization	chiral even	chiral odd
2	0		$h_1^{\perp}$
	L		
	T	$f_{1T}^{\perp}$	
3	0		$\mathbf{h}$
	L	$f_L^{\perp}$	$\mathbf{e}_L$
	T	$\mathbf{f}_T$	e_T

Table B.2: Summary of T-odd distribution functions.

The twist-2 functions have interpretations in terms of quark spin densities as pictured in Figures B.1 and B.2. [72]

T-even Fragmentation			
twist	polarization	chiral even	chiral odd
2	0	$\mathbf{D}_1$	
	L	$\mathbf{G}_{1L}$	$H_{1L}^{\perp}$
	T	G_{1T}	$\mathbf{H}_1$ $H_{1T}^{\perp}$
3	0	$D^{\perp}$	$\mathbf{E}$
	L	$G_L^{\perp}$	$\mathbf{H}_L$
	T	$\mathbf{G}_T$ $G_T^{\perp}$	H_T $H_T^{\perp}$

Table B.3: Summary of T-even fragmentation functions.

T-odd Fragmentation			
twist	polarization	chiral even	chiral odd
2	0		$H_1^{\perp}$
	L		
	T	$D_{1T}^{\perp}$	
3	0		$\mathbf{H}$
	L	$D_L^{\perp}$	$\mathbf{E}_L$
	T	$\mathbf{D}_T$	E_T

Table B.4: Summary of T-odd fragmentation functions.

The familiar polarized distribution functions g_1 and g_2 are given by

$$\begin{aligned} g_1 &= g_{1L} \\ g_2 &= g_T - g_1 = \frac{d}{dx} g_{1T}^{(1)} \end{aligned}$$

Some useful rules of thumb are listed below: [24]

1. Twist-2 functions are labeled with a '1'.

2. Functions in which quark intrinsic transverse momenta play an important role are labeled with a '$\perp$'.

3. 'L' and 'T' refer to the longitudinal or transverse polarization of the proton or the produced hadron.

4. e functions involve matrix elements of scalar or pseudoscalar operators, f functions involve vector operators, g functions involve pseudovector operators, and

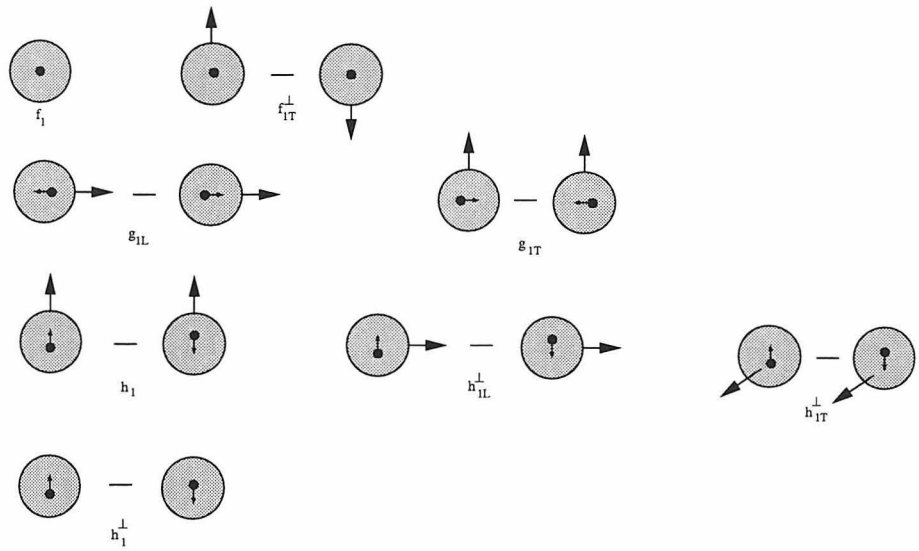

Figure B.1: Interpretation of twist-2 distribution functions.

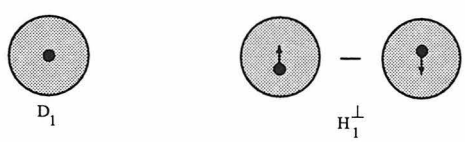

Figure B.2: Intepretation of selected twist-2 fragmentation functions.

h functions involve second rank tensor operators. The analogous fragmentation functions are labeled E, D, G, and H, respectively.

5. f and D describe unpolarized quarks in the proton and hadron, respectively. g and G describe longitudinally polarized quarks, and h and H describe transversely polarized quarks.

6. Chiral even functions are f, g, D, and G. Chiral odd functions are e, h, E, H.

7. The chirality structure of the distribution $\otimes$ fragmentation functions appearing in the cross section must be even $\otimes$ even or odd $\otimes$ odd.

8. The time reversal structure of single-spin-dependent cross sections is even $\otimes$ odd or odd $\otimes$ even. For unpolarized or doubly polarized cross sections it is even $\otimes$ even or odd $\otimes$ odd.

Appendix C Introduction to Twist

It is useful to introduce the term *twist* used frequently in this thesis. This Appendix is based on Reference [10] where a much more detailed discussion can be found.

The twist of an operator has a formal definition within the context of the operator product expansion analysis of deep inelastic scattering. The hadronic tensor may be written

$$4\pi W = \int d^4\xi e^{iq\cdot\xi} \langle P,S | [J_\mu(\xi), J_\nu(\xi)] | P,S \rangle .$$

The integral is dominated by the region $\xi^2 \sim 0$ for $Q^2 \to \infty$, so the current commutator can be expanded about $\xi^2 = 0$ as a sum of terms involving local operators:

$$[J(\xi), J(0)] \sim \sum_{[\theta]} K_{[\theta]}(\xi^2)\xi^{\mu_1} \ldots \xi^{\mu_{n_\theta}} \theta_{\mu_1 \ldots \mu_{n_\theta}}(0)$$

where $K_{[\theta]}(\xi^2)$ are singular complex functions that can be ordered according to their singularity at $\xi^2 = 0$. The matrix elements of these operators have the form

$$\left\langle P \left| \theta_{\mu_1 \ldots \mu_{n_\theta}}(0) \right| P \right\rangle = P_{\mu_1} \ldots P_{\mu_{n_\theta}} M^{d_\theta - n_\theta - 2} f_\theta + \ldots$$

where f_θ is a constant, M represents a hadronic mass scale, and the terms in $\ldots$ can be neglected for the purpose of this discussion. The twist of the operator θ is given by $t_\theta \equiv d_\theta - n_\theta$. Fourier transforming the result for the hadronic tensor leads to

$$4\pi W \sim \sum_{[\theta]} \left(\frac{M}{Q}\right)^{t_\theta - 2} \left(\frac{1}{x}\right)^{n_\theta} f_\theta .$$

Thus the twist of the operator is related to the order in M/Q in which it contributes to the hadronic tensor.

The term twist is typically used in less formal ways than $t_\theta = d_\theta - n_\theta$. In the first

case, it is used to classify distribution and fragmentation functions. The distributions can be viewed as discontinuities in forward parton-hadron scattering. A useful fact is that twist is related to the number of dynamically independent good light cone components of the quark fields and the number of bad components involved in the forward scattering amplitude. Twist-2 objects ($f_1, g_1, h_1, \ldots$) are amplitudes involving good components exclusively, allowing an interpretation in terms of the quark parton model. Higher twist objects ($h_L, g_T, \ldots$) involve bad components, and if the equations of motion are used to eliminate the bad components, the matrix elements are found to correlate both quark and gluon fields. Thus the higher twist objects have no partonic interpretation in terms of quark spin densities alone.

More generally, the twist labels the order in M/Q at which a given process appears in a deep inelastic cross section. A process with twist t appears as $(M/Q)^{t-2}$. In SIDIS, for instance, the Collins effect involves a twist-2 distribution function and a twist-2 fragmentation function and appears at twist-2 in σ_{0T}. The twist of the distribution or fragmentation function denotes the lowest order at which it can appear in a cross section.

Appendix D Multiplication of Fourier Series

Let σ and ϵ be two functions of ϕ written as follows as Fourier series:

$$\begin{aligned}\sigma(\phi) &= 1+\sum_m \left(a_m \cos m\phi + b_m \sin m\phi\right), \\ \epsilon(\phi) &= 1+\sum_m \left(A_m \cos m\phi + B_m \sin m\phi\right).\end{aligned}$$

Then the product is given by

$$\begin{aligned}\sigma\epsilon = \;& 1+\frac{1}{2}\sum_m \left(A_m a_m + B_m b_m\right) + \\ & \cos\phi\left[a_1 + A_1 + \frac{1}{2}\sum_m \left(A_m a_{m+1} + a_m A_{m+1} + B_m b_{m+1} + b_m B_{m+1}\right)\right] + \\ & \sin\phi\left[b_1 + B_1 + \frac{1}{2}\sum_m \left(-B_m a_{m+1} + a_m B_{m+1} + A_m b_{m+1} - b_m A_{m+1}\right)\right] + \\ & \cos 2\phi\left[\begin{array}{c} a_2 + A_2 + \frac{1}{2}\sum_m \left(A_m a_{m+2} + a_m A_{m+2} + B_m b_{m+2} + b_m B_{m+2}\right) + \\ \frac{1}{2}\left(a_1 A_1 - b_1 B_1\right)\end{array}\right] + \\ & \sin 2\phi\left[\begin{array}{c} b_2 + B_2 + \frac{1}{2}\sum_m \left(-B_m a_{m+2} + a_m B_{m+2} + A_m b_{m+2} - b_m A_{m+2}\right) + \\ \frac{1}{2}\left(a_1 B_1 + b_1 A_1\right)\end{array}\right] + \\ & \sin 3\phi\left[\begin{array}{c} b_3 + B_3 + \frac{1}{2}\sum_m \left(-B_m a_{m+3} + a_m B_{m+3} + A_m b_{m+3} - b_m A_{m+3}\right) + \\ \frac{1}{2}\left(a_1 B_2 + b_1 A_2 + a_2 B_1 + b_2 A_1\right)\end{array}\right] + \\ & \ldots\end{aligned}$$

Bibliography

[1] S. V. Bashinsky and R. L. Jaffe, Nucl. Phys. **B536**, 303.

[2] X. Ji, Phys. Rev. Lett. **78**(4), 610 (1997).

[3] P. J. Mulders and R. D. Tangerman, Nucl. Phys. **B461**, 197 (1996).

[4] V. W. Hughes and J. Kuti, Ann. Rev. Nucl. Part. Sci. **33**, 611 (1983).

[5] W. Greiner and A. Schäfer, *Quantum Chromodynamics*, Springer–Verlag, New York, 1995.

[6] J. Bjorken, Phys. Rev. **179**, 1547 (1969).

[7] J. Bjorken and E. Paschos, Phys. Rev. **185**, 1975 (1969).

[8] F. Halzen and A. D. Martin, *Quarks & Leptons: An Introductory Course in Modern Particle Physics*, John Wiley & Sons, New York, 1984.

[9] K. Ackerstaff et al., in preparation.

[10] R. L. Jaffe, hep-ph/9602236.

[11] R. L. Jaffe, hep–ph/9710465.

[12] J. Collins, Nucl. Phys. **B396**, 161 (1993).

[13] X. Ji, Phys. Lett. **B284**, 137 (1992).

[14] S. Gasiorowicz, *Elementary Particle Physics*, John Wiley & Sons, New York, 1966.

[15] X. Artru, J. Czyżewski, and H. Yabuki, Z. Phys. **C73**, 527 (1997).

[16] A. Bravar et al., Phys. Rev. Lett. **77**(13), 2626 (1996).

[17] D. L. Adams et al., Phys. Lett. **B264**, 462 (1991).

[18] D. L. Adams et al., Z. Phys. **C56**, 181 (1992).

[19] M. Anselmino and M. Boglione, hep-ph/9604397.

[20] G. L. Kane, J. Pumplin, and W. Repko, Phys. Rev. Lett. **41**(25), 1689 (1978).

[21] M. Anselmino, M. Boglione, and F. Murgia, hep-ph/9901442.

[22] D. Sivers, Phys. Rev. **D43**, 261 (1991).

[23] M. Anselmino and F. Murgia, Phys. Lett. **B442**, 470 (1998).

[24] M. Boglione and P. J. Mulders, hep-ph/9903354.

[25] A. V. Efremov et al., hep–ph/9901216.

[26] R. Jakob, D. Boer, and P. J. Mulders, hep–ph/9805410.

[27] M. Anselmino, A. Drago, and F. Murgia, hep-ph/9703303.

[28] K. A. Oganessyan, H. R. Avakian, N. Bianchi, and A. M. Kotzinian, hep–ph/9808368.

[29] G.-A. Voss and B. H. Wiik, Ann. Rev. Nucl. Part. Sci. **44**, 413 (1994).

[30] A. Sokolov and I. Ternov, Sov. Phys. Doklady **8**, 1203 (1964).

[31] J. Buon and K. Steffen, Nucl. Instr. and Meth. **A245**, 248 (1986).

[32] D. Barber et al., Nucl. Instr. and Meth. **A329**, 79 (1993).

[33] H. Kolster, PhD thesis, Ludwig–Maximilians–Universität München, 1998.

[34] B. Braun, in *7th International Workshop on Polarized Gas Targets and Polarized Beams*, Urbana-Champaign, 1997, AIP Conference Proceedings.

[35] J. Stewart, in *7th International Workshop on Polarized Gas Targets and Polarized Beams*, Urbana-Champaign, 1997, AIP Conference Proceedings.

[36] K. Ackerstaff et al., Nucl. Instr. and Meth. **A417**, 230 (1998).

[37] B. Bray, PhD thesis, California Institute of Technology, 1997.

[38] H. Avakian et al., Nucl. Instr. and Meth. **A417**, 69 (1998).

[39] W. Wander, PhD thesis, Friedrich Alexander Universität Erlangen-Nürnberg, 1996.

[40] R. Kaiser, PhD thesis, Simon Fraser University, 1997.

[41] D. de Schepper, private communication.

[42] R. D. Peccei and R. Rückl, Nucl. Phys. **B162**, 125 (1980).

[43] G. Ingelman, A. Edin, and J. Rathsman, Comp. Phys. Comm. **101**, 108 (1997).

[44] M. Arneodo et al., Z. Phys. **C34**, 277 (1987).

[45] M. R. Adams et al., Phys. Rev. **D48**, 5057 (1993).

[46] R. N. Cahn, Phys. Lett. **B78**, 269 (1978).

[47] H. Georgi and H. D. Politzer, Phys. Rev. Lett. **40**, 3 (1978).

[48] I. Akushevich, N. Shumeiko, and A. Soroko, hep-ph/9903325.

[49] M. Glück et al., Phys. Rev. **D53**, 4775 (1996).

[50] A. Dvoredsky and G. Schnell, private communication.

[51] M. Amarian et al., HERMES Internal Note 97-004, Feb. 1997.

[52] E. Cisbani et al., HERMES Internal Note 97-003, Mar. 1997.

[53] I. Adachi et al., Nucl. Instr. and Meth. **A355**, 390 (1995).

[54] G. Poelz and R. Riethmüller, Nucl. Instr. and Meth. **195**, 491 (1982).

[55] T. M. Tillotson and L. W. Hrubesh, J. Non-Cryst. Solids **145**, 44 (1992).

[56] D. E. Fields et al., Nucl. Instr. and Meth. **A349**, 431 (1994).

[57] R. De Leo et al., Nucl. Instr. and Meth. **A401**, 187 (1997).

[58] C. Caso et al., Euro. Phys. J. **C3**, 1 (1998).

[59] S. Henning and L. Svensson, Physica Scripta **23**, 697–702 (1981).

[60] D. Gray, editor, *AIP Handbook*, McGraw-Hill, New York, 2nd edition, 1963.

[61] M. Kerker, *The Scattering of Light*, Academic Press, New York, 1969.

[62] A. Beck, W. Körner, and J. Fricke, J. Phys. D **27**, 13–18 (1994).

[63] J. Kanesaka et al., HERMES Internal Note 98-061, Nov. 1998.

[64] E. Cisbani et al., in *Proceedings of the New Detectors Workshop*, Erice, Nov. 1997.

[65] R. De Leo et al., in preparation.

[66] G. Poelz, Nucl. Instr. and Meth. **A248**, 118–129 (1986).

[67] P. Wang et al., J. Non-Cryst. Solids **145**, 141 (1992).

[68] A. Emmerling et al., J. Non-Cryst. Solids **185**, 240 (1995).

[69] D. W. Hua et al., J. Non-Cryst. Solids **186**, 142 (1995).

[70] M. Amarian and A. Avetisyan, HERMES Internal Note 98-022, May 1998.

[71] D. Boer and P. J. Mulders, Phys. Rev. **D57**, 5780 (1998).

[72] P. J. Mulders, hep-ph/9903014.